

AD-A104 632

TECHNICAL
LIBRARY

AD A-104632

CONTRACT REPORT ARBRL-CR-00463

CALCULATIONS OF INTERNAL BALLISTIC FLOW
WITH A PROJECTILE TO WALL GAP

Prepared by

JAYCOR
11011 Torreyana Road
P. O. Box 85154
San Diego, CA 92138

August 1981



US ARMY ARMAMENT RESEARCH AND DEVELOPMENT COMMAND
BALLISTIC RESEARCH LABORATORY
ABERDEEN PROVING GROUND, MARYLAND

Approved for public release; distribution unlimited.

Destroy this report when it is no longer needed.
Do not return it to the originator.

Secondary distribution of this report by originating
or sponsoring activity is prohibited.

Additional copies of this report may be obtained
from the National Technical Information Service,
U.S. Department of Commerce, Springfield, Virginia
22161.

The findings in this report are not to be construed as
an official Department of the Army position, unless
so designated by other authorized documents.

*The use of trade names or manufacturers' names in this report
does not constitute endorsement of any commercial product.*

UNCLASSIFIED

SECURITY CLASSIFICATION OF THIS PAGE (When Data Entered)

| REPORT DOCUMENTATION PAGE | | READ INSTRUCTIONS BEFORE COMPLETING FORM |
|--|-----------------------|---|
| 1. REPORT NUMBER CONTRACT REPORT ARBRL-CR-00463 | 2. GOVT ACCESSION NO. | 3. RECIPIENT'S CATALOG NUMBER |
| 4. TITLE (and Subtitle) Calculations of Internal Ballistic Flow with a Projectile to Wall Gap | | 5. TYPE OF REPORT & PERIOD COVERED |
| | | 6. PERFORMING ORG. REPORT NUMBER |
| 7. AUTHOR(s) J.H. Stuhmiller R.E. Ferguson | | 8. CONTRACT OR GRANT NUMBER(s) DAAK11-80-C-0008 |
| 9. PERFORMING ORGANIZATION NAME AND ADDRESS JAYCOR 11011 Torreyana Road P.O. Box 85154 San Diego, CA 92138 | | 10. PROGRAM ELEMENT, PROJECT, TASK AREA & WORK UNIT NUMBERS |
| 11. CONTROLLING OFFICE NAME AND ADDRESS US Army Armament Research and Development Command US Army Ballistic Research Laboratory ATTN: DRDAR-BL Aberdeen Proving Ground, Maryland 21005 | | 12. REPORT DATE AUGUST 1981 |
| 14. MONITORING AGENCY NAME & ADDRESS (if different from Controlling Office) | | 13. NUMBER OF PAGES 116 |
| | | 15. SECURITY CLASS. (of this report) UNCLASSIFIED |
| | | 15a. DECLASSIFICATION/DOWNGRADING SCHEDULE |
| 16. DISTRIBUTION STATEMENT (of this Report) Approved for public release, distribution unlimited. | | |
| 17. DISTRIBUTION STATEMENT (of the abstract entered in Block 20, if different from Report) | | |
| 18. SUPPLEMENTARY NOTES | | |
| 19. KEY WORDS (Continue on reverse side if necessary and identify by block number) Interior Ballistics Corner Flow Numerical Analysis | | |
| 20. ABSTRACT (Continue on reverse side if necessary and identify by block number) (d11) The flow near the conjunction of the base of a moving projectile and the gun tube wall, with and without a 1% gap, has been simulated using the SAGITA code. Results are presented for both a 20 and a 40 mm gun and the predicted flow configurations were checked by several mesh refinement studies. | | |

CONTENTS

| | <u>Page</u> |
|--|-------------|
| INTRODUCTION | 9 |
| DISCUSSION OF RESULTS | 12 |
| APPENDIX A. MATHEMATICAL MODELS AND NUMERICAL ALGORITHMS | 49 |
| APPENDIX B. DISCUSSION OF ADDITIONAL CALCULATIONS | 63 |
| APPENDIX C. CONSIDERATION OF THE OUTFLOW BOUNDARY CONDITIONS | 107 |
| DISTRIBUTION LIST..... | 113 |

ILLUSTRATIONS

| <u>No.</u> | <u>Title</u> | <u>Page</u> |
|------------|---|-------------|
| 1. | Mesh configuration for 20 × 20 calculation in a 20 mm diameter barrel | 18 |
| 2. | Flow in the corner between the shell base and the wall at 0.06 ms .. | 18 |
| 3. | Flow in the corner is described in Figure 2 | 19 |
| 4. | Flow in the corner as described in Figure 2 | 19 |
| 5. | Flow in the corner as described in Figure 2 | 20 |
| 6. | Final configuration of corner flow ($t = 1.85$ ms) | 20 |
| 7. | Pressure field at 0.84 ms | 21 |
| 8. | Pressure distribution at late times ($t = 2.29$ ms) | 21 |
| 9. | Time history of pressure at centerline of shell | 22 |
| 10. | Time history of the pressure at corner of shell | 22 |
| 11. | Temperature contours in the corner region at early times; $t = 0.08$ ms | 23 |
| 12. | Temperature variations due to wall heating are starting to develop axially | 23 |
| 13. | Growing thermal layer in corner at late time ($t = 2.29$ ms) | 24 |
| 14. | Time history of temperature at the corner of the shell | 24 |
| 15. | Mesh configuration for the standard resolution calculation of flow with a 1% gap | 25 |
| 16. | Velocity vectors in the gap region on the last cycle before the code diverged when the outlet conditions were 90% sonic plus shell speed | 25 |
| 17. | Pressure contours for the same case described in Figure 16 | 26 |
| 18. | Temperature contours for the same case described in Figure 16 | 26 |
| 19. | Velocity vectors in the gap region just before the code diverged in the case when the outlet velocity was 90% of sonic speed in the absolute frame of reference | 27 |
| 20. | Flow in gap when outlet velocity is 50% sonic | 27 |
| 21. | Flow in gap under conditions described in Figure 21 | 28 |
| 22. | Flow in gap under conditions described in Figure 20 | 28 |
| 23. | Flow in gap under conditions described in Figure 20 | 29 |
| 24. | Pressure contours at same time shown in Figure 23 | 29 |
| 25. | Pressure contours in gap under conditions described in Figure 20 at a time just after the maximum internal velocity is achieved | 30 |
| 26. | Flow in the gap at late times under conditions described in Figure 20 | 30 |
| 27. | Maximum velocity in the gap, not counting the applied outlet value, for the cases discussed in the previous figures | 31 |
| 28. | Flow in the vicinity of the corner for 20 mm diameter barrel with 1% gap | 32 |
| 29. | Flow in vicinity of corner for same conditions described in Figure 28 | 32 |
| 30. | Flow in the vicinity of the corner for the same conditions described in Figure 28 | 33 |
| 31. | Flow in the vicinity of the corner for the same conditions described in Figure 28 | 33 |
| 32. | Pressure contours in the vicinity of the corner for the case described in Figure 28 | 34 |

| | | |
|------|--|----|
| 33. | Time history of pressure at the corner of shell and centerline for 20 mm diameter barrel with 1% gap | 34 |
| 34. | Time history of temperature at the corner of the shell and at the centerline for a 20 mm diameter barrel with a 1% gap | 35 |
| 35. | Temperature contours at late time for 20 mm barrel with a 1% gap ... | 35 |
| 36. | High resolution calculation of flow in the gap for a 20 mm barrel with a 1% gap | 36 |
| 37. | Time history of pressure at corner of shell for 20 mm barrel with 1% gap | 36 |
| 38. | Time history of pressure at base on centerline for 20 mm barrel with 1% gap | 37 |
| 39. | Time history of temperature at the corner of shell for a 20 mm barrel with a 1% gap | 37 |
| 40. | Time history of temperature at base centerline for 20 mm barrel with a 1% gap | 38 |
| 41. | Flow pattern in the vicinity of the corner for the case of a 20 mm barrel with a 1% gap | 38 |
| 42. | Flow pattern in the vicinity of the corner for the case described in Figure 1 | 39 |
| 43. | Flow pattern in the vicinity of the corner for the case described in Figure 41 | 39 |
| 44. | Flow pattern in the vicinity of the corner for the case described in Figure 41 | 40 |
| 45. | Whole field visualization of flow in 20 mm no gap case | 40 |
| 46. | See caption for Figure 45 | 41 |
| 47. | See caption for Figure 45 | 41 |
| 48. | See caption for Figure 45 | 42 |
| 49. | See caption for Figure 45 | 42 |
| 50. | Whole field visualization for 20 mm, 1% gap case with standard resolution | 43 |
| 51. | See caption for Figure 50 | 43 |
| 52. | See caption for Figure 50 | 44 |
| 53. | See caption for Figure 50 | 44 |
| 54. | See caption for Figure 50 | 45 |
| 55. | Whole field visualization for the 20 mm, 10% gap case with high resolution | 45 |
| 56. | See caption for Figure 55 | 46 |
| 57. | See caption for Figure 55 | 46 |
| 58. | See caption for Figure 55 | 47 |
| B-1. | Whole field visualization of 20 mm, 1% gap when no net flow boundary conditions are used at the exit of the gap | 70 |
| B-2. | See caption for Figure B-1 | 70 |
| B-3. | See caption for Figure B-1 | 71 |
| B-4. | See caption for Figure B-1 | 71 |
| B-5. | See caption for Figure B-1 | 72 |
| B-6. | Time history of pressure at the shell corner for 20 mm diameter barrel with a 1% gap and no net bypass flow | 72 |
| B-7. | Time history of temperature at the shell corner for a 20 mm diameter barrel with a 1% gap and no net bypass flow | 73 |
| B-8. | Temperature contours in the whole field visualization for a 20 mm diameter barrel with 1% gap and no net bypass flow | 73 |

| | | |
|-------|---|----|
| B-9. | Whole field visualization of flow pattern in 40 mm barrel with no gap | 74 |
| B-10. | See caption for Figure B-9 | 74 |
| B-11. | Time history of pressure at shell corner for 40 mm diameter barrel with no gap | 75 |
| B-12. | Time history of temperature at the shell corner for 40 mm diameter barrel with no gap | 75 |
| B-13. | Whole field visualization of temperature contours for 40 mm, no gap case | 76 |
| B-14. | Whole field visualization for 40 mm diameter barrel with no gap when the gas kinematic viscosity is assumed to be 10^{-4} cm ² /sec ... | 76 |
| B-15. | See caption for Figure B-14 | 77 |
| B-16. | Time history of the pressure at the corner of the shell for the 40 mm barrel, no gap case with viscosity equal to 10^{-4} cm ² /sec | 77 |
| B-17. | Time history of temperature at the shell corner for the 40 mm, no gap case with viscosity raised to 10^{-4} cm ² /sec | 78 |
| B-18. | Whole field visualization of temperature contours at late time for 40 mm, no gap case with viscosity raised to 10^{-14} cm ² /sec | 78 |
| B-19. | Whole field visualization of flow pattern for 40 mm diameter barrel with a 1% gap when no net outflow is permitted | 79 |
| B-20. | See caption for Figure B-19 | 79 |
| B-21. | See caption for Figure B-19 | 80 |
| B-22. | See caption for Figure B-19 | 80 |
| B-23. | Time history of pressure at the corner of the shell for a 40 mm diameter barrel with a 1% gap | 81 |
| B-24. | See caption for Figure B-19 | 81 |
| B-25. | Time history of the gas temperature at the corner of the shell for a 40 mm diameter barrel with a 1% gap | 82 |
| B-26. | See caption for Figure B-19 | 82 |
| B-27. | Whole field visualization of the flow pattern for a 40 mm diameter barrel with a 1% gap using the turbulence model of Pope and Whitelaw | 83 |
| B-28. | See caption for Figure B-27 | 83 |
| B-29. | See caption for Figure B-27 | 84 |
| B-30. | See caption for Figure B-27 | 84 |
| B-31. | Time history of pressure at the corner of the shell for a 40 mm diameter barrel with a 1% gap using the Pope and Whitelaw turbulence model | 85 |
| B-32. | See caption for Figure B-27 | 85 |
| B-33. | Time history of gas temperature at the corner of the shell for a 40 mm diameter barrel with a 1% gap using the Pope and Whitelaw turbulence model | 86 |
| B-34. | See caption for Figure B-27 | 86 |
| B-35. | Whole field visualization of flow pattern in 40 mm barrel with a 1% gap when the viscosity has been raised to a uniform value of 10^{-3} cm ² /sec | 87 |
| B-36. | See caption for Figure B-35 | 87 |
| B-37. | See caption for Figure B-35 | 88 |
| B-38. | See caption for Figure B-35 | 88 |
| B-39. | Time history of pressure at corner of shell for 40 mm diameter barrel with a 1% gap when the viscosity has been raised to 10^{-3} cm ² /sec | 89 |

| | | |
|-------|---|-----|
| B-40. | See caption for Figure B-35 | 89 |
| B-41. | Time history of the gas temperature at the corner of the shell for a 40 mm diameter barrel with a 1% gap when the viscosity is raised to 10^{-3} cm ² /sec | 90 |
| B-42. | See caption for Figure B-35 | 90 |
| B-43. | Expanded computational grid for calculation at standard resolution (20×20 in chamber) | 91 |
| B-44. | Whole field visualization of flow pattern for a 40 mm diameter barrel with a 1% gap and a viscosity of 10^{-4} cm ² /sec | 91 |
| B-45. | See caption for Figure B-44 | 92 |
| B-46. | See caption for Figure B-44 | 92 |
| B-47. | See caption for Figure B-44 | 93 |
| B-48. | See caption for Figure B-44 | 93 |
| B-49. | See caption for Figure B-44 | 94 |
| B-50. | Time history of pressure at cell corner for calculation at standard resolution | 94 |
| B-51. | See caption for Figure B-44 | 95 |
| B-52. | Time history of temperature at corner of shell for calculation at standard resolution | 95 |
| B-53. | See caption for Figure B-44 | 96 |
| B-54. | Expanded computational grid for making the twice normal resolution runs (40×40) | 96 |
| B-55. | Whole field visualization of flow pattern for (40×40) resolution calculation of 40 mm diameter barrel with 1% gap | 97 |
| B-56. | See caption for Figure B-55 | 97 |
| B-57. | See caption for Figure B-55 | 98 |
| B-58. | See caption for Figure B-55 | 98 |
| B-59. | See caption for Figure B-55 | 99 |
| B-60. | See caption for Figure B-55 | 99 |
| B-61. | Time history of pressure at the corner of the shell showing the same behavior as in the lower resolution runs | 100 |
| B-62. | Time history of temperature at the corner of the shell showing the same behavior as in the low resolution calculations | 100 |
| B-63. | Computation grid for highest radial resolution calculation (20×80) | 101 |
| B-64. | Highest resolution calculation of 40 mm diameter barrel with 1% gap | 101 |
| B-65. | See caption for Figure B-64 | 102 |
| B-66. | See caption for Figure B-64 | 102 |
| B-67. | See caption for Figure B-64 | 103 |
| B-68. | See caption for Figure B-64 | 103 |
| B-69. | Time history of pressure at the corner of the shell for 40 mm diameter barrel, 1% gap with high (20×80) resolution | 104 |
| B-70. | Time history of gas temperature at the corner of the shell for case described in Figure B-69 | 104 |
| B-71. | See caption for Figure B-64 | 105 |

INTRODUCTION

Background

Previous calculations by another contractor using a nonstaggered numerical scheme for ballistic flow with no shell to barrel gap led to peculiar results at the contact corner. In order to proceed with the systematic development of a multi-dimensional, multi-phase ballistics code it is necessary to resolve this matter and determine the role played by the shell to barrel gap. Because of JAYCOR's experience in computational fluid dynamics, this project was initiated to address the corner flow.

Scope of the Work

In order to produce results on corner flow behavior with a minimum of distraction by other ballistics issues it was decided to limit the cases studied and parameters varied. The initial scope called for runs for a 40 mm diameter barrel with and without a 1% gap and for a 20 mm diameter barrel with no gap. A two-variable turbulence model was to be used for the 40 mm case. A moving coordinate system was adopted to avoid the problem of an expanding grid, with pressure boundary conditions on the open end to be taken from the earlier, nonstaggered grid calculations. Accuracy of the calculations were to be checked with runs on a 20×20 , 40×40 , and 80×80 grid.

After the initial results were reported it was decided to add additional cases: 20 mm with a 1% gap at 20×20 and 40×40 resolution. At the same time, it was decided to explore other outlet flow conditions at the top of the gap to force a net bypass flow around the shell.

The results of these calculations were to be analyzed from the point of view of phenomena occurring in the corner region.

Summary of results

The results are discussed in detail in the next section but they can be summarized as follows.

(1) All of the cases were successfully run by the code except when the outflow boundary conditions tried to drive the interior flow supersonic in the

absolute frame of reference or when the turbulence model gave a physical results.

(2) For the outlet boundary conditions considered, the flow near the corner is considerably different with and without a gap. The net flow around the projectile causes a flow splitting at the corner with part of the flow feeding the developing boundary layer and part venting through the gap. The flow in the corner region tends to be more complex, with a recirculation zone, counter current streams (in the projectile's frame of reference), and a boundary layer all occurring within a very small space.

(3) The gas temperature in the neighborhood of the projectile corner is nearly equal in both cases, but the wall temperature at that location can be as much as 150° higher with a gap. This difference is due to the wall heating in the gap region that feeds the corner flow and to the reduction of cooling flow to the boundary layer caused by flow splitting.

(4) The corner flow is strongly affected by the prescribed boundary conditions. The corner flow develops in about the same length of time as the overall ballistic motion so the start up transients are an inseparable part of the problem. The initial acceleration of the shell creates a low pressure region at the base which is fed both by the chamber and the gap - this effect is a major difference between the gap and no gap cases. The downflow from the gap leads to a corner eddy that persists for most of the problem time and strongly effects the pressure history in that region. Flow reversals in the chamber due to rarefaction pulses also influence the developing flow and may be caused by inconsistencies between the prescribed outlet pressure and the present calculation. The sudden application of the gap outflow conditions leads to a rarefaction pulse in the gap that influences the corner flow and the assumption of a uniform outflow seems to contradict the counter current flow (in the shell's frame of reference) that tries to develop. These effects may not affect the qualitative nature of the flow but they surely affect the quantitative detail.

(5) Turbulence does not seem to have sufficient time to develop from laminar flow and the use of conventional models led to spurious results. Estimates were made that showed there were not enough e-folding times to reach transition based on the growth of laminar disturbances. Use of a two-variable turbulence model, based on fully developed turbulence arguments, gave unphysically large production in the corner region and caused the calculation to

abort. On the other hand, calculations made with molecular viscosity alone were stable.

DISCUSSION OF RESULTS

Standard resolution, 20 mm, no gap

The starting point for the work done under this project is a 20×20 cell calculation of the flow in a 20 mm diameter barrel with a shell that allows no gap. Figure 1 shows the arrangement of mesh points; there is a concentration of cells near the wall to adequately resolve the developing boundary layer and flow near the corner. Note that in plotting the mesh the radial distance has been expanded by a factor of four so that more detail can be seen; even expanded, the finest cells can still be barely resolved.

At the initial instant the gas and shell are at rest and the gas pressure is uniform. The high pressure begins to accelerate the shell which increases the volume of the firing chamber and lowers the pressure. In all calculations discussed in this report, the boundary pressure along the bottom was prescribed and the shell motion calculated from Newton's Law. The start up process, as well as possible inconsistencies between the previously calculated boundary pressure and the present calculation, causes a small rarefaction wave to be generated and bounce off the computational boundaries a few times before diffusing. The time required for the rarefaction generated at the base of the shell to propagate to the open boundary and back is about 0.1 ms. This period corresponds to the appearance of flow reversal in the corner at 0.08 ms and 0.2 ms. Figures 2-5 show the flow oscillation at times 0.06, 0.08, 0.12, and 0.20 ms. The vectors are scaled differently in each Figure and the radial velocity component is magnified in proportion to the expansion of the radial coordinate itself. No more flow direction changes occur after this time and, except for scale effects, the corner flow is typified by that shown in Figure 6: a small, steady radial flow toward the wall that feeds a narrow, growing boundary layer.

During the transient the pressure is dominated by the overall chamber pressure, set by the pressure boundary conditions, and the slight gradient away from the shell that causes the gas to lag the shell. See Figure 7 for a typical pressure contour map at 0.84 ms. The early gas dynamics waves are also planar and do not readily show up on these plots. At late times the pressure variation is still essentially axial, c.f. Figure 8. With the exception of the momentary perturbation due to the bouncing gas dynamics waves, the pressure

histories at the centerline of the shell (Figure 9) and at the corner (Figure 10) show the same steady decrease due to expansion.

The temperature, on the other hand, evolves considerably during the motion of the shell. At early times it is nearly uniform and drops steadily as the pressure drops. See Figure 11. As the wall boundary wall heating sets in and gradients develop along the wall. See Figure 12. The temperatures are cooler near the bullet because this is where the inflow of gas from the center of the chamber feeds the boundary layer. At 2.29 ms, a 30°C temperature differential has developed between a point near the corner and the centerline. See Figure 13. The difference at the corner is much less. The temperature nearest to the corner shows the same general decrease evidenced in the pressure histories. See Figure 14. The early oscillations are due to essentially adiabatic heating and cooling due to the gas dynamics waves.

Standard resolution, 20 mm, 1% gap case

Next, the calculational domain was extended along the axial direction to allow the resolution of a 1% gap. Figure 15 shows the entire mesh; the axial and radial scales have been further distorted so that detail can be seen. There are three cells resolving the gap width and twenty along its length. The mesh below the shell is identical to the one used in the no gap case.

The gap problem requires an additional boundary condition: the outflow condition at the end of the gap at the front of the shell. This condition can only be determined by making a complete calculation that extends far in front of the shell where the ambient conditions are known. In order not to detract from the immediate objective of this project, that of studying the corner flow, it was decided to use an ad hoc assumption. Several possibilities were discussed and tried including setting the outlet velocity to: 10% more than the shell speed; the shell speed; 50% of the shell speed; shell speed + 90% sonic; 90% sonic; and others. We now discuss one series of runs.

Since the pressure drop from the back to the front of the shell is quite large, it was suggested that the flow might be choked, that is, that a standing shock would form at the outlet. Since, however, the gap is quite narrow, 10^{-4} m, and viscosity is not negligible over the time of the problem, $v\Delta t/\Delta r^2 \sim 1$, then the outflow may be sonic only over part of the gap. This line of argument led to the proposition that the outflow be 90%, say, of sonic. It was

further proposed that the outflow be relative to the shell. This means that when the shell reached a speed of about 100 m/sec, the gas flow would be sonic relative to the absolute frame of reference. Precisely at this time the code diverged. Graphics from the last few cycles show clearly what had taken place.

Figure 16 shows the velocity vectors in the gap region just before the code diverged. The outlet velocity has just gone slightly supersonic in the absolute frame of reference and the third row of velocities marks the upstream edge of a shock that has formed. Figure 17 shows the pressure contours at the same instant and the bunching together of the values around an internal maximum marks the approximate shock location. Since the method is not designed for supersonic flow, once it is created a nonphysical runaway thermodynamic process occurs. Figure 18 shows the temperature just ahead of the shock in excess of 5000 C and this catastrophic production of internal energy is the process that eventually causes the code to fail. Clearly the gas velocity cannot exceed sonic in the absolute frame of reference.

Next we tried an outlet condition that was 90% of sonic in the absolute frame of reference. It, too, diverged shortly after the start of the problem for the same reason: an internal shock formed, despite the fact that the outlet remained subsonic. The growth of the wall boundary layer is sufficient to retard a significant part of the flow and force the central part of the gap flow to become supersonic. See Figure 19. An additional process, just starting to appear at this time, is the flow separation at the inlet to the gap which also constricts the flow and forces an internal shock to form.

Finally, the choice of an outlet velocity of 50% of sonic in the absolute frame of reference worked. A maximum internal velocity of about 90% sonic occurs 0.3 ms into the problem which then reduces to nearly the outlet speed at late times. The outlet conditions lead to a upstream propagating rarefaction that accelerates the flow toward the outlet. This can be seen in Figures 20 and 21. Figures 22 and 23 show that the developing wall boundary layer forces the flow toward the shell and accelerates it to a value nearly twice the exit speed. At this time the chamber pressure is still greater than the exit as can be seen in Figure 24. Around 0.3 ms the chamber pressure drops below that of the exit causing the flow to decelerate. See Figure 25. After another 0.3 ms the gap flow settles down to a balance between a nearly fully developed boundary layer and a weak pressure gradient. As Figure 26 shows flow reversal occurs right at the exit indicating that a uniform exit velocity is

probably not correct. The flow, however, seems to recover quickly so that at the gap it is in the proper direction.

The maximum velocity histories for the above cases are summarized in Figure 27. Qualitative agreement was gotten when the mesh was refined by a factor of two with the maximum velocity nearly going sonic.

The velocity patterns in the vicinity of the corner are shown in Figures 28-31. The low pressure generated by the initial acceleration of the shell at first draws flow in from the gap. As the density of the gas in the gap decreases, the pressure falls and backflow finally ceases around 0.1 ms. Further flow from the exit lowers the gap pressure below that in the chamber, drawing gas into the gap. Finally, the wall boundary layer develops and flow splitting at the corner occurs. For the outlet conditions used in this case the radial flow along the shell has been greatly enhanced.

The pressure contours are similar to the no gap case where the pressure was quite uniform within the chamber near the corner. See Figure 32. However, during the development of the radial flow into the boundary layer and the gap, the corner and centerline pressures differ by as much as 300 atmospheres. See figure 33. There was no discernible difference in the no gap case. The centerline curves from the gap and no gap cases overlay one another except for the early oscillations. This agreement seems to indicate that the chamber pressure is governed by the conditions at the open boundary and that the rarefaction wave that bounced around in the first calculation has been filled in with the back flow from the gap.

The temperature field evolution is also similar to the no gap case: at early time, uniform temperatures primarily governed by expansion cooling; at late times, viscous heating of the wall boundary layer. The temperature, however, varies from the centerline value as the flow evolves. See Figure 34. Since the wall flow is carried in from the gas ahead of the shell, the wall temperatures will depend upon the outlet conditions, which are probably not totally correct in these calculations. The corner of the shell and the wall could differ by more than 100° C, a variation not seen in the no gap case. See Figure 35.

High Resolution, 20 mm, 1% gap case

The previous calculation was repeated with every cell halved in size in both dimensions to produce a 40×40 grid in the chamber and a 40×7 grid within the gap.

The expanded flow in the gap displayed the same characteristics as for the low resolution case. The wall boundary layer reverses the flow one cell below the exit and the layer occupies 2 cells in agreement with the earlier results. The structure of the upward flow is clearer, with the maximum occurring away from the shell as it should since a boundary layer must form there too. See Figure 36.

The pressure and temperature time histories at the centerline and at the corner compare favorably in Figures 37-40. There are more variations in the higher resolution run near the corner. Part of the reason for this is that the value is closer to the corner where the flow varies more rapidly and where it may remain unsteady.

The flow field in the corner region is shown in Figures 41-44. The backflow due to the initial acceleration is now more accurately resolved and separated flow from the corner is clearly seen. The recirculation eddy persists after the backflow ceases. Later, the wall boundary layer develops and the flow along the base splits at the corner as occurred in the lower resolution run.

Comparison between the runs at two different resolutions leads us to conclude that the 20×20 calculation captures the quantitative essence of the flow. The exact details of the motion, especially at the recirculation zones, are seen much more clearly in the higher resolution case. It would probably be appropriate to use these results as boundary conditions to a very fine mesh calculation if more detail were required.

Visualization of total flow field

The aspect ratio of the geometries in this problem are so large that it is impossible to view the flow over any reasonable extent and maintain the proper geometric relationships. We have used a distorted presentation of the data in the corner region to illustrate the flow pattern there with some success. In this section we present the entire calculational domain, with even

greater geometric distortion, in order to give the reader a feeling for the overall motion of the fluid. The technique employed is to make every velocity vector fill the cell it occupies so that through a head-to-tail connection the viewer's eye is attracted to the streamline pattern. The penalty for this approach is that very small flows are over emphasized, however, the comprehension gained by the overview seems to justify the attempt.

The whole field visualization for the no gap case is shown in Figures 45-49. The flow reversals, seen earlier in the corner pictures, occurs over the whole field and may be due to an inconsistency between the shell motion and the prescribed boundary pressures. This method of presentation has suppressed the boundary layer by making all velocities equal; actually most of the flow is in a thin wall layer.

Figures 50-54 show the whole field flow visualization for the 1% gap case with standard resolution. The initial backflow and separation region can be seen as well as the local rarefaction that develops in the gap. The recirculation eddy builds up and is shed from the shell as the flow back into the gap is established. Finally, a splitting of the flow along the shell base is established.

Figures 55-58 show the whole field flow visualization for the high resolution case. The evolution follows that of the lower resolution calculation except that more detail on the region just behind the shell is obtained. The visualizations and the earlier quantitative comparisons of pressures and temperatures leads us to conclude that the 20×20 is satisfactorily detailed.

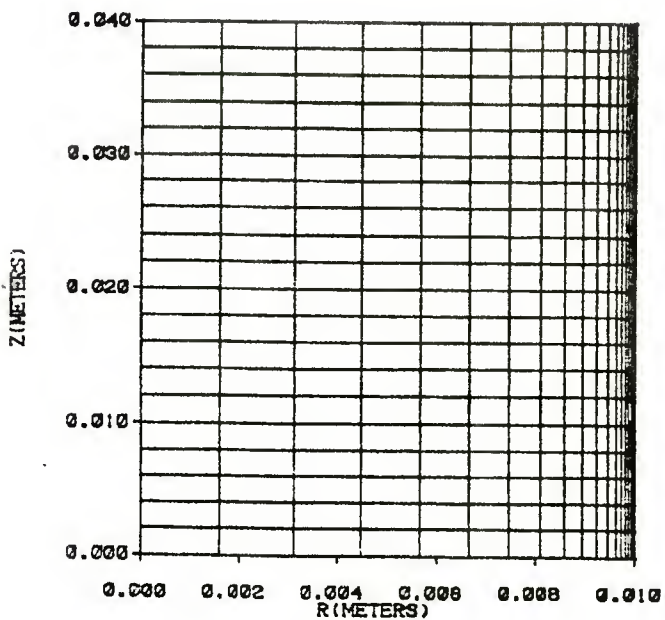


Figure 1. Mesh configuration for 20×20 calculation in a 20 mm diameter barrel. The radial direction has been expanded by a factor of four to allow more detail to be seen.

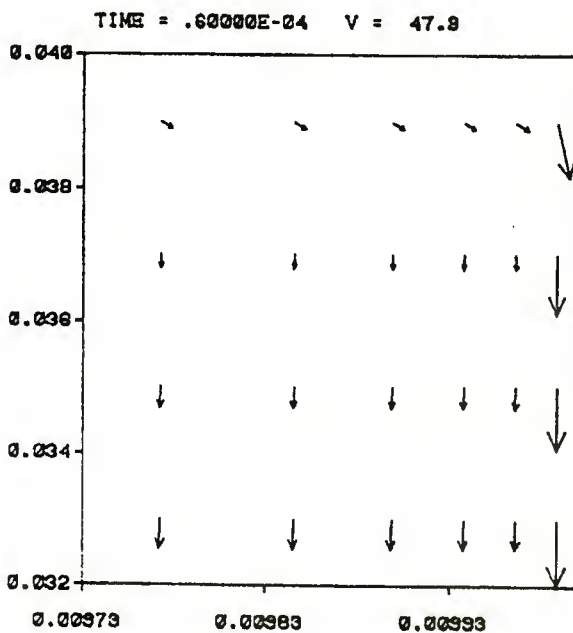


Figure 2. Flow in the corner between the shell base and the wall at 0.06 ms. The radial coordinate and radial velocity component has been greatly enlarged for clarity. At this moment the flow relative to the shell is away from the shell.

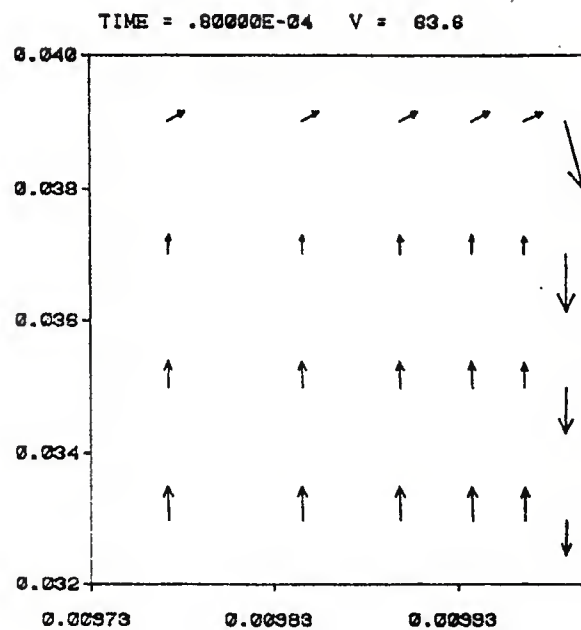


Figure 3. Flow in the corner is described in Figure 2. Time is 0.08 ms and a flow toward the shell in the accelerating frame of reference has developed due to gas dynamics effects originating from the start-up.

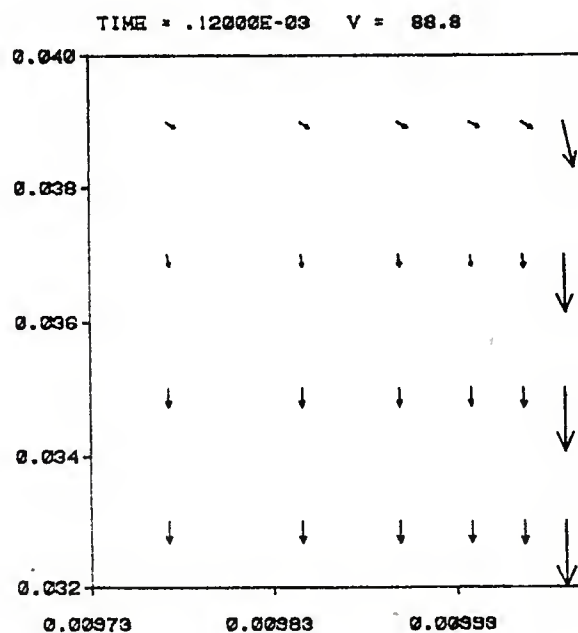


Figure 4. Flow in the corner as described in Figure 2. Time is 0.12 ms and flow is once again away from the shell.

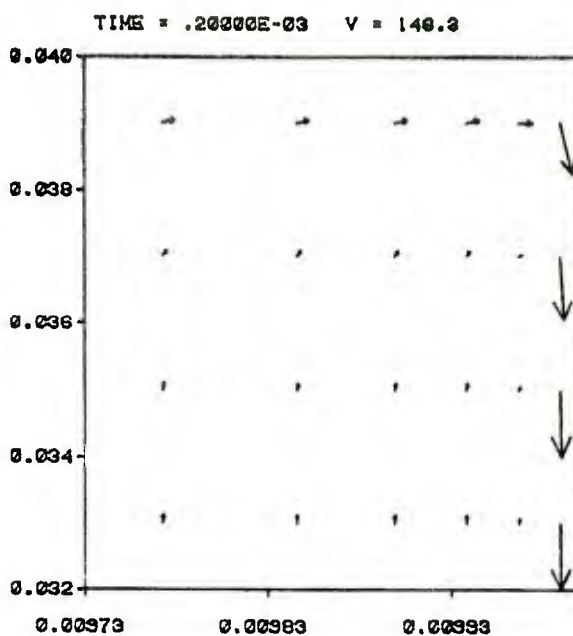


Figure 5. Flow in the corner as described in Figure 2. Time is 0.20 ms as a final, weak flow reversal has occurred due to the second bounce of the rarefaction wave.

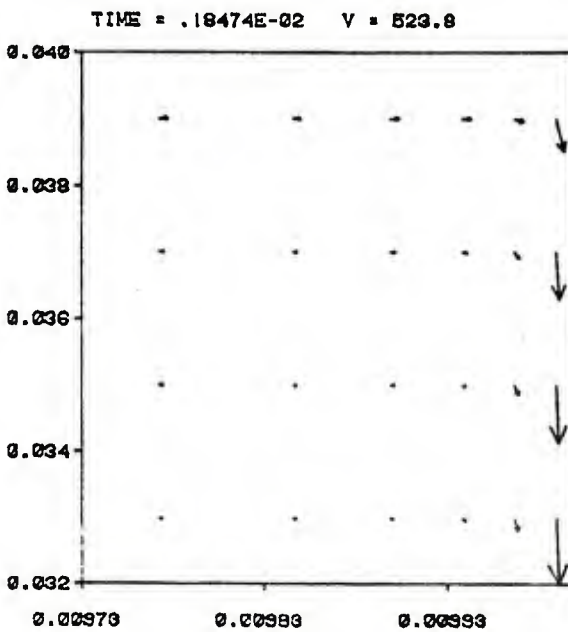
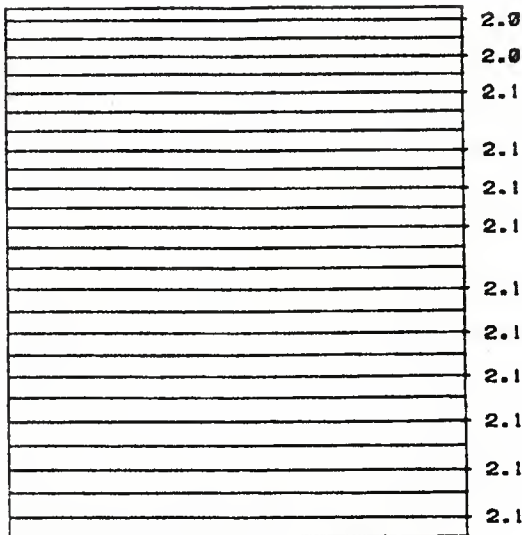
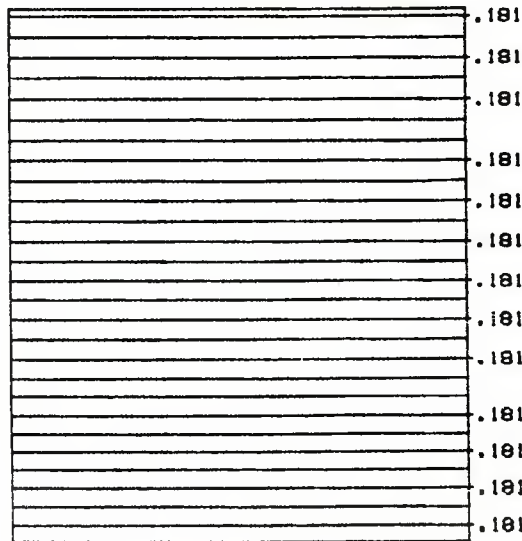


Figure 6. Final configuration of corner flow ($t = 1.85$ ms). Flow moves slowly from the centerline toward the wall where it feeds a strong, narrow boundary layer. Recall that there is about an order of magnitude expansion in the radial coordinate and velocity.



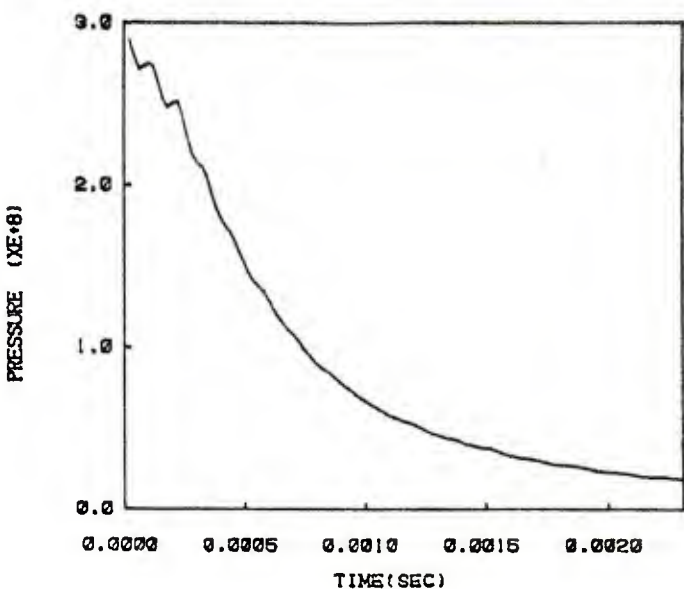
PRESSURE CONTOURS AT TIME = .84000E-03

Figure 7. Pressure field at 0.84 ms. A simple axial gradient between the shell and the open boundary forms. The rarefaction waves are not apparent on any of the pressure plots because they are small and without radial variation.



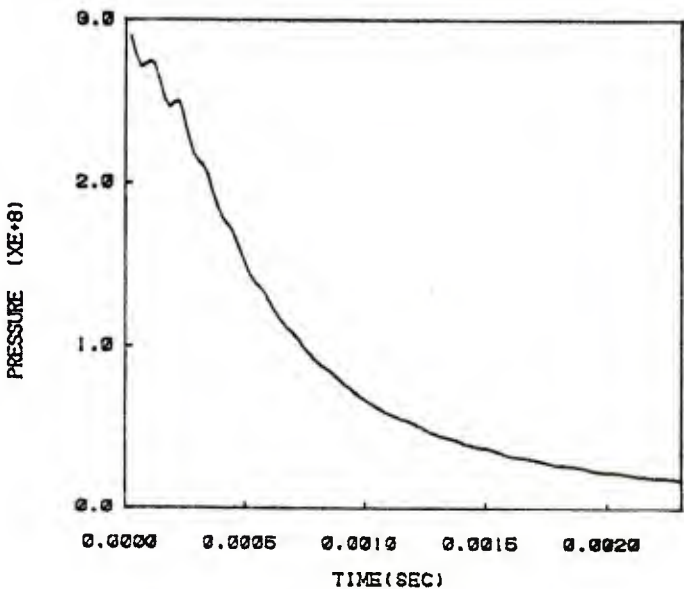
PRESSURE CONTOURS AT TIME = .22890E-02

Figure 8. Pressure distribution at late times ($t = 2.29$ ms). Except for the overall magnitude, the pressure contours remain the same throughout the bullet motion.



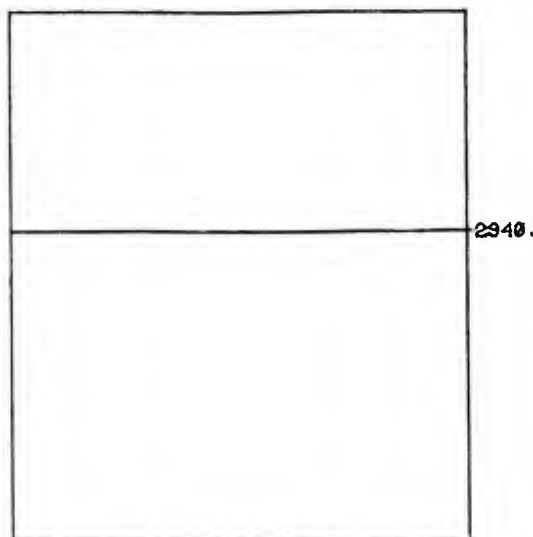
TIME HISTORY AT CENTERLINE AT BASE OF PROJECTILE

Figure 9. Time history of pressure at centerline of shell. The overshooting due to the bouncing gas dynamics waves can be seen at 1 ms intervals. Up to 6 or 7 bounces can be resolved, but only the first two are strong enough to change the direction of the pressure variation and consequently the flow.



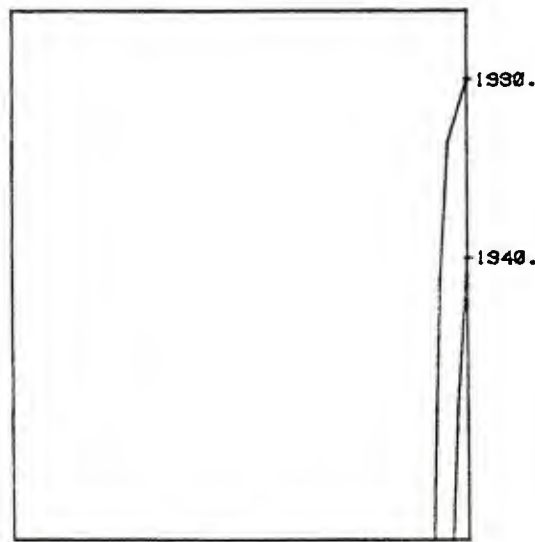
TIME HISTORY AT CORNER OF PROJECTILE

Figure 10. Time history of the pressure at corner of shell. The behavior is identical to that on the centerline because the flow direction is essentially axial.



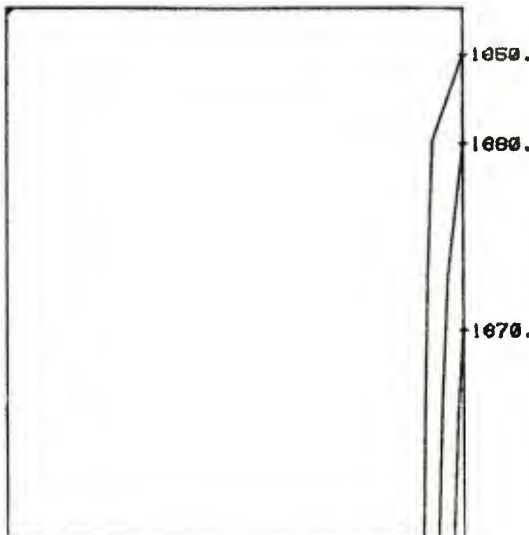
TEMPERATURE CONTOURS AT TIME = .80000E-04

Figure 11. Temperature contours in the corner region at early times; $t = 0.08$ ms. Contour lines are every 10°C so the temperature is everywhere within 10°C of 2940°C .



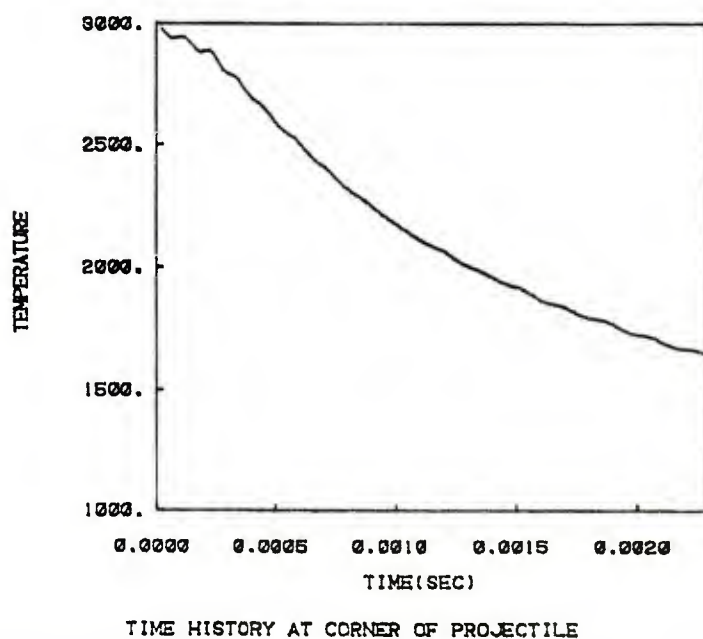
TEMPERATURE CONTOURS AT TIME = .147495-02

Figure 12. Temperature variations due to wall heating are starting to develop axially. The temperatures are cooler near the bullet, and more like the bulk gas temperature, because this is where the boundary layer is fed by the general radial flow.



TEMPERATURE CONTOURS AT TIME = .228995-02

Figure 13. Growing thermal layer in corner at late time ($t = 2.29$ ms). The corner itself is still near the bulk gas temperature because of the gas inflow along the shell.



TIME HISTORY AT CORNER OF PROJECTILE

Figure 14. Time history of temperature at the corner of the shell. The temperature essentially traces the gas pressure including the early oscillations due to compressive heating and expansion cooling caused by the bouncing gas dynamics waves.

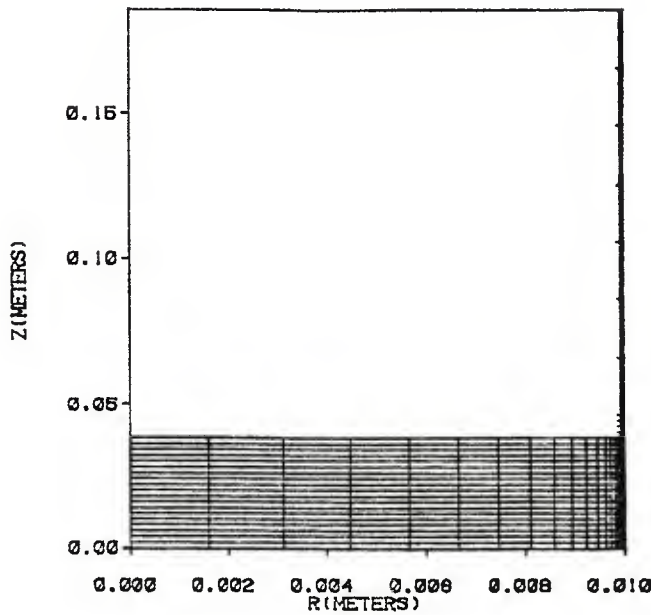


Figure 15. Mesh configuration for the standard resolution calculation of flow with a 1% gap. There are 20 cells along the gap and three cells across its width. The mesh below the shell is identical to that used in the first calculation.

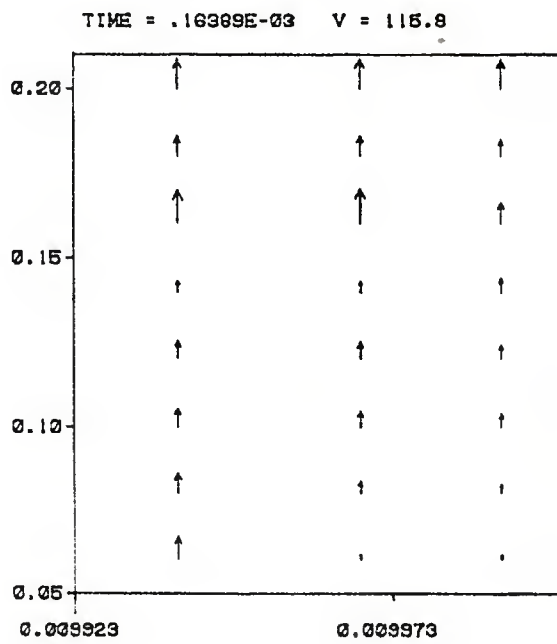
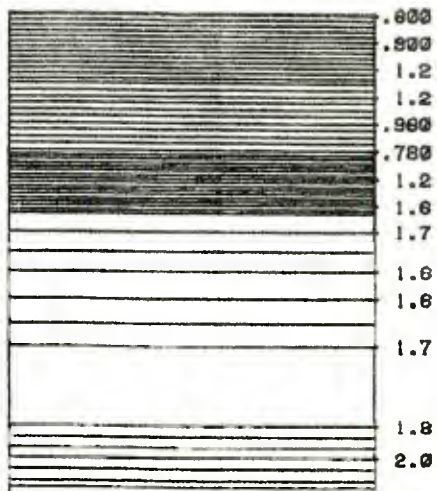
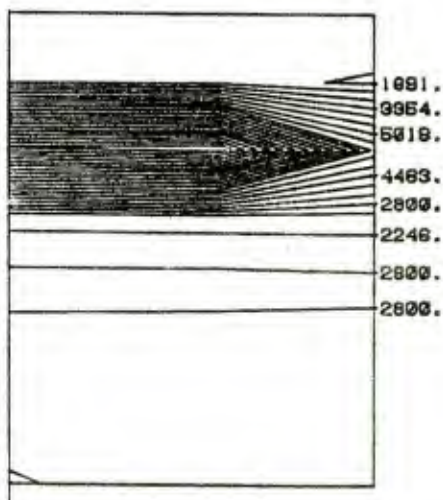


Figure 16. Velocity vectors in the gap region on the last cycle before the code diverged when the outlet conditions were 90% sonic plus shell speed. The radial coordinate has been expanded by a factor of 2000. The top row of vectors is at the outlet and have just reached the sonic speed. Since this is a prescribed row, not a calculated one, this is not the source of trouble, but the third row has gone slightly supersonic and exceeded the range of validity of the method.



PRESSURE CONTOURS AT TIME = .10309E-03

Figure 17. Pressure contours for the same case described in Figure 16. A shock, with overshoot ringing, has formed at the middle of the "1.2" contour lines near the exit. The shock and an attendant rarefaction are clearly seen by the bunching of the contour lines.



TEMPERATURE CONTOURS AT TIME = .10309E-03

Figure 18. Temperature contours for the same case described in Figure 16. The extremely high temperature spike is just upstream of the shock as expected. The value of the temperature is meaningless because the method is not intended to capture shocks.

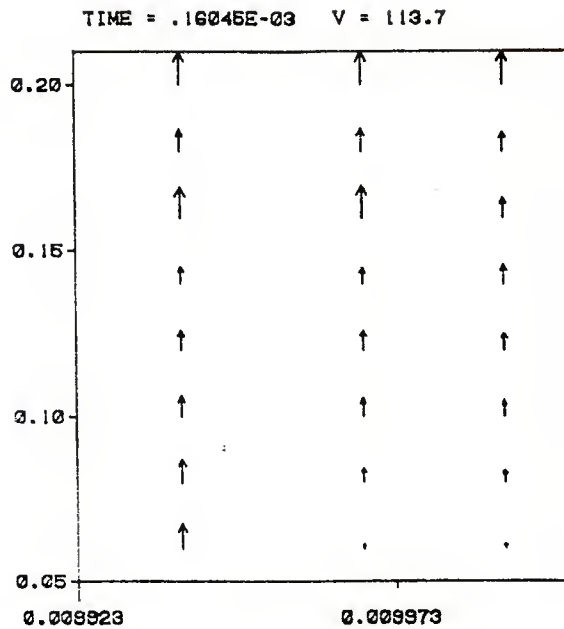


Figure 19. Velocity vectors in the gap region just before the code diverged in the case when the outlet velocity was 90% of sonic speed in the absolute frame of reference. The radial coordinate has been expanded by a factor of 2000. The internal flow has been sped up to a supersonic value by the construction of the wall boundary layer and the backflow at the gap inlet.

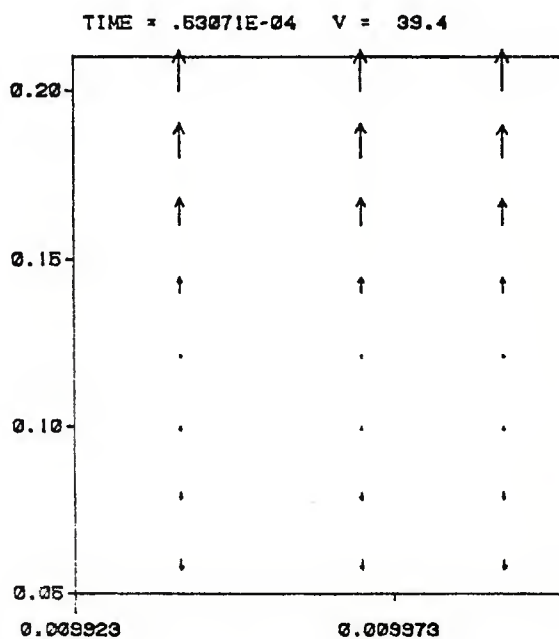


Figure 20. Flow in gap when outlet velocity is 50% sonic. Radial coordinate expanded 2000 times. The rarefaction wave from the outlet has propagated about $1200 \text{ m/sec} \times 0.5 \times 10^{-4} \text{ sec} \approx .06 \text{ m}$ and the flow correspondingly accelerated to near the exit velocity.

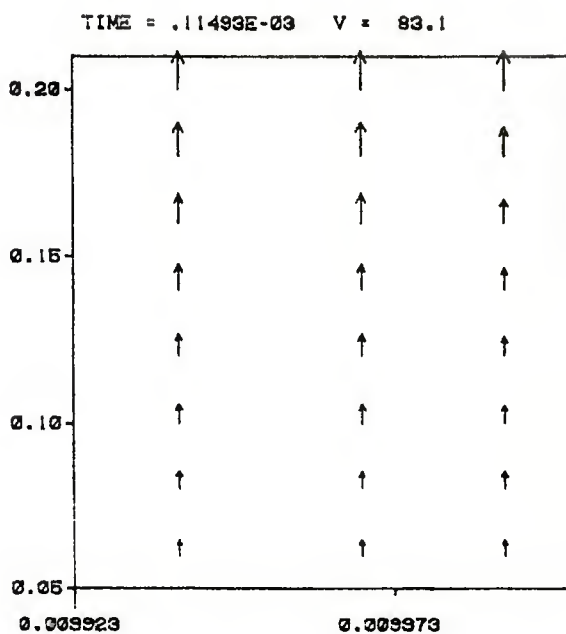


Figure 21. Flow in gap under conditions described in Figure 21. The expansion wave has traveled most of the gap and the flow is uniform in the radial direction with the maximum value at the exit.

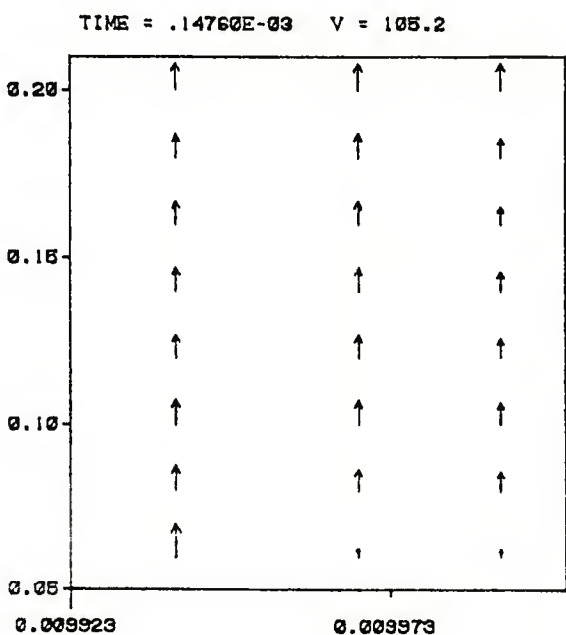


Figure 22. Flow in gap under conditions described in Figure 20. Boundary layer development along the wall has forced the flow inward toward the shell where it is accelerated to a value that exceeds the exit speed.

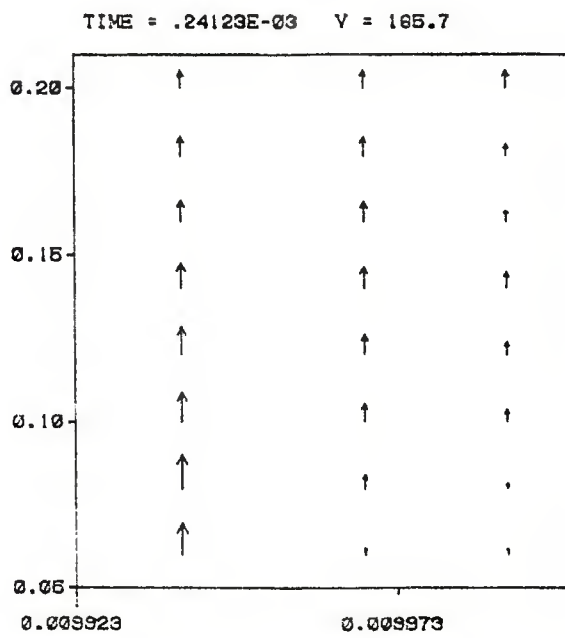


Figure 23. Flow in gap under conditions described in Figure 20. Maximum flow rate achieved due to constriction of wall boundary layer. Maximum velocity nearly twice exit speed.

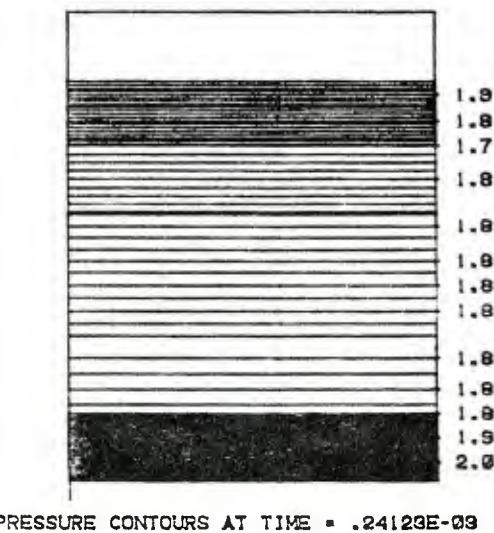
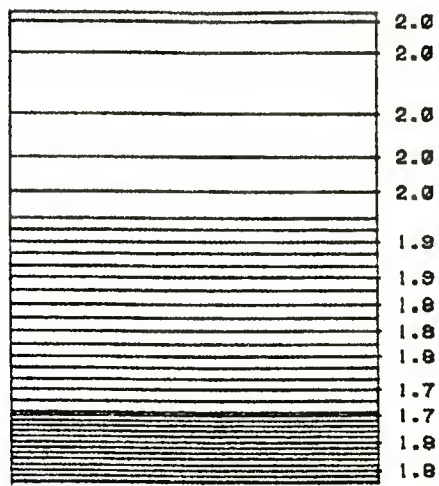


Figure 24. Pressure contours at same time shown in Figure 23. Flow is still being accelerated up the gap due to a higher pressure in the firing chamber.



PRESSURE CONTOURS AT TIME = .32519E-03

Figure 25. Pressure contours in gap under conditions described in Figure 20 at a time just after the maximum internal velocity is achieved. The wall boundary layer is still growing and constricting the flow but the chamber pressure is now lower than the exit so the flow is being decelerated. At this moment the two trends are nearly in balance so the maximum is held.

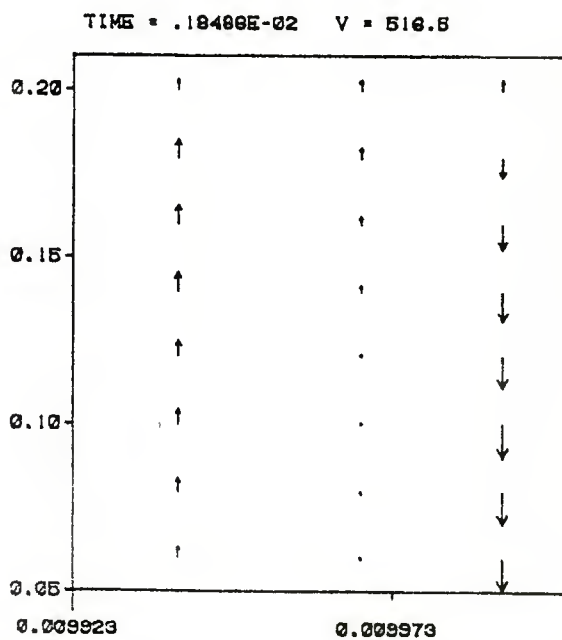


Figure 26. Flow in the gap at late times under conditions described in Figure 20. Boundary layer is only growing slowly and pressure drop is nearly zero so that maximum flow velocity has settled on about the outlet value. Note that flow reverses at first cell from the inlet, indicating that uniform outlet velocity is probably not correct.

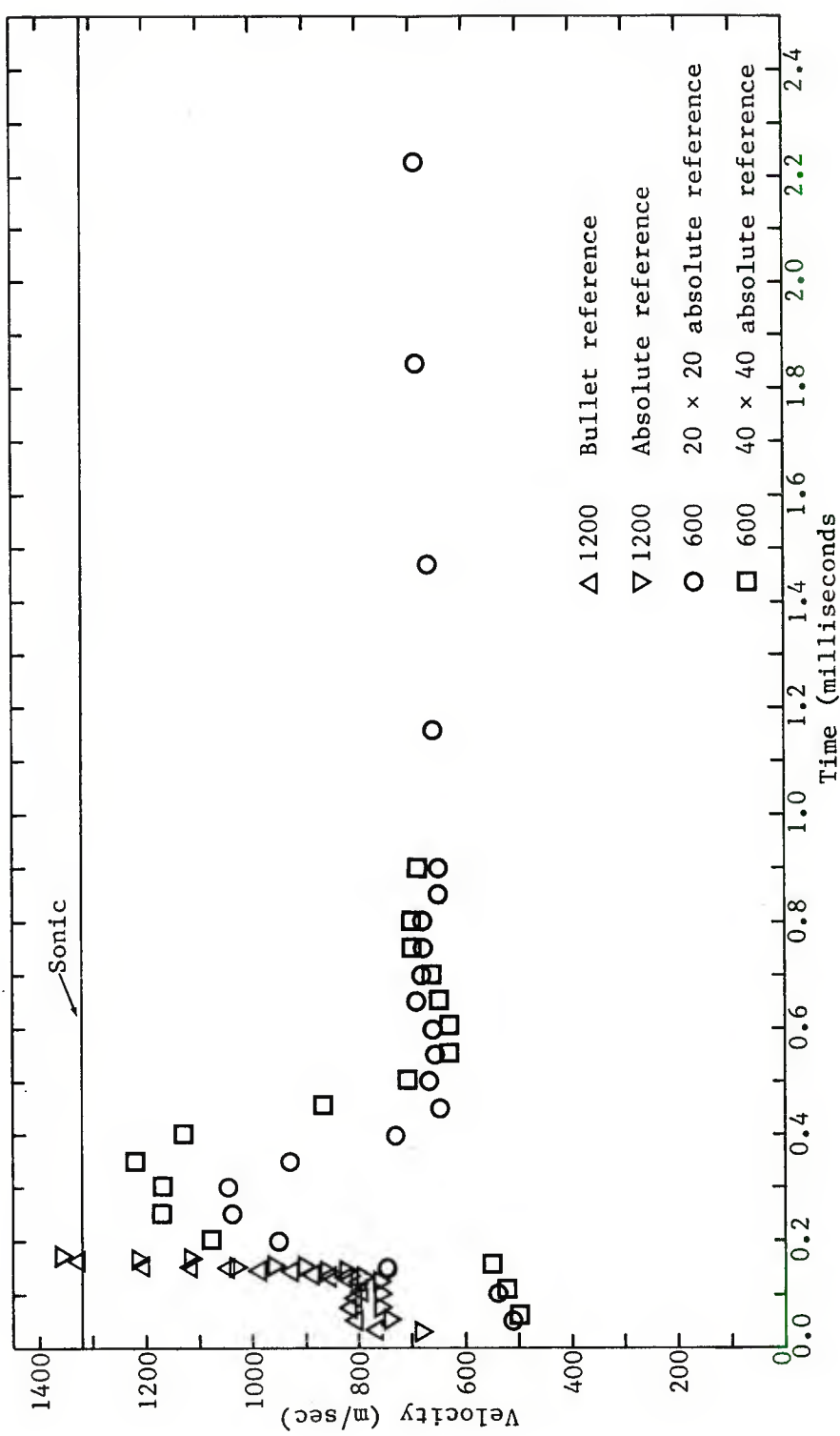


Figure 27. Maximum velocity in the gap, not counting the applied outlet value, for the cases discussed in the previous figures.

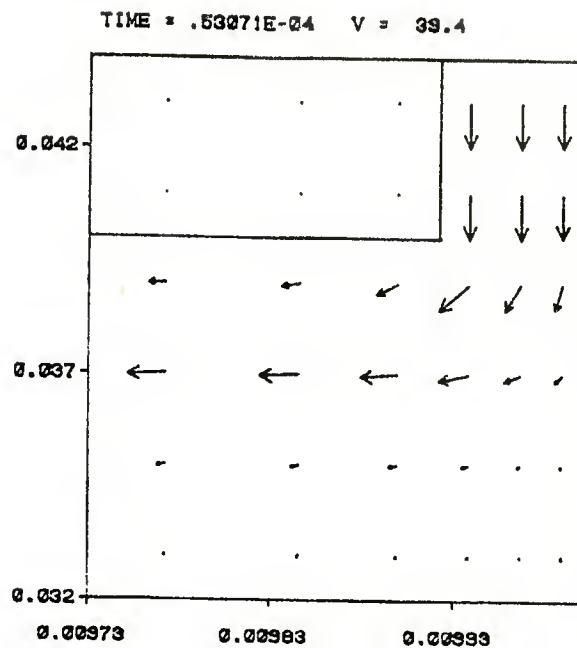


Figure 28. Flow in the vicinity of the corner for 20 mm diameter barrel with 1% gap. Radial coordinate and velocity proportionately exaggerated. At early times acceleration of shell causes a local flow pressure to develop at the base of the shell which draws gas in from the gap.

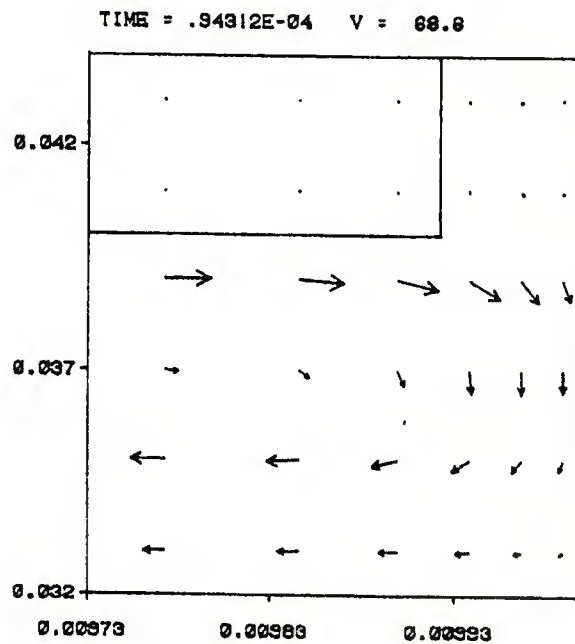


Figure 29. Flow in vicinity of corner for same conditions described in Figure 28. After gas is drawn out of gap the pressure lowers to a point in equilibrium with the chamber and no further flow occurs. Recirculation eddy generated by initial motion persists.

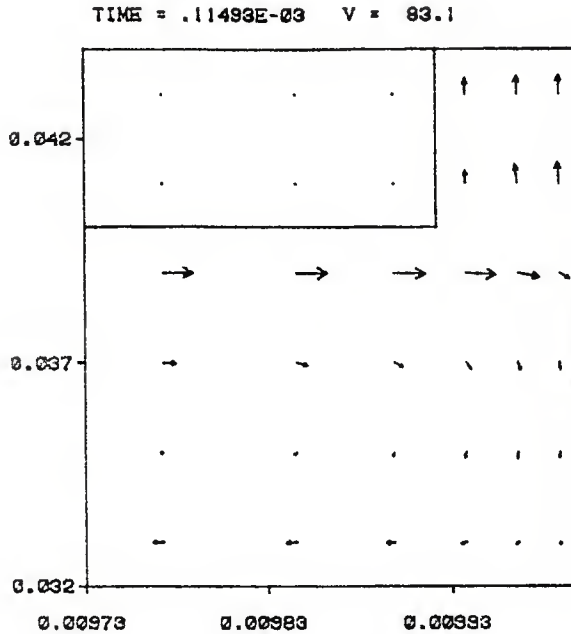


Figure 30. Flow in the vicinity of the corner for the same conditions described in Figure 28. As gas is vented from exit of gap, pressure is lowered below that in the chamber and flow is pulled into the gap. The radial flow across the bottom of the shell splits into part moving in the wall boundary layer and part entering the gap.

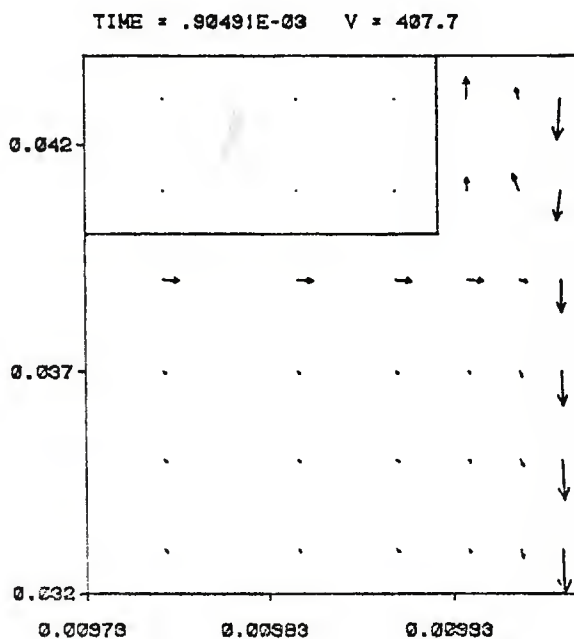
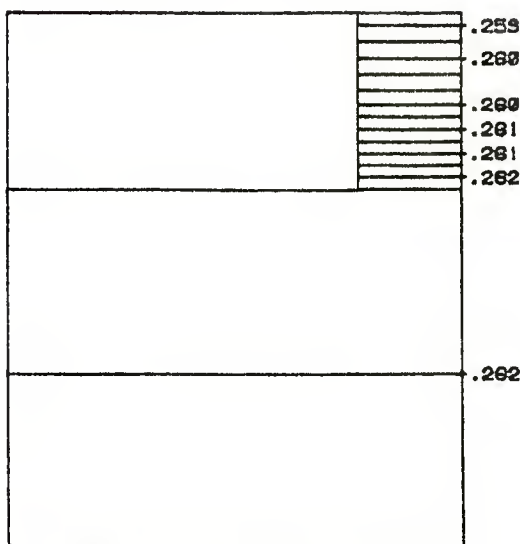
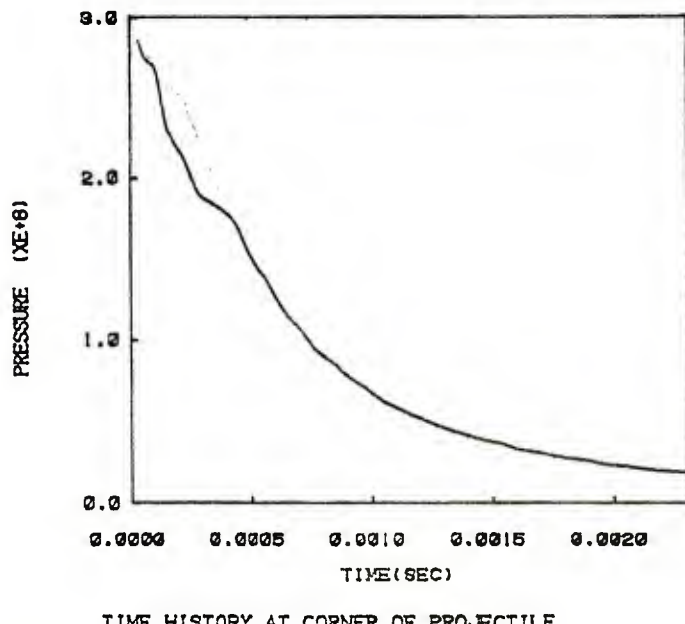


Figure 31. Flow in the vicinity of the corner for the same conditions described in Figure 28. The flow pattern is now fully developed. It is similar to that with no gap except that the radial flow is increased to be able to supply that leaking around the shell.



PRESSURE CONTOURS AT TIME = .1848E-02

Figure 32. Pressure contours in the vicinity of the corner for the case described in Figure 28. At late times the pressure is nearly uniform within the chambers, with the gap being at a lower value.



TIME HISTORY AT CORNER OF PROJECTILE

Figure 33. Time history of pressure at the corner of shell and centerline for 20 mm diameter barrel with 1% gap (— corner; - - - centerline). Because of the expansion flow into the gap, the corner has a lower pressure than the centerline until equilibrium is established. This is in contrast to the no gap case where the pressures were identical.

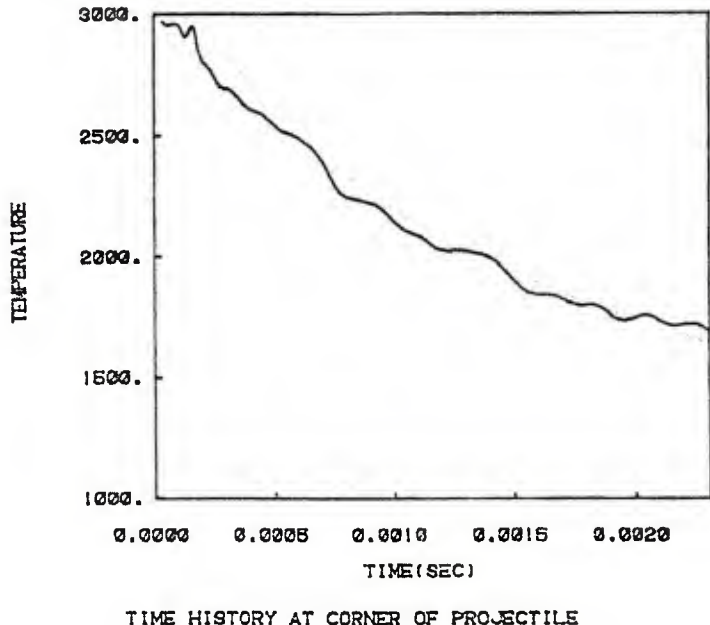


Figure 34. Time history of temperature at the corner of the shell and at the centerline for a 20 mm diameter barrel with a 1% gap. (— corner; - - - centerline). The complexity of the flowfield near the corner affects the viscous heating which varies considerably as the flow develops. Because the wall flow originates from gas ahead of the shell, it will strongly depend on the outlet boundary conditions.

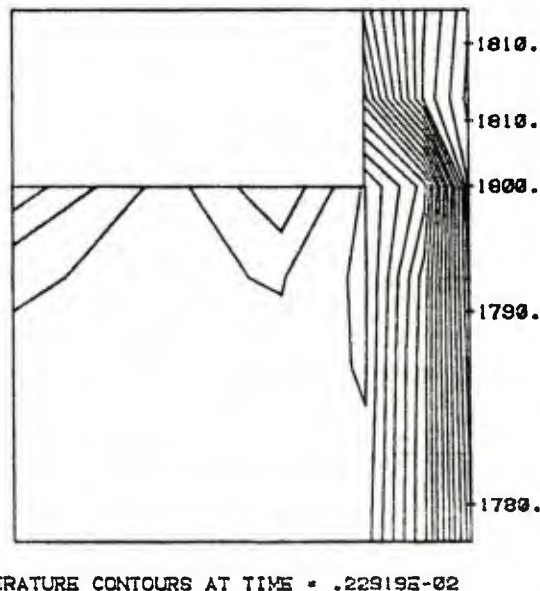


Figure 35. Temperature contours at late time for 20 mm barrel with a 1% gap. Viscous heating in the wall boundary layer dominates the field, but the wall temperature at the wall is 150°C higher than the no gap case because the boundary layer is not totally derived from the circulating chamber flow. The temperature at the corner of the shell, however, is nearly the same as in the no gap case.

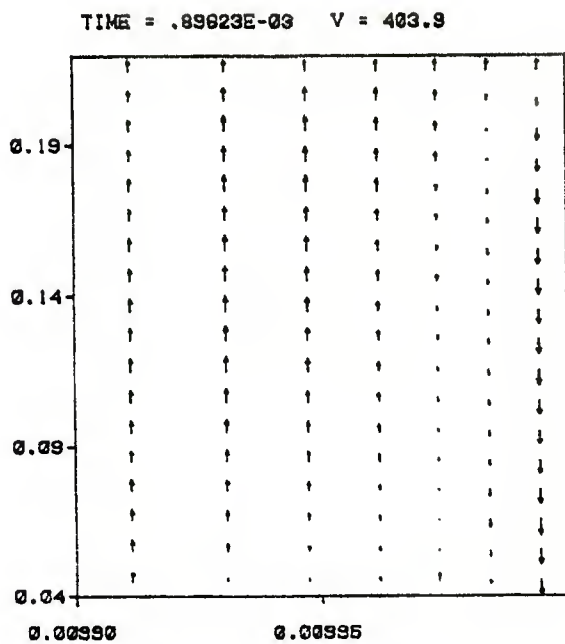


Figure 36. High resolution calculation of flow in the gap for a 20 mm barrel with a 1% gap. Boundary layers on both the wall and the shell can be seen.

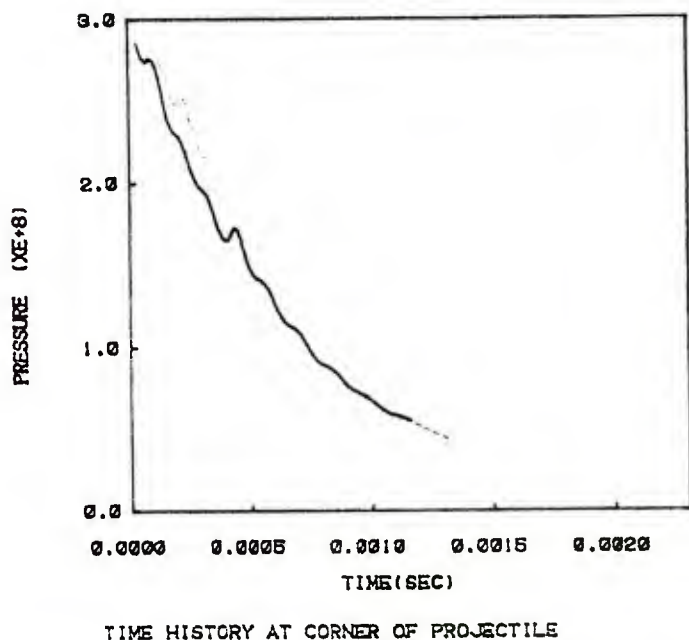
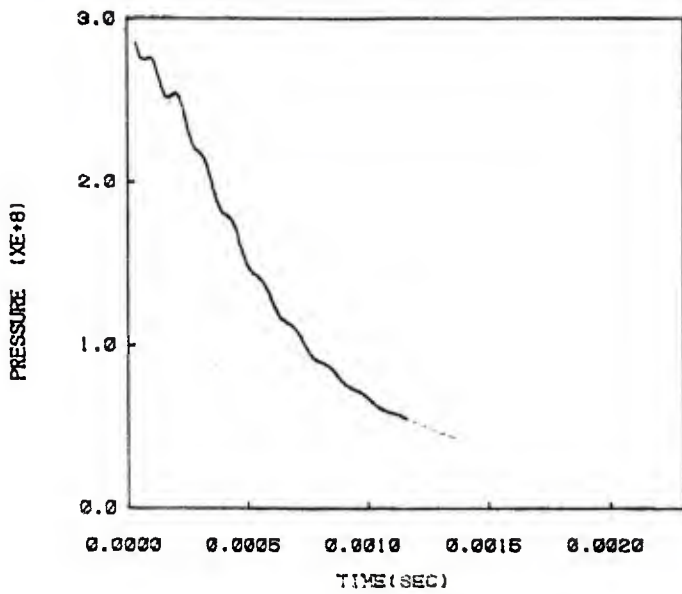
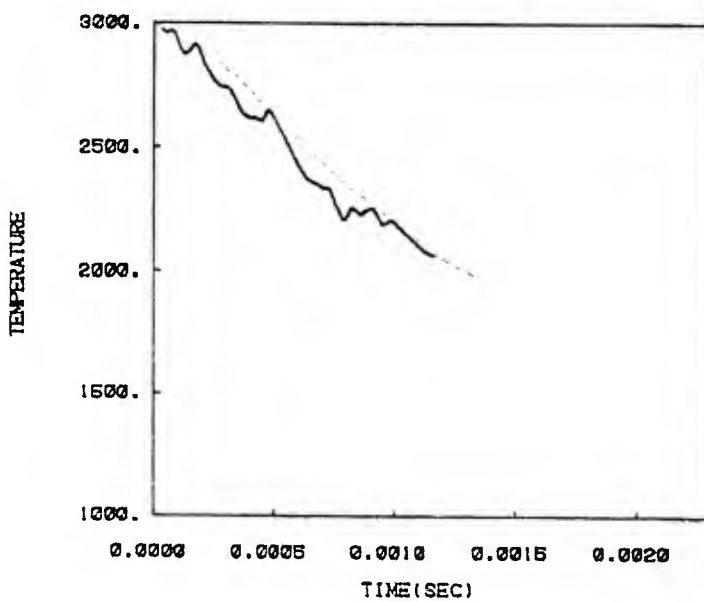


Figure 37. Time history of pressure at corner of shell for 20 mm barrel with 1% gap (— 40 x 40 mesh; --- 20 x 20 mesh). Differences are primarily due to details of the flow about the corner during the backflow and reentry stages of development.



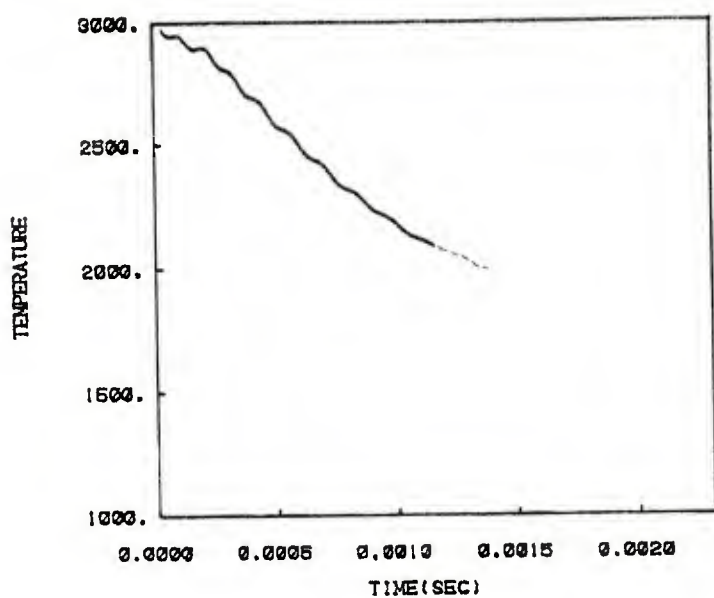
TIME HISTORY AT CENTERLINE AT BASE OF PROJECTILE

Figure 38. Time history of pressure at base on centerline for 20 mm barrel with 1% gap (— 40 x 40 mesh; - - - 20 x 20 mesh). Results are essentially the same and differ only in the magnitude of the early time gas dynamics oscillations.



TIME HISTORY AT CORNER OF PROJECTILE

Figure 39. Time history of temperature at the corner of shell for a 20 mm barrel with a 1% gap (— 40 x 40 mesh; - - - 20 x 20 mesh). As with the pressure, the differences lie in the details of the flow field which governs the viscous heating rate. The wall temperatures at the corner could be 150°C higher than in the no gap case.



TIME HISTORY AT CENTERLINE AT BASE OF PROJECTILE

Figure 40. Time history of temperature at base centerline for 20 mm barrel with a 1% gap (— 40 x 40 mesh; --- 20 x 20 mesh). Results are identical with the no gap case.

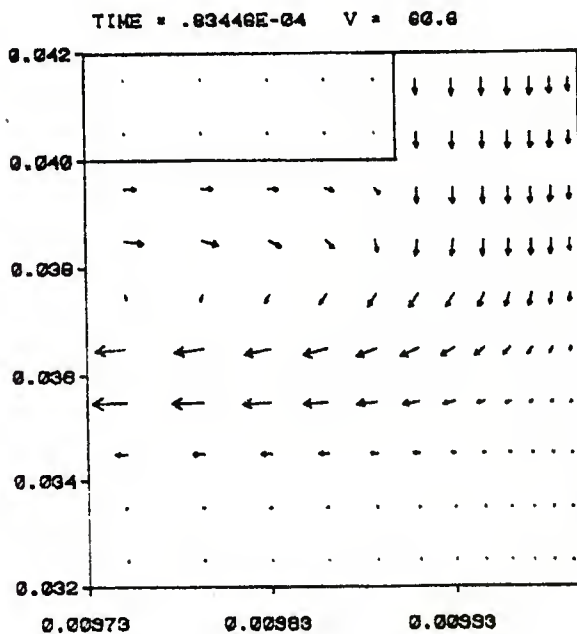


Figure 41. Flow pattern in the vicinity of the corner for the case of a 20 mm barrel with a 1% gap. The radial coordinate has been greatly expanded. Early time flow shows the backflow from the gap into the rarefaction created by the shell's acceleration. In this higher resolution calculation the separated flow from the corner is clearly seen.

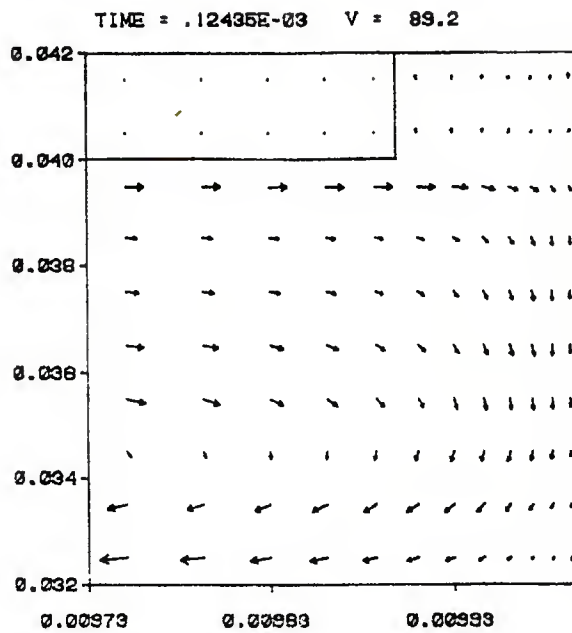


Figure 42. Flow pattern in the vicinity of the corner for the case described in Figure 1. This is the moment that the pressure in the gap has dropped to that of the chamber and reentry flow is about to begin. The recirculation vortex caused by the backflow is well developed.

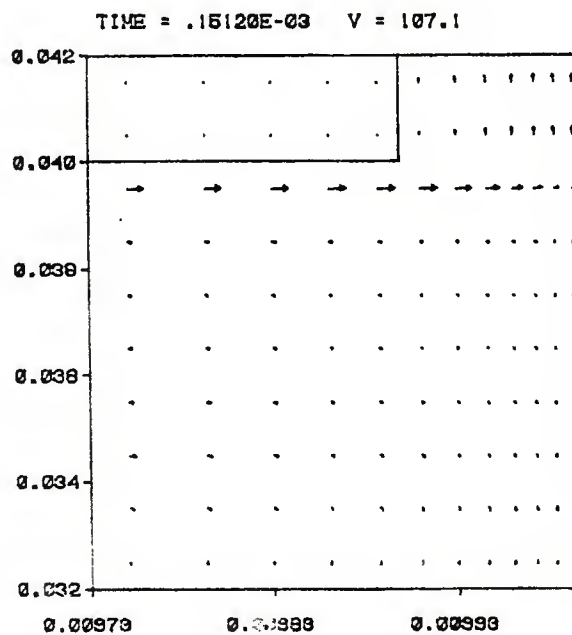


Figure 43. Flow pattern in the vicinity of the corner for the case described in Figure 41. Flow across the shell base is established and it splits into the gap and wall layer streams.

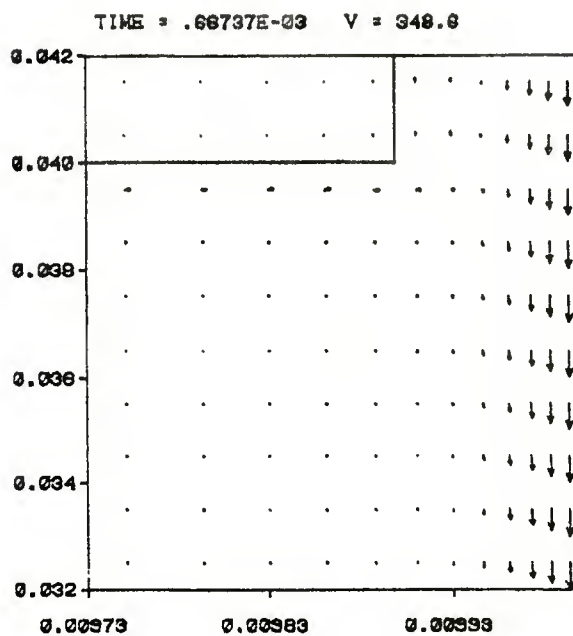


Figure 44. Flow pattern in the vicinity of the corner for the case described in Figure 41. The wall boundary layer is established and well resolved.

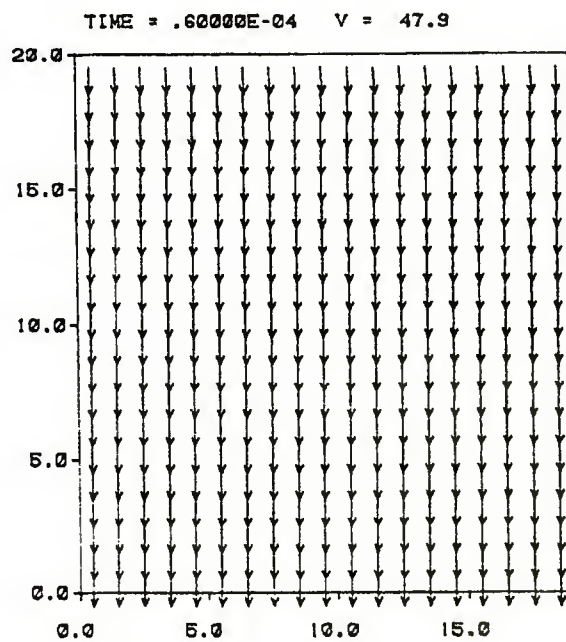


Figure 45. Whole field visualization of flow in 20 mm no gap case. All vectors have been expanded to fill their computational cell and all cells have been expanded to a square array. At this early instant flow is leaving the computational region as the gas lags the shell's motion.

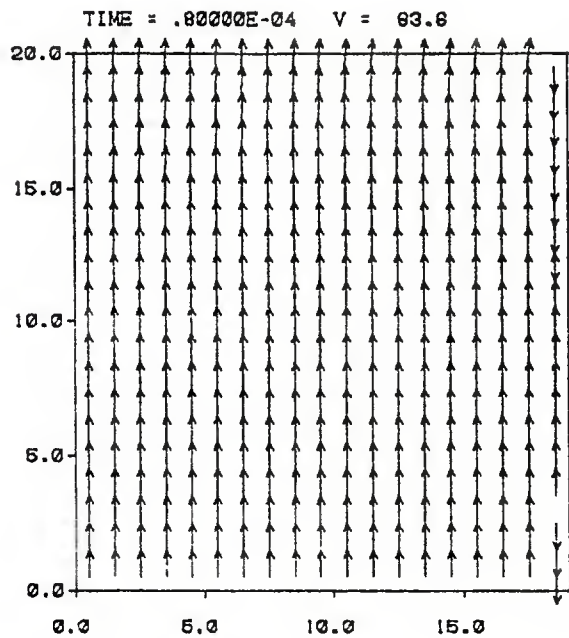


Figure 46. See caption for Figure 45. Flow reversal occurs throughout the field, probably the result of a rarefaction wave set up at the shell. An inconsistency between the calculated shell velocity and the prescribed pressure boundary condition may be a source.

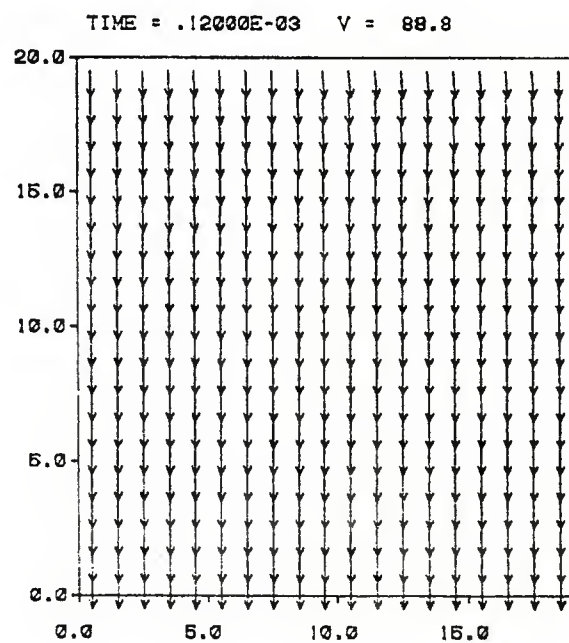


Figure 47. See caption for figure 45. Flow returns to normal direction as rarefaction wave leaves system.

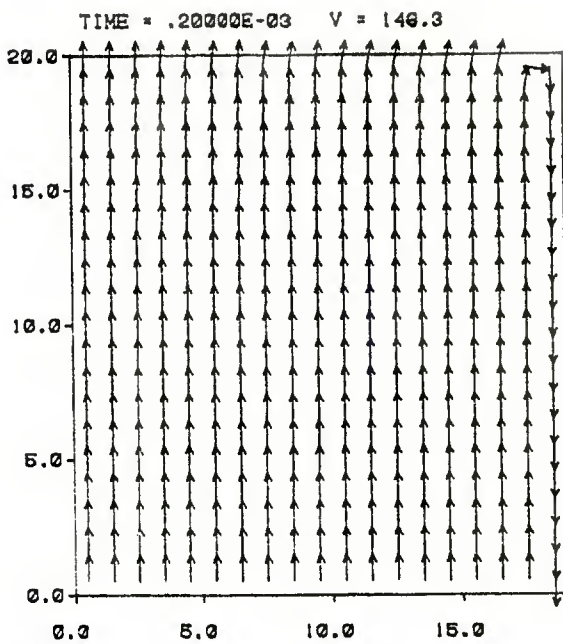


Figure 48. See caption for Figure 45. A second flow reversal accompanies another rarefaction wave.

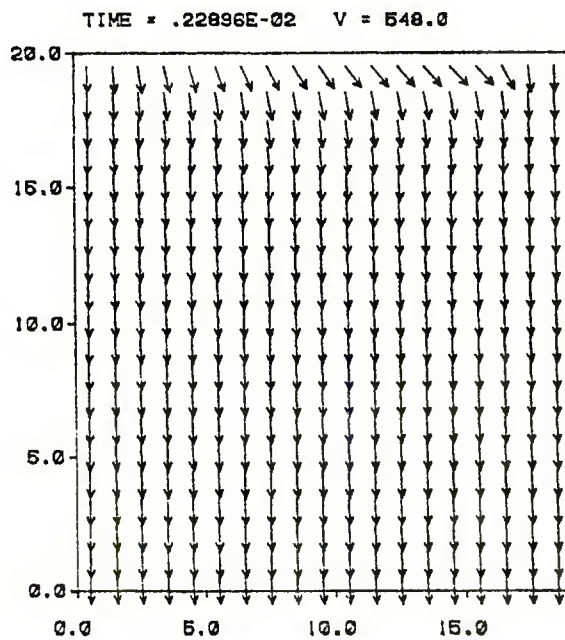


Figure 49. See caption for Figure 45. At late times flow pattern settles down to an outflow expansion which is directed slightly toward the outer wall to feed the wall boundary layer.

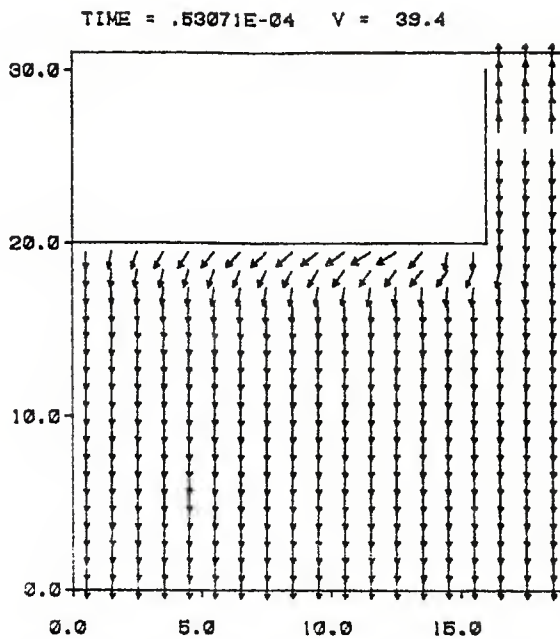


Figure 50. Whole field visualization for 20 mm, 1% gap case with standard resolution. The backflow from the gap can be seen and the first stages of a separation region. A local rarefaction in the gap develops as flow exits both ends of the gap.

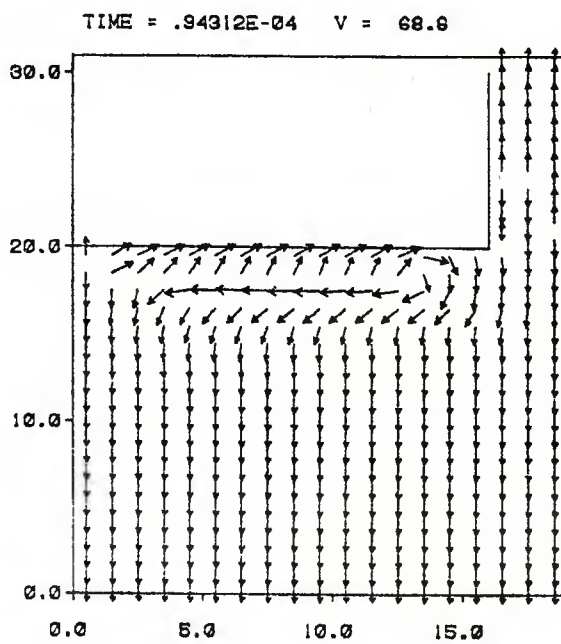


Figure 51. See caption for Figure 50. The flow separation region at the corner is well developed and the wall boundary layer has been established up to the corner

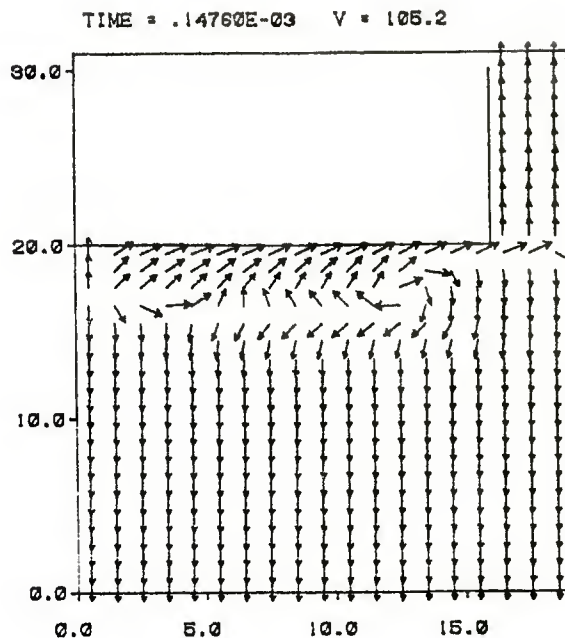


Figure 52. See caption for Figure 50. The recirculation eddy has been pushed from the base of the shell as flow into the gap is established. A local rarefaction has formed in the fifth row below the shell.

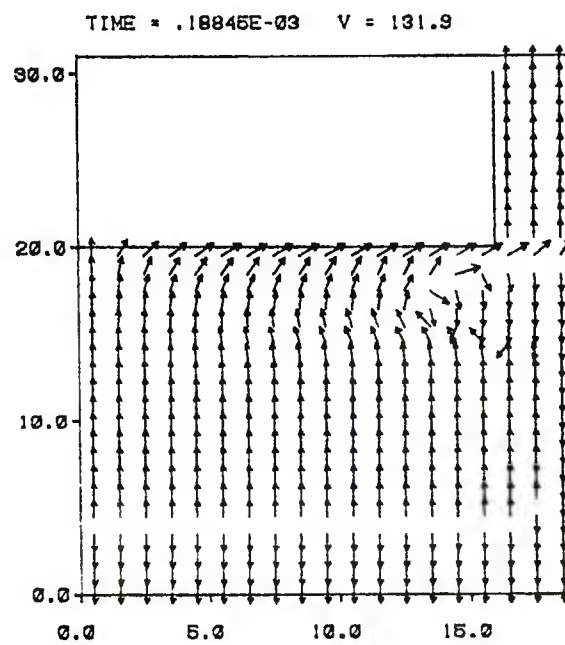


Figure 53. See caption for Figure 50. Downward flow is being reestablished by the upper propagating rarefaction wave. The separation eddy is smaller and nearly diffused.

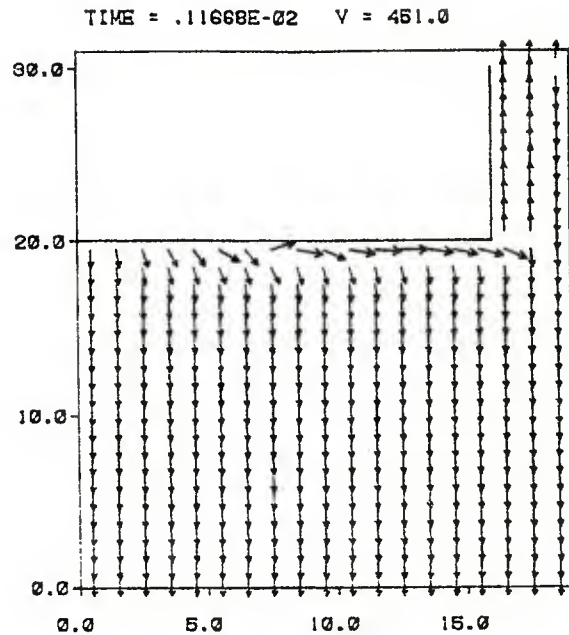


Figure 54. See caption for Figure 50. Final flow pattern is established with flow splitting of the base flow into the gap and the wall boundary layer.

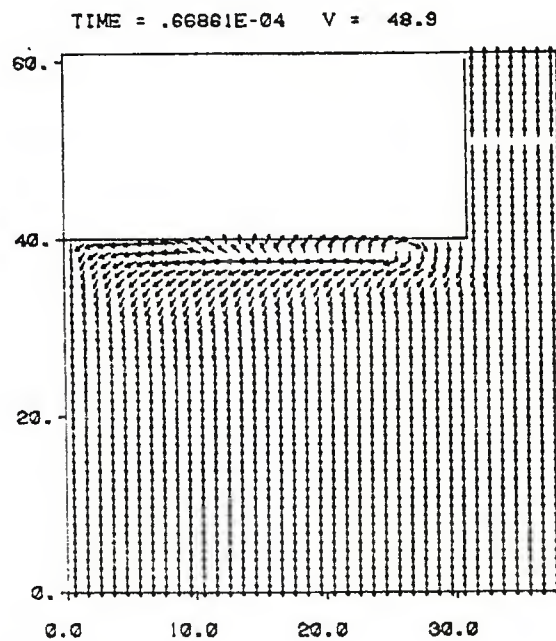


Figure 55. Whole field visualization for the 20 mm, 10% gap case with high resolution. The backflow from the gap has begun with a small recirculation just forming along the base. A rarefaction has formed in the gap due to the outflow at both ends.

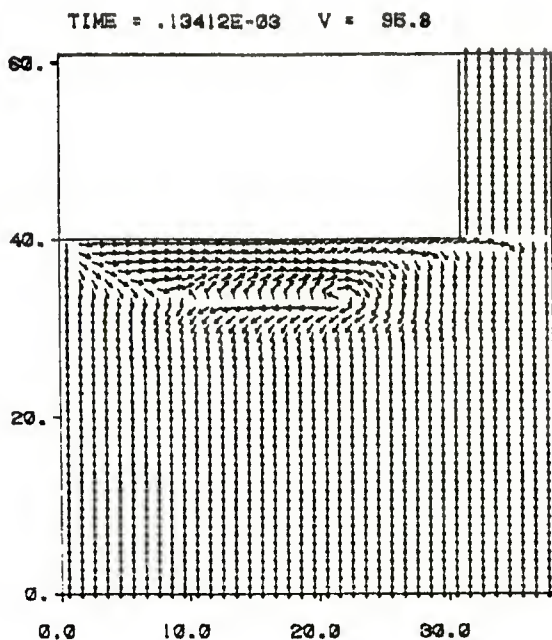


Figure 56. See caption for Figure 55. The recirculation region at the base of the shell has expanded and flow splitting at the gap has begun.

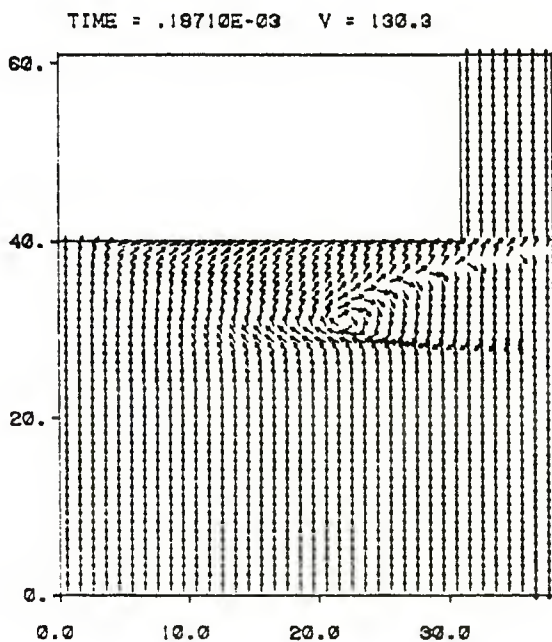


Figure 57. See caption for Figure 55. Flow reversal in the chamber has occurred and the recirculation eddy has been shed from the base of the shell.

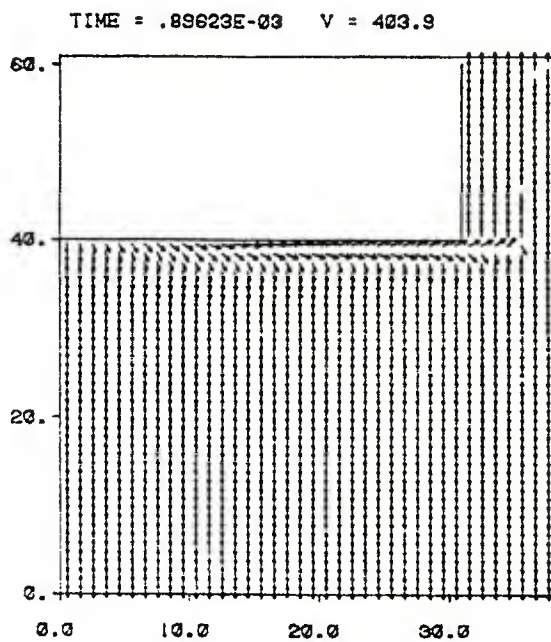


Figure 58. See caption for Figure 55. The flow is approaching its final pattern. The expansion flow is away from the shell and the flow splitting into the gap and the boundary layer are clearly seen.

APPENDIX A

MATHEMATICAL MODELS AND NUMERICAL ALGORITHMS

NOMENCLATURE

| | |
|------------------|---|
| a | acceleration of the projectile (m/sec^2) |
| E | energy (J/kg) |
| I | index of rightmost column |
| i | index denoting cell columns |
| J | index of topmost row |
| j | index denoting cell rows |
| M | mass of the projectile (kg) |
| n | index denoting time level |
| p | pressure (N/m^2) |
| r | radial distance (m) |
| T | temperature |
| t | time (sec) |
| δt | time increment (sec) |
| u | radial velocity (m/sec) |
| v | axial velocity (m/sec) |
| V | projectile velocity (m/sec) |
| z | axial distance (m) |
| ρ | density (kg/m^3) |
| μ | viscosity of fluid |
| λ | viscosity coefficient |
| γ | ratio of specific heats, value used was 1.27118. |
| σ | turbulent thermal diffusivity (m^2/sec) |
| $\Delta A_{i,j}$ | area of computational cell i,j (m^2) |

GOVERNING EQUATIONS

The equations assumed to describe the expanding flow within the barrel of the gun are the compressible Navier-Stokes equations written in axisymmetric cylindrical polar coordinates, plus an appropriate equation of state to close the system. These equations are:

Continuity:

$$\frac{\partial \rho}{\partial t} + \frac{1}{r} \frac{\partial}{\partial r} (\rho u r) + \frac{\partial}{\partial z} (\rho v) = 0 \quad (1)$$

Radial momentum:

$$\begin{aligned} \frac{\partial}{\partial t} (\rho u) + \frac{1}{r} \frac{\partial}{\partial r} (\rho u^2 r) + \frac{\partial}{\partial z} (\rho u v) = & - \frac{\partial p}{\partial r} + \frac{2}{r} \frac{\partial}{\partial r} \left(\mu r \frac{\partial u}{\partial r} \right) - \frac{2\mu}{r^2} u \\ & + \frac{\partial}{\partial z} \left[\mu \left(\frac{\partial v}{\partial r} + \frac{\partial u}{\partial z} \right) \right] + \frac{\partial}{\partial r} (\lambda \Delta) \end{aligned} \quad (2)$$

Axial momentum:

$$\begin{aligned} \frac{\partial}{\partial t} (\rho v) + \frac{1}{r} \frac{\partial}{\partial r} (\rho u v r) + \frac{\partial}{\partial z} (\rho v^2) = & - \frac{\partial p}{\partial z} + \frac{1}{r} \frac{\partial}{\partial r} \left[\mu r \left(\frac{\partial u}{\partial z} + \frac{\partial v}{\partial r} \right) \right] \\ & + 2 \frac{\partial}{\partial z} \left(\mu \frac{\partial v}{\partial z} \right) + \frac{\partial}{\partial z} (\lambda \Delta) \end{aligned} \quad (3)$$

Energy:

$$\begin{aligned} \frac{\partial}{\partial t} (\rho E) + \frac{1}{r} \frac{\partial}{\partial r} (r u \rho E) + \frac{\partial}{\partial z} (v \rho E) = & \frac{\gamma}{\sigma} \left[\frac{1}{r} \frac{\partial}{\partial r} (r u \frac{\partial E}{\partial r}) + \frac{\partial}{\partial z} \left(\mu \frac{\partial E}{\partial z} \right) \right] - p \Delta \\ & + \mu^2 \frac{\partial u}{\partial r}^2 + \frac{\partial v}{\partial r}^2 + \frac{\partial u}{\partial z}^2 + 2 \frac{\partial v}{\partial z}^2 + 2 \frac{u}{r}^2 + \lambda \Delta^2 \end{aligned} \quad (4)$$

where

$$\Delta = \frac{1}{r} \frac{\partial}{\partial r} (ru) + \frac{\partial v}{\partial z} \quad (5)$$

Nobel-Abel Equation of State:

$$p = p(\rho, E)$$

$$p = \frac{(\gamma - 1)\rho E}{1 - \epsilon_c \rho} \quad \epsilon_c = 0.0010775 \text{ m}^3/\text{kg} \quad (6)$$

Ballistic Calculation:

$$F = Ma \quad (7)$$

The viscosity coefficient, μ , is either calculated from Sutherland formula

$$\mu = \frac{4.0608 \times 10^{-8} E^{3/2}}{E + 1.4232 \times 10^5}$$

or μ from the $k-\epsilon$ turbulence model of Pope and Whitelaw, or μ is taken as a constant. The viscosity coefficient λ is equal to $-2/3 \mu$.

Due to the desire to keep the calculation domain constant, a transformation to the coordinate system fixed with respect to the moving shell is incorporated into these equations in the following manner. In the barrel fixed system, the shell moves past stationary walls with a velocity V , creating a gas velocity v . This is the axial velocity in Eqs. (1)-(5). In the shell fixed frame of reference, the shell is stationary, but the gun barrel now moves past the shell with velocity $-V$. The axial gas velocity seen in this frame is $v_b = v - V$. Hence, the transformation of the equation can be made by

$$r_b = r$$

$$z_b = z - \int_0^t V(t') dt'$$

$$u_b = u$$

$$v_b = v - V$$

$$t_b = t$$

If this transformation is used in Eqs. (1)-(5), the only change which occurs is seen in the axial momentum equation; all the other equations remain the same, but with the subscript b appended to each variable. The axial momentum equation is altered by the addition of one term which accounts for the unsteady motion of the shell. Dropping all the subscripts which appear in the equation due to the transformation, the axial momentum equation in the shell fixed coordinate system is

$$\begin{aligned} \frac{\partial}{\partial t} (\rho v) + \frac{1}{r} \frac{\partial}{\partial r} (\rho u v r) + \frac{\partial}{\partial z} (\rho v^2) = - \rho \frac{dV}{dt} - \frac{\partial p}{\partial z} + \frac{1}{r} \frac{\partial}{\partial r} [\mu r (\frac{\partial u}{\partial z} + \frac{\partial v}{\partial r})] \\ + 2 \frac{\partial}{\partial z} (\mu \frac{\partial v}{\partial z}) + \frac{\partial}{\partial z} (\lambda \Delta) . \end{aligned} \quad (3-A)$$

Equations (1)-(7), with Eq. (3) replaced by Eq. (3-A), are the governing equations solved by JAYCOR's SAGITA code.

FINITE DIFFERENCE EQUATIONS

An extended version of the Implicit Continuous-fluid Eulerian (ICE) technique of Harlow and Amsden⁽¹⁾ for compressible flow is used in JAYCOR's SAGITA code which is one application of the EITACC methodology.⁽²⁾

A fragment of the Eulerian finite-difference mesh is shown in Fig. 1, which illustrates the centering of the field variables relative to a typical cell. The index i counts cell centers from left to right, while j counts them from bottom to top. δr_i and δz_i are the lengths of a cell.

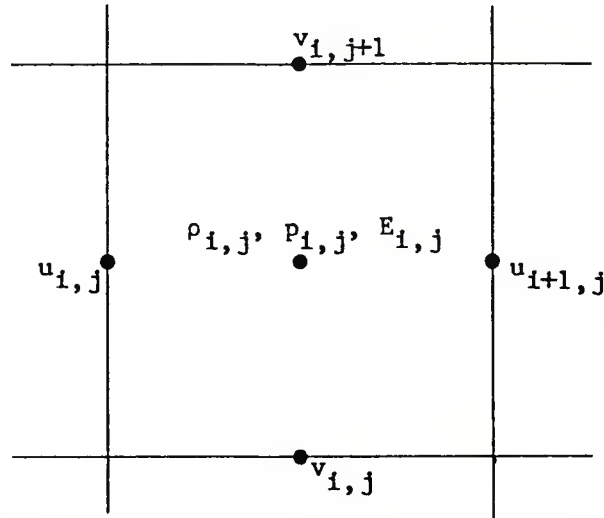


Figure 1. Layout of Variables and Indices in the Mesh.

The form of the finite difference equations are as follows:

Ballistic Calculation:

$$v^{n+1} = v^n + \frac{\delta t}{M} \sum_{i,j} p_{i,j}^{n+1} \Delta A_{i,j} \quad (8)$$

Continuity:

$$\rho_{i,j}^{n+1} = \rho_{i,j}^n + \delta t \phi \frac{\partial \rho}{\partial t}_{i,j}^{n+1} \quad (9)$$

Momentum:

$$(\rho u)_{i,j}^{n+1} = (\rho u)_{i,j}^n + \delta t \frac{\partial}{\partial t} (\rho u)_{i,j}^n - \frac{\partial p}{\partial r}_{i,j}^{n+1} \quad (10)$$

$$(\rho v)_{i,j}^{n+1} = (\rho v)_{i,j}^n + \delta t \frac{\partial}{\partial t} (\rho v)_{i,j}^n - \frac{\partial p}{\partial z}_{i,j}^{n+1} \quad (11)$$

Energy:

$$(\rho E)_{i,j}^{n+1} = (\rho E)_{i,j}^n + \delta t \frac{\partial}{\partial t} (\rho E)_{i,j}^n \quad (12)$$

where the index $n+1$ indicates the advanced-time value. The [] means that the pressure is not included in this momentum derivative term.

In order to eliminate the sonic speed stability limitation, the pressure must be implicitly included in the calculation procedure. This is accomplished by incorporating the values of the flux at the forward time step, Eqs. (10) and (11), into the continuity equation (1) as follows: In shorthand vector notation, where $\underline{w} = (u, v)$, we have

$$\frac{\partial \rho}{\partial t}_{i,j}^n + \text{div}(\rho \underline{w})_{i,j}^{n+1} = 0$$

or

$$\frac{\partial \rho}{\partial t}_{i,j}^n + \text{div}[\rho \underline{w}]_{i,j}^{n+1} - \delta t \text{div grad } p_{i,j}^{n+1} = 0 \quad (13)$$

This gives an equation for the new pressures, $p_{i,j}^{n+1}$, when (10) and (11) are substituted in (13).

SOLUTION PROCEDURE

The specific steps which comprise one calculation cycle are as follows:

1. From known values at time step n, and the latest iterated values at n+1 compute

$$v^{n+1} \quad \text{from Eq. (8)}$$

$$\rho_{i,j}^{n+1} \quad \text{from Eq. (9)}$$

$$(\rho u)_{i,j}^{n+1} \quad \text{without the } \delta t \frac{\partial p}{\partial r}_{i,j}^{n+1} \text{ term from Eq. (10)}$$

$$(\rho v)_{i,j}^{n+1} \quad \text{without the } \delta t \frac{\partial p}{\partial z}_{i,j}^{n+1} \text{ term from Eq. (11)}$$

$$(\rho E)_{i,j}^{n+1} \quad \text{from Eq. (12)}$$

2. These values at n+1 are placed in the Poisson Eq. (13). This equation is then solved for $p_{i,j}^{n+1}$ by a direct method,⁽³⁾ rather than SOR, to avoid slow or non-convergence problems caused by high aspect ratio finite difference meshes.

3. These values of $p_{i,j}^{n+1}$ are used to complete the calculations of $(\rho u)_{i,j}^{n+1}$ and $(\rho v)_{i,j}^{n+1}$ in Eqs. (10) and (11).

4. After steps 1-3, V, ρ , ρu , ρv , ρE , p are now defined at the new time step n+1. These are compared with the previous iterated values. If convergence is obtained then continue to the next calculation cycle; otherwise, repeat the above steps.

INITIAL CONDITIONS

The initial conditions were taken from the BRL computer run output sent as an attachment to ARRADCOM letter dated 20 December 1979. These initial conditions are as follows:

$p = 3.0 \times 10^8 \text{ N/m}^2$ everywhere in the computational mesh.

$\rho = 218.66 \text{ kg/m}^3$ everywhere in the computational mesh.

ρE in J/m^3 is computed from the equation of state for every cell in the computational mesh.

$\rho u = 0.0 \text{ kg/m}^2\text{-sec}$ everywhere in the computational mesh.

$\rho v = 0.0$ everywhere in the computational mesh.

BOUNDARY CONDITIONS

Boundary conditions are derived in such a way as to describe the various walls or surfaces that may occur. Below is the description of the various boundary conditions used at the centerline (left of the computational mesh), at the wall of the gun (right of the computational mesh), 4 cm away from the projectile base (bottom of computational mesh), and at the projectile base (top of computational mesh). I and J represent the total number of columns and rows used, with columns $i = 1$ and I and $j = 1$ and J being boundary cells outside the physical domain.

Boundary Conditions on Centerline:

$$p_{1,j} = p_{2,j}, \quad \rho_{1,j} = \rho_{2,j}, \quad (\rho E)_{1,j} = (\rho E)_{2,j},$$

$$(\rho u)_{2,j} = 0, \quad (\rho v)_{1,j} = (\rho v)_{2,j}$$

Boundary Conditions on the Wall of Gun:

$$p_{I,j} = p_{I-1,j}, \quad \rho_{I,j} = \rho_{I-1,j}, \quad (\rho E)_{I,j} = (\rho E)_{I-1,j},$$

$$(\rho u)_{I,j} = 0,$$

$(\rho v)_{I,j} = (\rho v)_w$ where $(\rho v)_w$ is defined such that the wall is moving at velocity - v .

Boundary Conditions 4 cm from the Projectile Base:

$p_{i,1} = p_b$ where p_b is taken from the BRL computer run.

$\rho_{i,1}, (\rho E)_{i,1}, (\rho u)_{i,1}, (\rho v)_{i,j}$ are all linearly extrapolated.

Boundary Conditions at the Projectile Base:

$$p_{i,J} = p_{i,J-1}, \quad \rho_{i,J} = \rho_{i,J-1}, \quad (\rho E)_{i,J} = (\rho E)_{i,J-1},$$

$$(\rho u)_{i,J} = -(\rho u)_{i,J-1}, \quad (\rho v)_{i,J} = 0$$

Boundary Conditions next to bullet for Gap:

$$\bar{p}_{b,j} = p_{b,j}, \quad \bar{\rho}_{b,j} = \rho_{b,j}, \quad (\rho E)_{\bar{b},j} = (\rho E)_{b,j},$$

$$(\rho u)_{\bar{b},j} = 0., \quad (\rho v)_{\bar{b},j} = -(\rho v)_{b,j}$$

Boundary Conditions for top of Gap:

$$p_{i,J} = p_{i,J-1}, \quad \rho_{i,J} = \rho_{i,J-1}, \quad (\rho E)_{i,J} = (\rho E)_{i,J-1},$$

$$(\rho u)_{i,J} = (\rho u)_{i,J-1}$$

TURBULENCE MODEL

The model I two-equation $k-\epsilon$ turbulence model as used by Pope and White-law⁽⁴⁾ was implemented in the code as follows:

$$\frac{\partial k}{\partial t} + u \frac{\partial k}{\partial r} + v \frac{\partial k}{\partial z} = \frac{1}{r} \frac{\partial}{\partial r} \left(r v \frac{\partial k}{\partial r} \right) + \frac{\partial}{\partial z} \left(v \frac{\partial k}{\partial z} \right) + P - \epsilon$$

$$\frac{\partial \epsilon}{\partial t} + u \frac{\partial \epsilon}{\partial r} + v \frac{\partial \epsilon}{\partial z} = \frac{1}{r} \frac{\partial}{\partial r} \left(r v \frac{\partial \epsilon}{\partial r} \right) + \frac{\partial}{\partial z} \left(v \frac{\partial \epsilon}{\partial z} \right) + \frac{\epsilon}{k} (c_{\epsilon 1} P - c_{\epsilon 2} \epsilon)$$

$$v = \min [c_{\mu} k^2 / \epsilon, v_{mol} + c_w v_* (r_w - r)]$$

$$P = v \left(\frac{\partial u}{\partial z} + \frac{\partial v}{\partial r} \right)^2 + \left(\frac{\partial u}{\partial r} \right)^2 + \left(\frac{\partial v}{\partial z} \right)^2 + \frac{u^2}{r}$$

$$c_{\mu} = 0.09$$

$$c_{\epsilon 1} = 1.45$$

$$c_{\epsilon 2} = 1.90$$

$$c_w = 0.04 \quad v_* = v_{i,j}$$

This model was used to run the problem under task F.3.1.5, which is the 40 mm gap problem. This model gave a viscosity, v , about 2 or 3 orders of magnitude larger than $v_{mol} + c_w v_* (r_w - r)$ where v_{mol} is the viscosity from Sutherland equation.

REFERENCES

1. Harlow, F. H. and A. A. Amsden, "A Numerical Fluid Dynamics Calculation Method for All Flow Speeds," Journal of Computational Physics, Academic Press, New York, Vol. 8, No. 2, Oct. 1971, pp. 197-213.
2. Stuhmiller, J. H. and M. J. Vander Vorst, "Construction of a Computer Program to Calculate the Dynamics of Fluids," for presentation at the ANS/ENS International Topical Meeting on "Advances in Mathematical Methods for Nuclear Engineering Problems," April 27-29, 1981, Munich, Federal Republic of Germany.
3. Vander Vorst, M. J., "DECBDD - Solves $A \cdot X = B$ where A is a Banded Matrix," an internal JAYCOR paper.
4. Pope, S. B. and J. H. Whitelaw, "The Calculation of Near-Wake Flows," Journal of Fluid Mechanics, Vol. 73, part 1, pp. 9-32 (1976).
5. Roache, P. J., Computational Fluid Dynamics, Hermosa Publishers, Albuquerque, New Mexico, 1976.

APPENDIX B
DISCUSSION OF ADDITIONAL CALCULATIONS

Below is a summary of the calculations called out in the contract (underlined) and additional calculations performed by JAYCOR to clarify the behavior. These runs were made with no net bypass flow, which was later decided not to be the preferred boundary conditions thereby necessitating the runs described in the main body of the text.

F.3.1.1. No gap problem with 20 mm gun. The computational grid spacing used was the same as used by the BRL computer run dated 20 December 1979 in the radial direction, and a fixed increment of 0.002 in axial direction.

F.3.1.2. No gap problem with 40 mm gun. Two (2) runs were made for this task as follows:

F.3.1.2.A. No gap problem with 40 mm gun and projectile weight of 480 grams. This weight was used because it scales with the 20 mm gun with weight of 120 grams. This was done so comparisons could be made to the BRL computer run dated 20 December 1979. The computational grid spacing used was the same as in F.3.1.1.

F.3.1.2.B. No gap problem with 40 mm gun and projectile weight of 960 grams. The computational grid spacing used was the same as in F.3.1.1.

F.3.1.3. No gap problem with 40 mm gun and turbulence model. The projectile weight used was 480 grams so again comparisons could be made to the BRL computer run. This was run with a fixed viscosity of 10^{-4} [about two (2) orders of magnitude larger than from Sutherland equation]. The computational grid spacing used was the same as in F.3.1.1.

F.3.1.4. Gap problem with 40 mm gun. The computational grid spacing was the same as the BRL computer run in the radial direction, and using an increment of 0.002 meters up to three (3) cells above the gap and then an increment of 0.02 meters to the top of the gap. Three (3) runs were made for this task as follows:

F.3.1.4.A. Gap problem with 20 mm gun. This run used as the boundary condition for (ρv) at the top of the gap to vary linearly from the projectile ($v = 0$) to the gun wall ($v = -V$) as discussed in the boundary condition

section. Note that this run hit time limit at $t = 0.0019305$ and on the graphs this time is plotted with the BRL computer run at $t = 0.0022917$.

F.3.1.4.B. Gap problem with 40 mm gun and projectile weight of 480 grams. The weight was changed so to scale with the BRL computer run. This run used as the boundary condition for (ρv) at the top of the gap to correspond to the velocity of the projectile.

F.3.1.4.C. Gap problem with 40 mm gun and projectile weight of 960 grams. This run used the same boundary conditions for (ρv) as F.3.1.4.B.

F.3.1.5. Gap problem with 40 mm gun and turbulence model. The computational grid spacing used was the same as in F.3.1.4. Three (3) runs were made for this task as follows:

F.3.1.5.A. Gap problem with 40 mm gun with the two-equation $k-\epsilon$ turbulence model as used by Pope and Whitelaw and projectile weight of 480 grams.

F.3.1.5.B. Gap problem with 40 mm gun with a fixed viscosity of 10^{-3} (about 3 orders of magnitude larger than from Sutherland equation) and projectile weight of 480 grams.

F.3.1.5.C. Gap problem with 40 mm gun with a fixed viscosity of 10^{-4} (about 2 orders of magnitude larger than from Sutherland equation) and projectile weight of 480 grams.

F.3.1.6. Gap problem with 40 mm gun, turbulence model and mesh refinement. Two (2) runs were made for this task as follows:

F.3.1.6.A. Gap problem with 40 mm gun, fixed viscosity of 10^{-4} , projectile weight of 480 grams, one grid halving in both the radial and axial direction. This run required one (1) hour of CP time on the CDC 7600 computer.

F.3.1.6.B. Gap problem with 40 mm gun, fixed viscosity of 10^{-4} , projectile weight of 480 grams, two (2) grid halvings in the axial direction because of the CP time that would have been required.

Of the twelve runs described above, some are of greater interest in the light of the net bypass flow cases run later. A discussion of the comparison is given below in order to shed light on the difference caused by changing the

outflow boundary conditions and to document the experience gained with a two-variable turbulence model and with varying the radial resolution.

The initial calculations were made with zero net bypass flow around the shell. Figures B-1 through B-5 show the whole field visualization of the flow evolution in this case which is typical of the variation seen in all cases with no net bypass. The early moments show the expansion region pulling gas in from the gap. Recall that there is considerable distortion of the cells and velocity vectors in this representation and that only the pattern is qualitatively correct. A recirculation develops but cannot be maintained although reinforced by the flow reversal caused by the rarefaction waves; this is qualitatively the same as in the net bypass cases, Figures 50-54. The final flow patterns, Figure B-5, are similar to the bypass case in the chamber but the gap shows only downward flow in the shell's frame of reference. The pressure history, Figure B-6, is the same as before, but the temperature field, Figures B-7 and B-8, is considerably cooler than with bypass due to the much smaller velocity gradients in the gap. The remaining runs were concentrated on the 40 mm diameter barrel.

Figures B-9 through B-13 present results on the 40 mm, no gap case where the shell's mass has been scaled with the square of its base area to produce the same acceleration as in the 20 mm case. The results for flow pattern, pressure, and temperature are essentially the same as in the 20 mm case.

Figures B-14 through B-18 show the flow pattern in the no gap case when the fluid viscosity is increased to 10^{-4} cm²/sec, about two orders of magnitude larger than the value given by the Sutherland equation. The variations of pressure and temperature are nearly identical to the lower viscosity runs. The high viscosity values were explored as a substitute for a turbulence model after problems developed with standard models.

Figures B-19 through B-26 show the results for the 40 mm diameter barrel with a 10% gap and no net bypass flow. The same sequence of patterns that occurred in the 20 mm case reappears: initial expansion and circulation in the wake of the shell dissipation and migration of the eddy; reestablishment of the circulation pattern due to a rarefaction wave; and the final, expansion flow out the bottom boundary. One significant difference is that the wider gap permits a boundary layer to develop on the shell which leads to countercurrent

flow in the gap, Figure B-22. Some flow splitting at the shell corner does occur, but it is not the dominant feature as in the net bypass flow situations. The pressure variation is identical to the 20 mm case because the prescribed boundary conditions dominate the field, but the wall temperatures are slightly lower because the scale of the chamber has been increased. Internal, thermal eddys originating from the corner flow can be seen in the temperature contours, Figure B-26.

When the turbulence model of Pope and Whitelaw was used the calculations invariably diverged after the shell reached sizeable speeds. The problem stemmed from a catastrophic production of turbulence energy in the neighborhood of the corner. This, in turn, arose from the high shear field produced at the separation point and the strong rarefaction effects of the accelerating shell. The model, based on incompressible and parallel flow data, is evidently not applicable in this circumstance. It is unlikely that there is a viable theory for this flow, however coupled with the short duration of this problem fully developed turbulence probably does not occur. In any event, to study the effects of "turbulence-like" diffusion, we overwrote the calculated turbulence quantities, in particular the eddy viscosity, whenever they exceeded the values encountered in pipe flow at the same mean velocity, pipe diameter, and distance from the wall. This modification did allow the code to run and the results are shown in Figure B-27 through B-34. The flow fields are qualitatively similar, although the boundary layer is thicker and countercurrent flow in the gap has greater difficulty forming. The pressure history is again the same, but the corner temperature is higher by about 150°C due to accentuated wall friction.

An even greater viscosity of 10^{-3} cm²/sec was chosen for the calculation presented in Figures B-35 through B-42. Again, the flow pattern and pressure is essentially the same but wall heating has raised the temperature 400°C above the normal laminar case. This variation in viscosity over almost three orders of magnitude is fairly convincing evidence that the flow pattern will exist independent of the exact form of the diffusion.

On the other hand, there is a marked difference in the corner flow with and without net bypass flow. With bypass there is a strong flow splitting at the corner in the 20 mm case that is not seen when the gas moves with the shell. The 40 mm barrel with gap does show the effect.

Finally, calculations were made with 20, 40, and 80 cells in the radial direction. The results shown in whole field visualization are found in Figures B-43 through B-71. The calculations agree very closely over the whole range and at all times, indicating that the lower resolution runs are sufficiently accurate for the present purposes. The largest difference was a 20°C change in wall temperature between the 20×20 and the 20×80 runs.

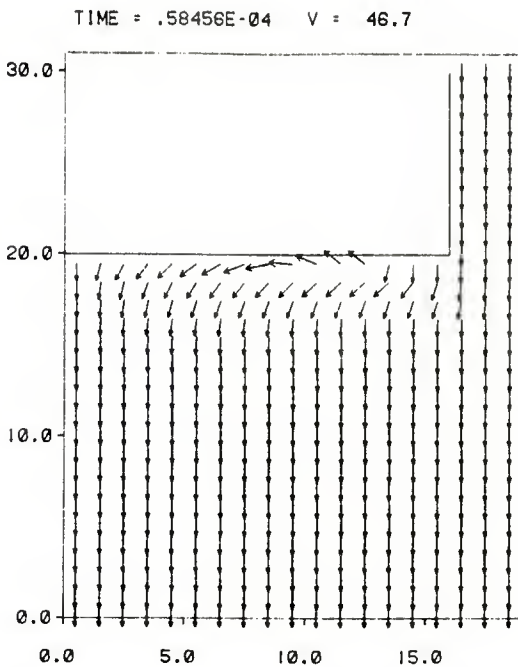


Figure B-1. Whole field visualization of 20 mm, 1% gap when no net flow boundary conditions are used at the exit of the gap. All vectors have been expanded to fill their computational cell and all cells have been expanded to a square array. Considerable geometric distortion is introduced but the flow directions are clearly seen. At this early time a rarefaction has developed behind the shell which is pulling in gas from the gap. The flow pattern is similar to that of Figure 50 where net flow past the shell was imposed.

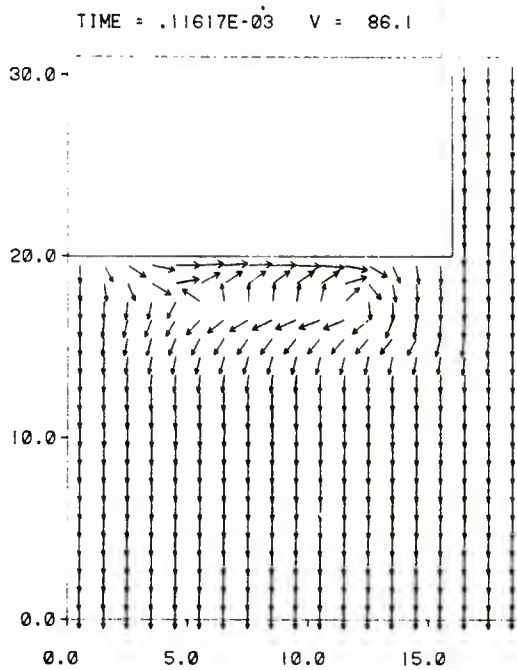


Figure B-2. See caption for Figure B-1. Flow separation eddy has grown in the shell's wake and is still qualitatively similar to the net flow calculation shown in Figure 51.

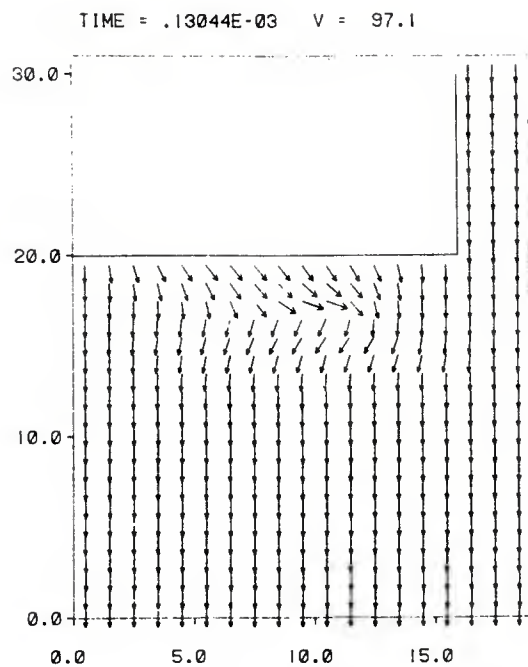


Figure B-3. See caption for Figure B-1. The recirculation region has been dispersed for the moment as a local rarefaction develops in its place. By this time in the net flow calculation, flow up the gap has developed. See Figure 52.

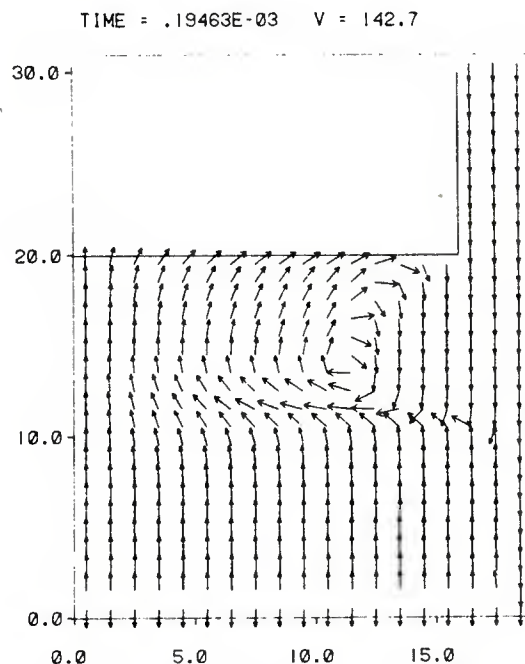


Figure B-4. See caption for Figure B-1. The recirculation has been reestablished at the corner of the shell aided by the flow reversal of the rarefaction wave that can be seen just leaving the region at the bottom of the mesh. This situation is very nearly the same as that shown in Figure 53 for the net bypass flow case. The recirculation eddy is stronger here because the gap flow is downward.

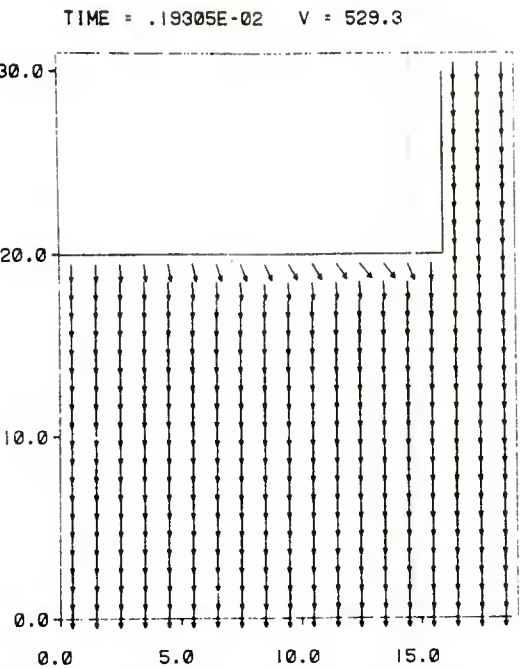
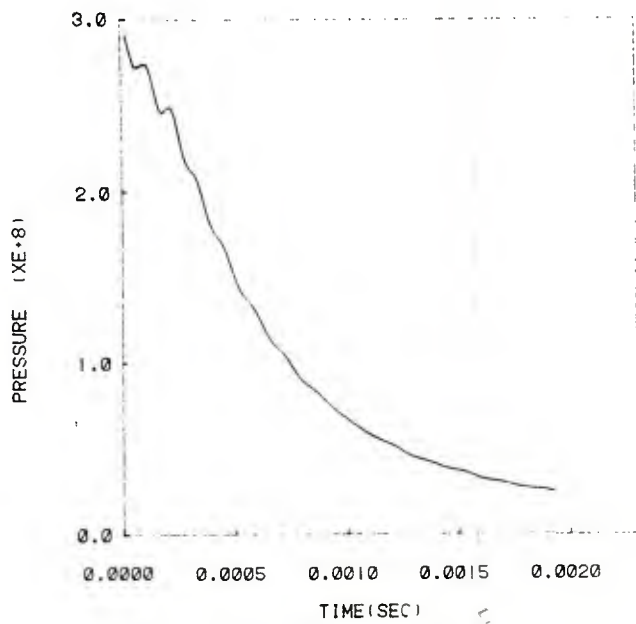
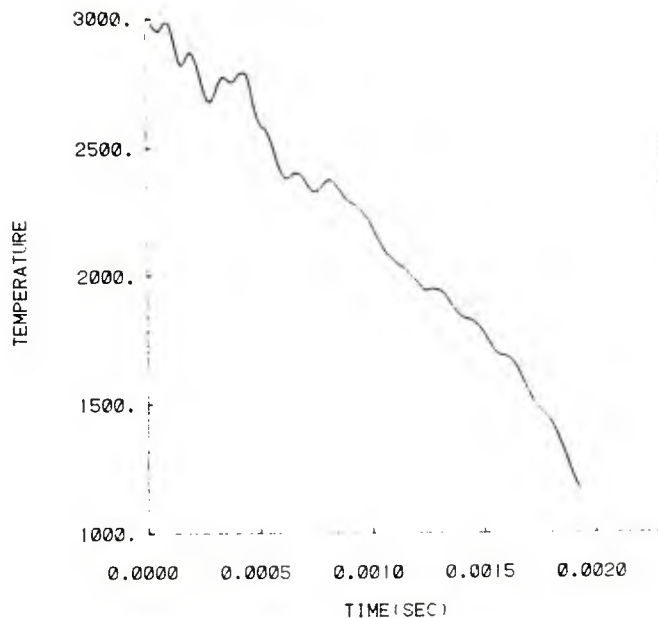


Figure B-5. See caption for Figure B-1. Final flow pattern is a simple flow away from the shell and downward from the gap. There is no flow from the end of the gap in this frame of reference but the scaling of vector lengths accentuates the small gap flow. The flow pattern in the chamber is very similar to that in the net flow case, but the gap direction is reversed.

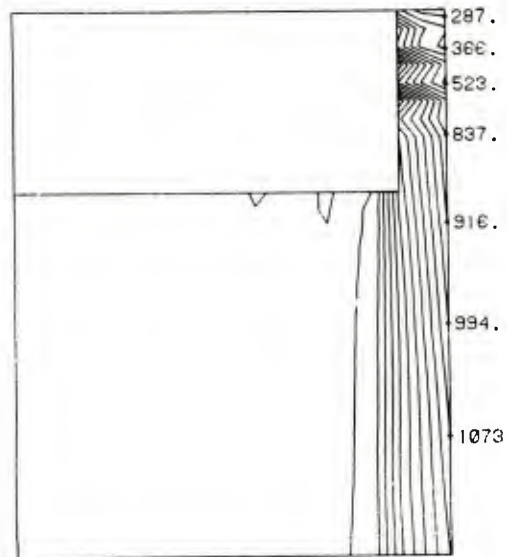


TIME HISTORY AT CORNER OF PROJECTILE
Figure B-6. Time history of pressure at the shell corner for 20 mm diameter barrel with a 1% gap and no net bypass flow. The results are very similar to the net bypass flow case, see Figure 33, because the pressure level is largely set by the prescribed values on the open boundary.



TIME HISTORY AT CORNER OF PROJECTILE

Figure B-7. Time history of temperature at the shell corner for a 20 mm diameter barrel with a 1% gap and no net bypass flow. The early time behavior is similar to the net bypass flow case, see Figure 34, but after about 0.7 ms this case produces much lower temperatures. This is caused by the cool, expanded gas leaving the gap and mixing with the wall boundary layer.



TEMPERATURE CONTOURS AT TIME = .18496E-02

Figure B-8. Temperature contours in the whole field visualization for a 20 mm diameter barrel with 1% gap and no net bypass flow. The temperatures are considerably less than in the bypass case, see Figure 35, because there is much less viscous heating in the gap.

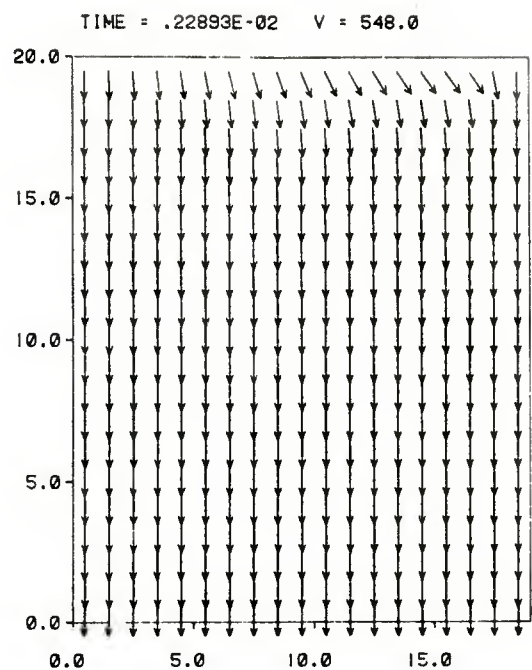


Figure B-9. Whole field visualization of flow pattern in 40 mm barrel with no gap. See Figure B-1 for description of distortion introduced. At late times flow is similar to 20 mm case; see Figure 4-9. Early times showed the previously observed rarefaction motion and flow reversal.

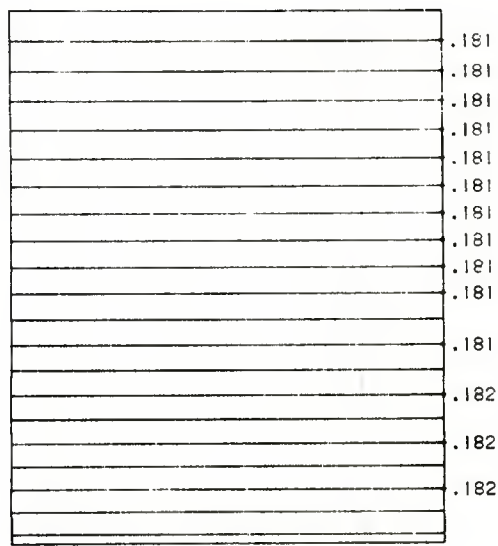
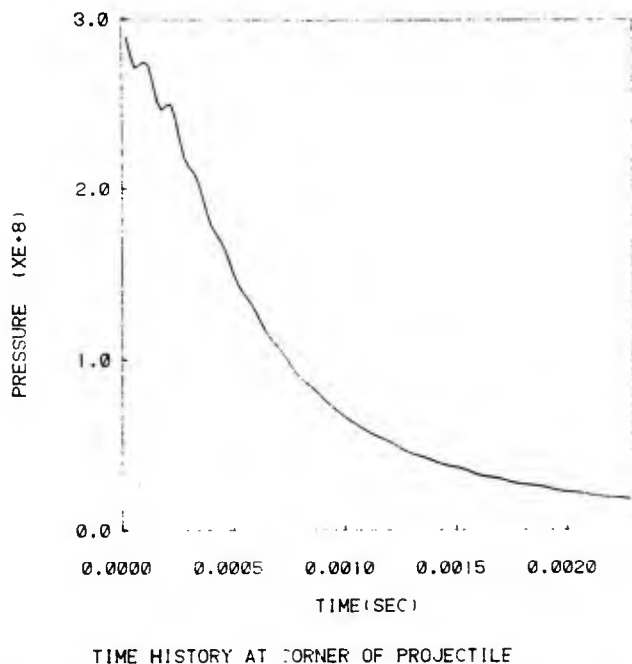
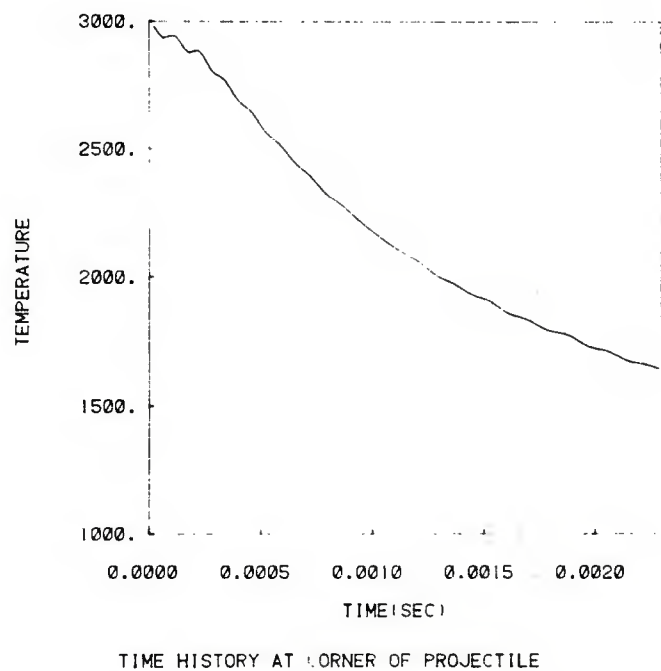


Figure B-10. See caption for Figure B-9. Pressure contours at late time are horizontal and nearly constant.



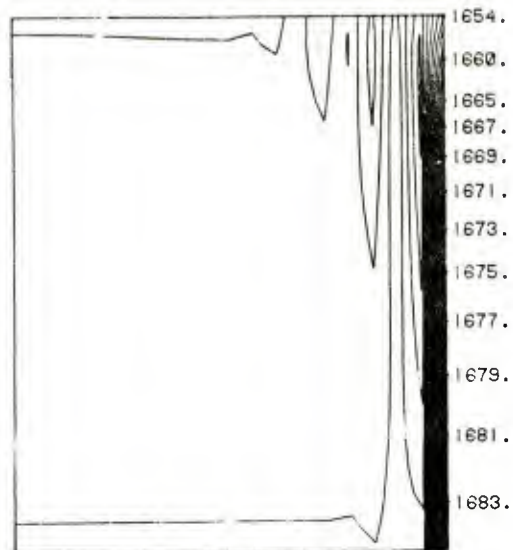
TIME HISTORY AT CORNER OF PROJECTILE

Figure B-11. Time history of pressure at shell corner for 40 mm diameter barrel with no gap. Nearly identical to 20 mm case, see Figure 10, with characteristic early oscillations due to rarefaction propagation.



TIME HISTORY AT CORNER OF PROJECTILE

Figure B-12. Time history of temperature at the shell corner for 40 mm diameter barrel with no gap. Results are nearly identical with 20 mm case. See Figure 14. Shell mass was scaled to produce the same accelerations.



TEMPERATURE CONTOURS AT TIME = .22893E-02

Figure B-13. Whole field visualization of temperature contours for 40 mm, no gap case. Strong wall boundary layer heating is similar to 20 mm case shown for corner region only in Figure 13.

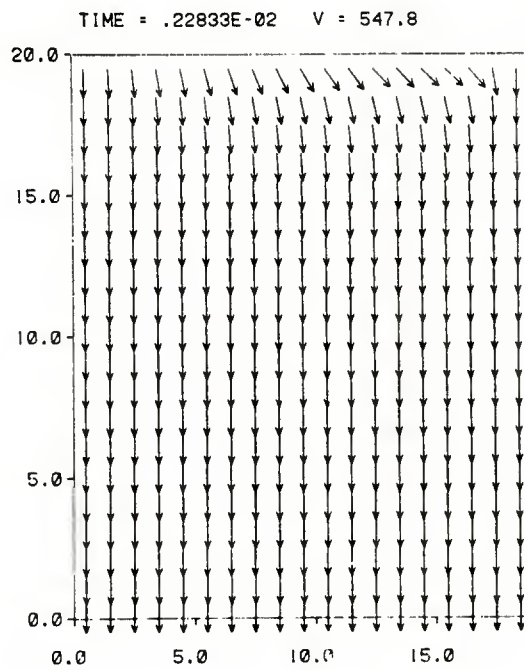
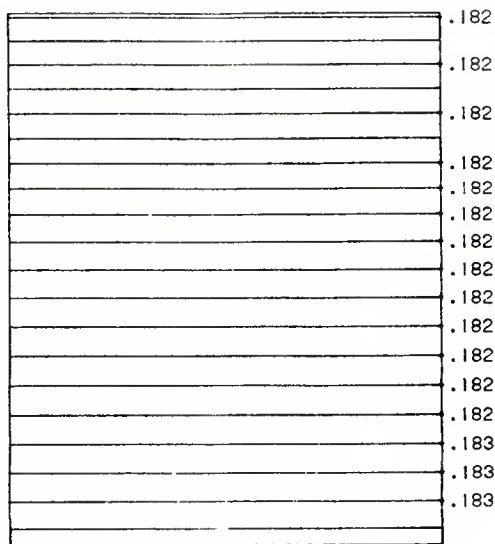
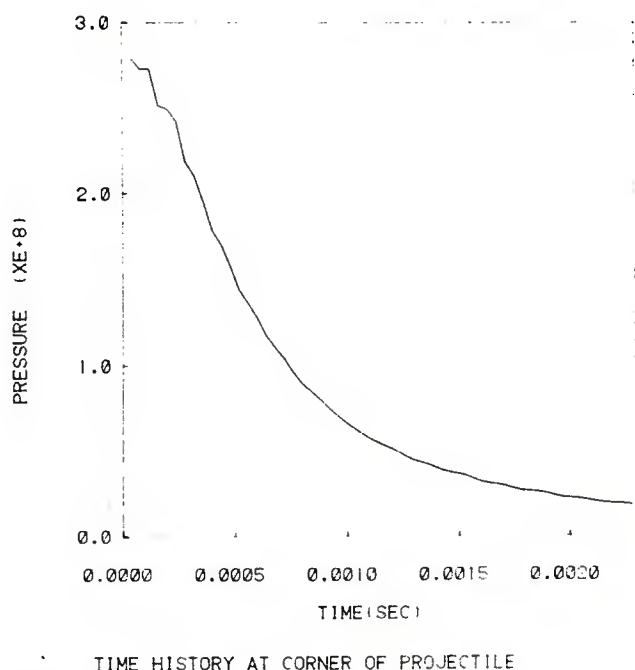


Figure B-14. Whole field visualization for 40 mm diameter barrel with no gap when the gas kinematic viscosity is assumed to be $10^{-4} \text{ cm}^2/\text{sec}$. See Figure B-1 for distortions caused by this plot. Viscosity is about an order of magnitude greater than standard case but flow pattern is unchanged.



PRESSURE CONTOURS AT TIME = .22833E-02

Figure B-15. See caption for Figure B-14. Pressure contours at late time showing the horizontal and nearly constant values characteristic of all of the no gap runs.



TIME HISTORY AT CORNER OF PROJECTILE

Figure B-16. Time history of the pressure at the corner of the shell for the 40 mm barrel, no gap case with viscosity equal to $10^{-4} \text{ cm}^2/\text{sec}$. Behavior is similar to other no gap cases except that rarefaction oscillations seem to be damped.

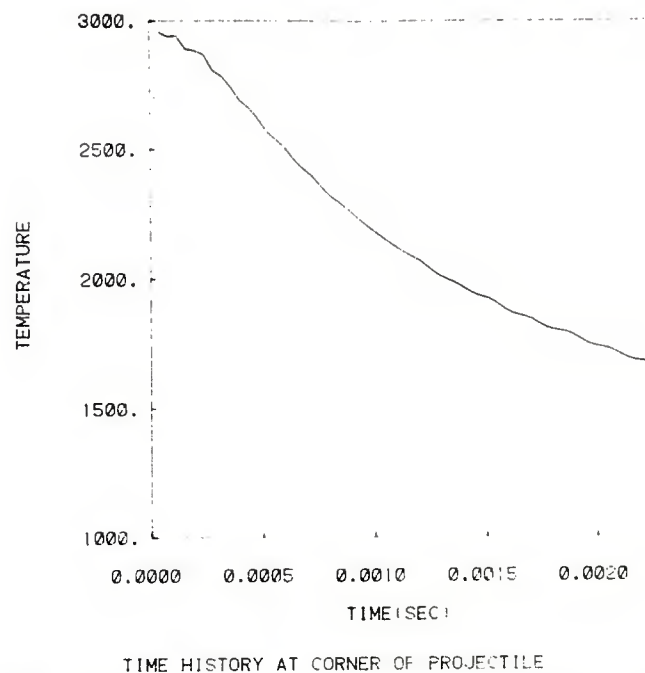
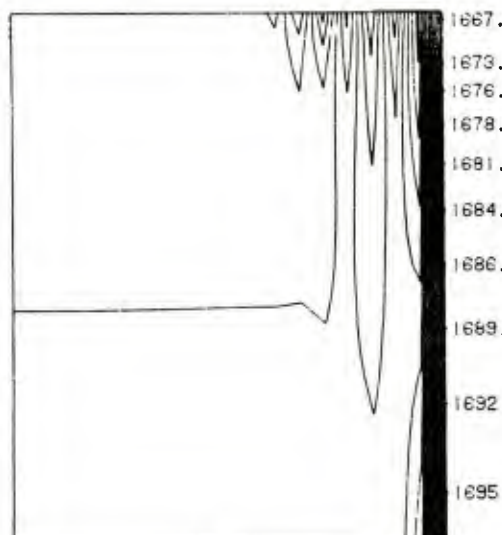


Figure B-17. Time history of temperature at the shell corner for the 40 mm, no gap case with viscosity raised to 10^{-4} cm 2 /sec. Behavior is similar to other no gap cases.



TEMPERATURE CONTOURS AT TIME = .22833E-02

Figure B-18. Whole field visualization of temperature contours at late time for 40 mm, no gap case with viscosity raised to 10^{-4} cm 2 /sec. Variation is similar to that seen in other no gap cases.

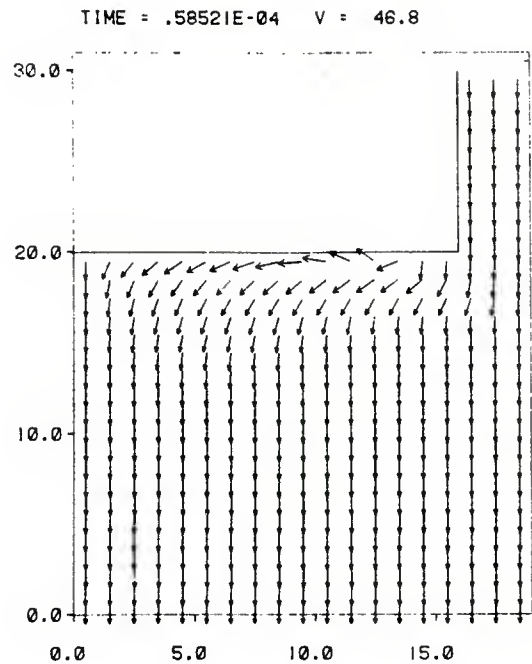


Figure B-19. Whole field visualization of flow pattern for 40 mm diameter barrel with a 1% gap when no net outflow is permitted. At early times a rarefaction region develops behind accelerating shell and gas is pulled in from gap. Similar to 20 mm case; Figure B-1.

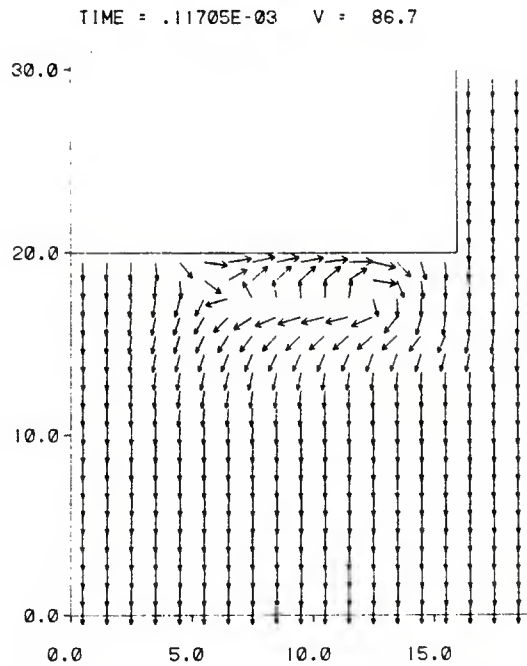


Figure B-20. See caption for Figure B-19. Recirculation region has developed in shell's wake. Eddy occupies a smaller fraction of the shell's base than in the 20 mm case; see Figure B-2. Absolute eddy size may be nearly constant.

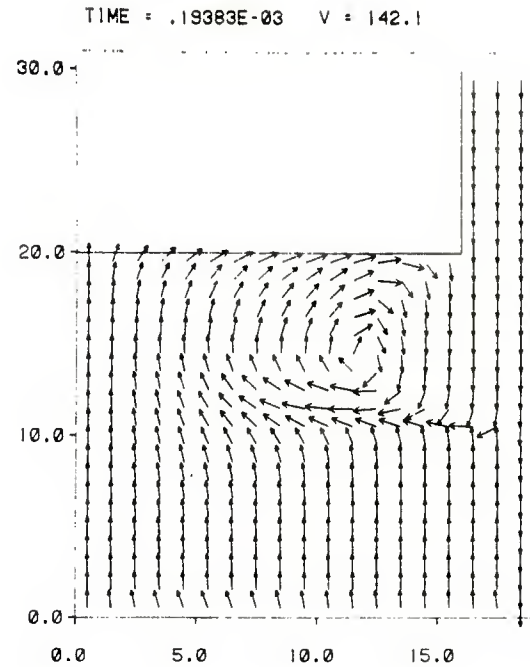


Figure B-21. See caption for Figure B-19. Recirculation associated with rarefaction wave is very similar to the 20 mm case shown in Figure B-4.

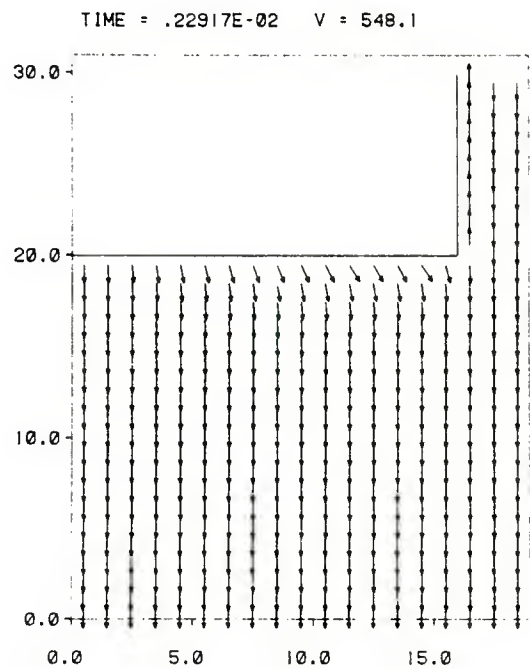
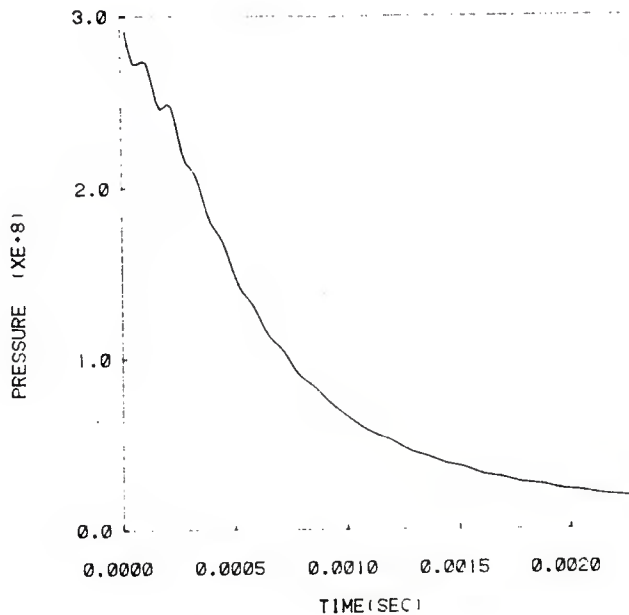
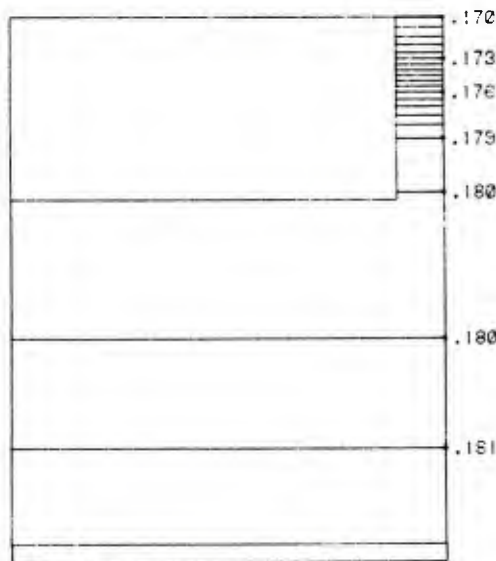


Figure B-22. See caption for Figure B-19. Final flow pattern is similar to 20 mm case in the chamber, see Figure B-5, but differs in the gap. The wall boundary layer is unable to span the gap so countercurrent flow has developed reminiscent of the net outflow cases. There is flow splitting at the corner in this case.



TIME HISTORY AT CORNER OF PROJECTILE

Figure B-23. Time history of pressure at the corner of the shell for a 40 mm diameter barrel with a 1% gap. Behavior similar to 20 mm case with and without net bypass flow.



PRESSURE CONTOURS AT TIME = .22917E-02

Figure B-24. See caption for Figure B-19. Pressure contours at late time. Pressure in chamber exceeds that in the gap in order to accelerate flow with the shell and against the wall boundary layer.

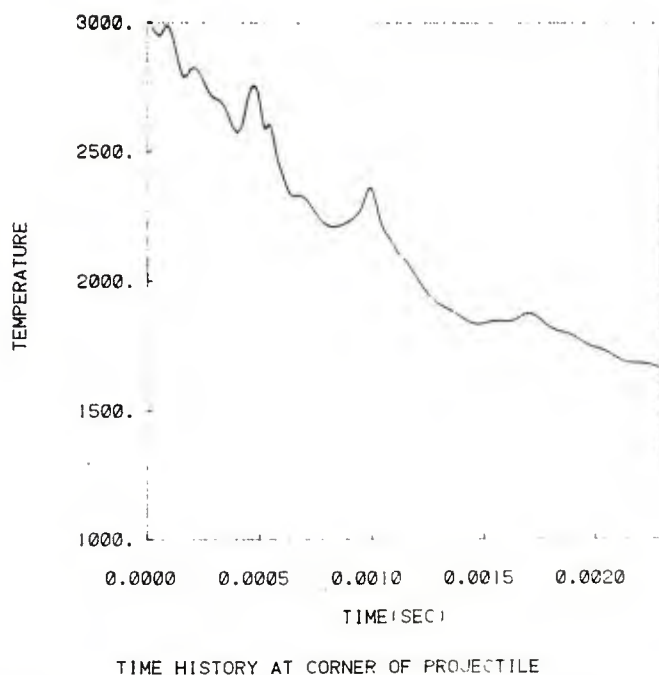


Figure B-25. Time history of the gas temperature at the corner of the shell for a 40 mm diameter barrel with a 1% gap. Large oscillations are due to vortex shedding at the corner and the countercurrent flow into the gap which did not existd in the 20 mm case.

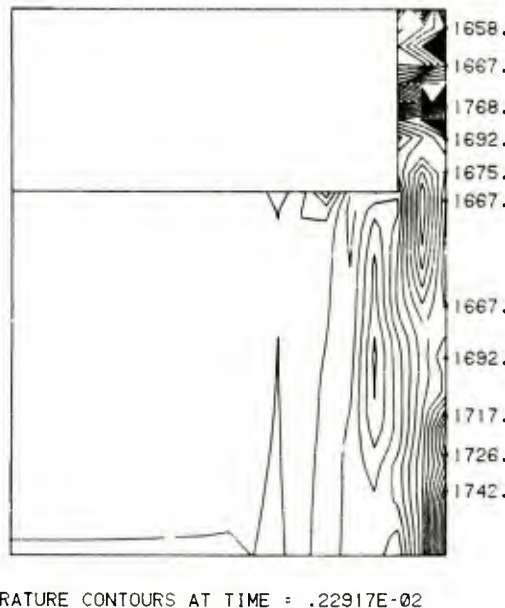


Figure B-26. See caption for Figure B-19. Temperature contours at late time show values comparable to the 20 mm case with net flow bypass, Figure 35, and much higher than the 20 mm no bypass case, Figure B-8. This is due to the countercurrent gap flow which brings gas into the gap region.

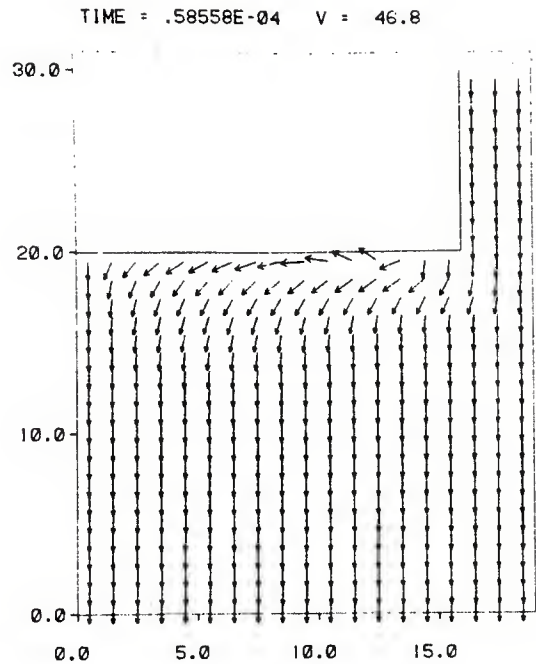


Figure B-27. Whole field visualization of the flow pattern for a 40 mm diameter barrel with a 1% gap using the turbulence model of Pope and Whitelaw. To obtain calculations that were stable the turbulent variables had to be overwritten whenever they exceeded boundary layer values. At early times the flow is similar to the standard case; Figure B-19.

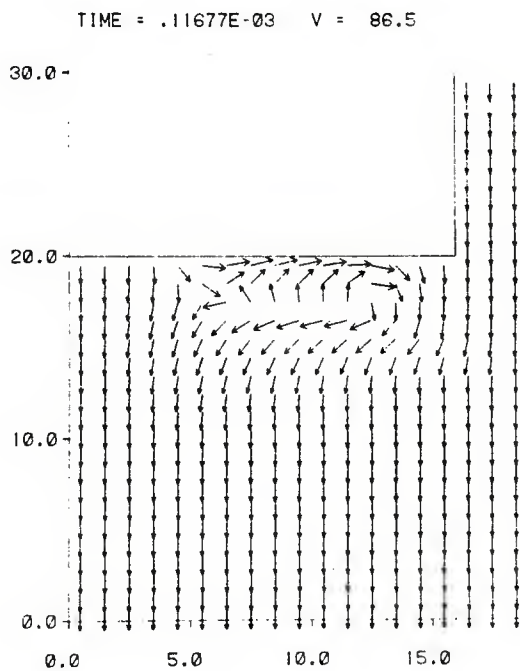


Figure B-28. See caption for Figure B-27. Recirculation eddy in shell's wake is similar to the laminar result in Figure B-20.

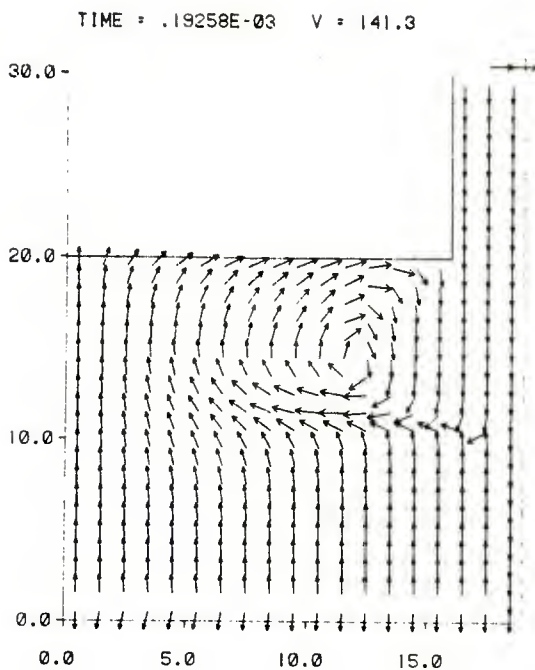


Figure B-29. See caption for Figure B-27. Reestablishment of recirculation caused by flow reversal of a rarefaction wave just passing out of the system. Compare to Figure B-21.

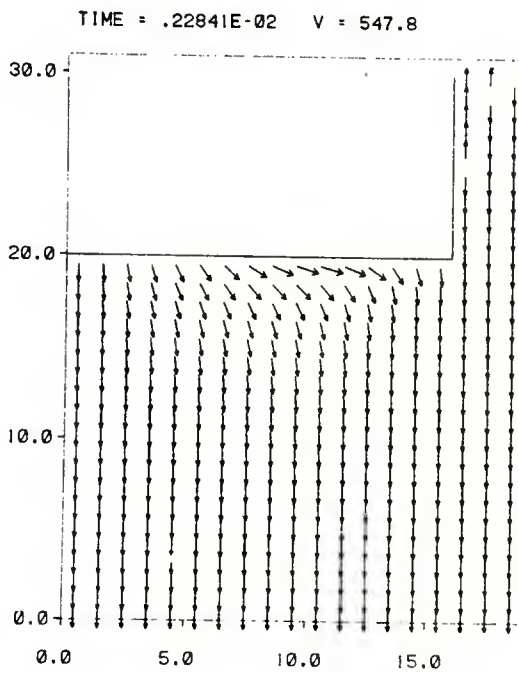
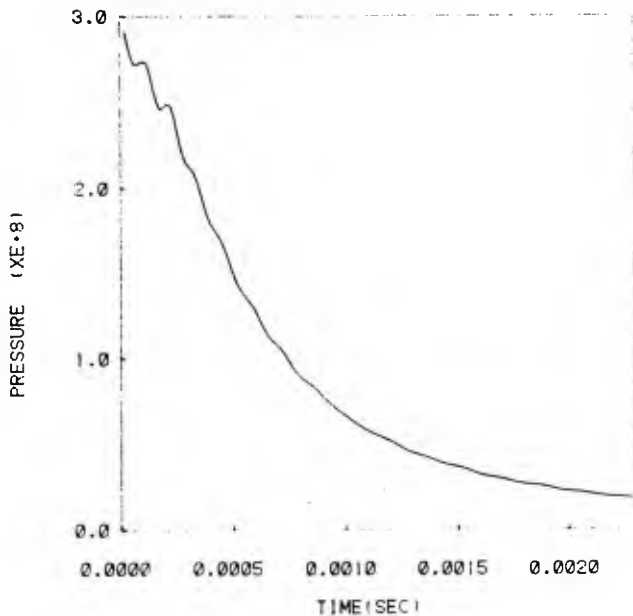
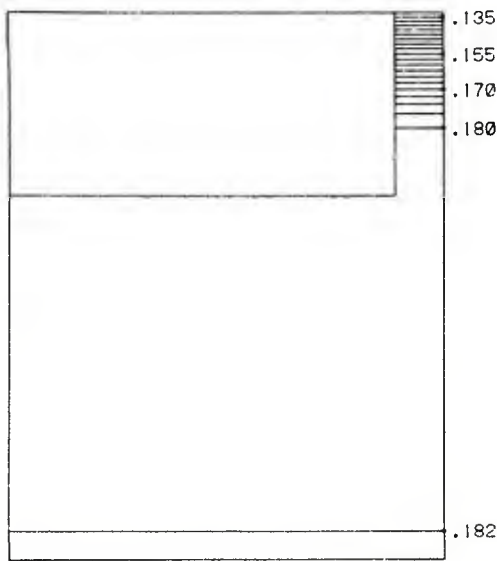


Figure B-30. See caption for Figure B-27. Boundary layer along wall much stronger at the high effective viscosity so that the lower gap region is pulled downward and the cross flow along the shell bottom is deflected more strongly.



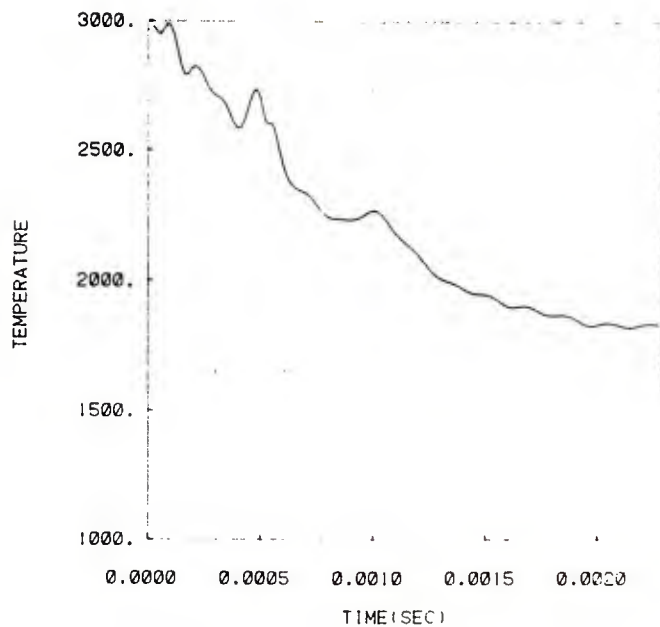
TIME HISTORY AT CORNER OF PROJECTILE

Figure B-31. Time history of pressure at the corner of the shell for a 40 mm diameter barrel with a 1% gap using the Pope and Whitelaw turbulence model. Results essentially the same as the laminar case; see Figure B-23.



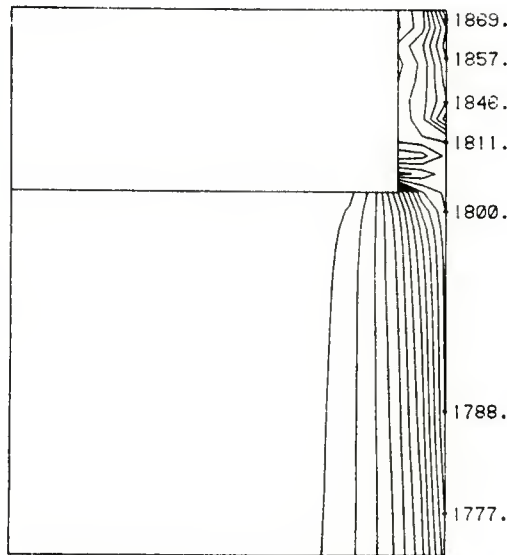
PRESSURE CONTOURS AT TIME = .22841E-02

Figure B-32. See caption for Figure B-27. Pressure contours for whole field showing that gap pressure is less than laminar case, Figure B-24, in order to drive gas into the gap against the greater viscous forces.



TIME HISTORY AT CORNER OF PROJECTILE

Figure B-33. Time history of gas temperature at the corner of the shell for a 40 mm diameter barrel with a 1% gap using the Pope and Whitelaw turbulence model. The results are similar to the laminar case, Figure B-25, although the final temperatures are higher due to enhanced viscous heating.



TEMPERATURE CONTOURS AT TIME = .22841E-02

Figure B-34. See caption for Figure B-27. Whole field visualization of temperature contours. Values are about 150°C higher than in laminar case, Figure B-26, because of enhanced viscous heating.

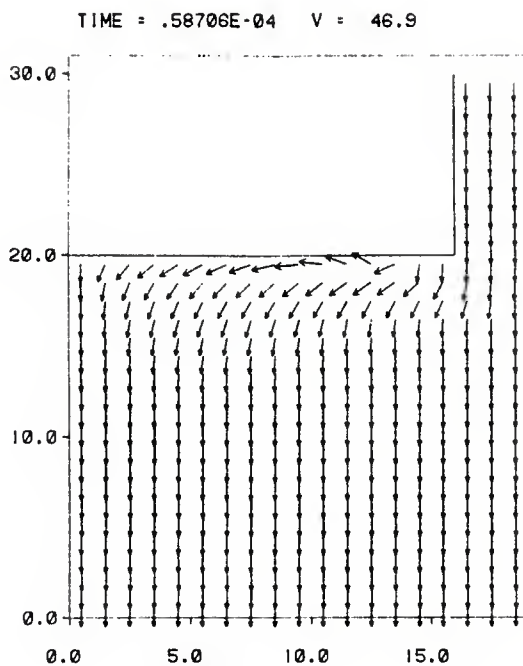


Figure B-35. Whole field visualization of flow pattern in 40 mm barrel with a 1% gap when the viscosity has been raised to a uniform value of 10^{-3} cm^2/sec . See caption on Figure B-1 for distortion caused by this kind of plot. Early time expansion at rear of shell pulls in gasses from the gap.

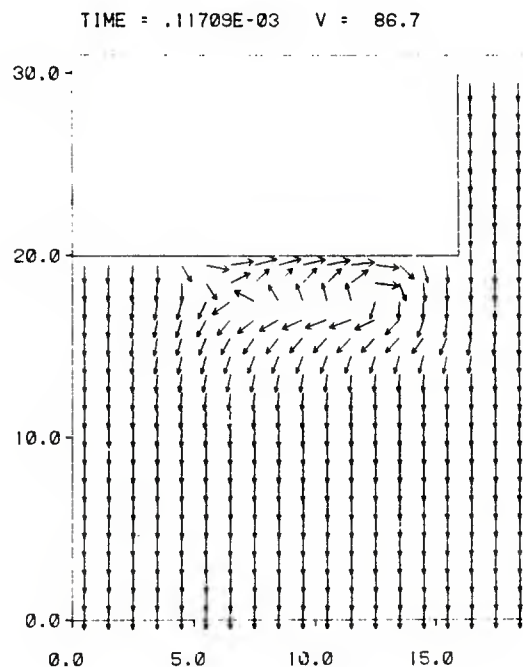


Figure B-36. See caption for Figure B-35. Recirculation eddy at rear of shell is qualitatively the same as those in other gap cases.

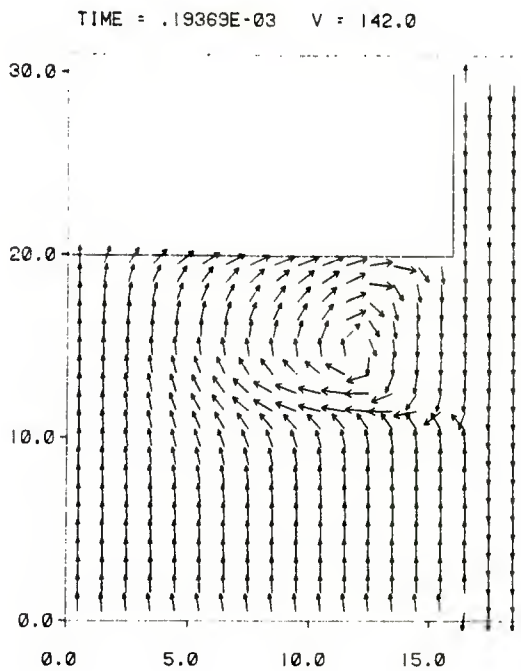


Figure B-37. See caption for Figure B-35. Reestablished circulation pattern following rarefaction wave. Wall boundary layer is considerably wider than in less viscous cases.

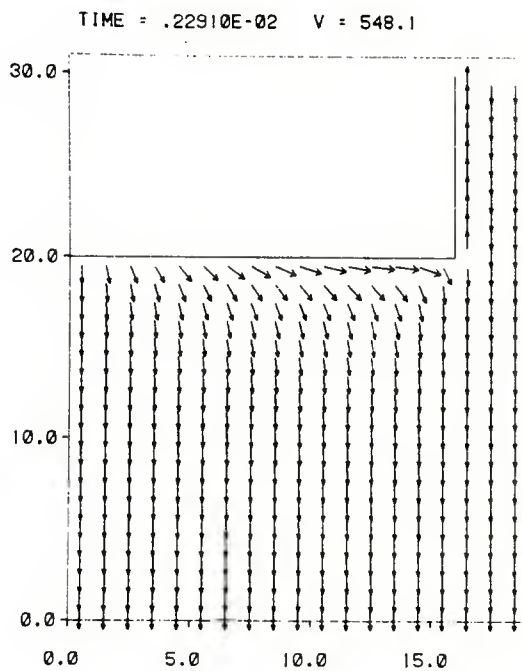
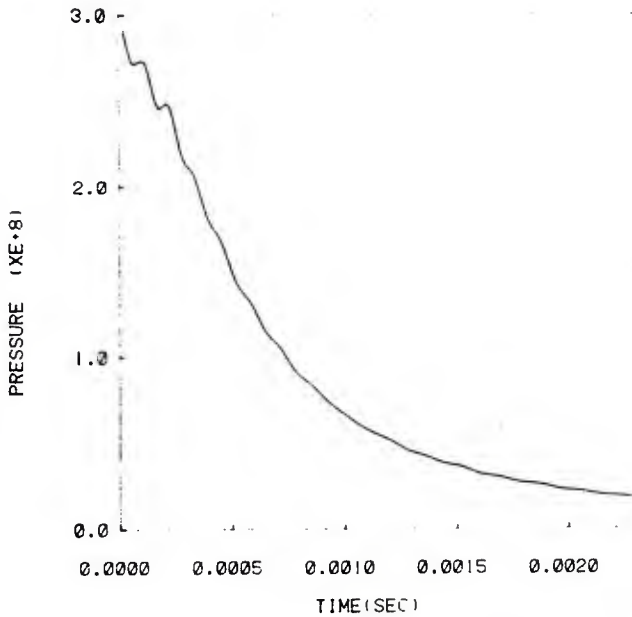
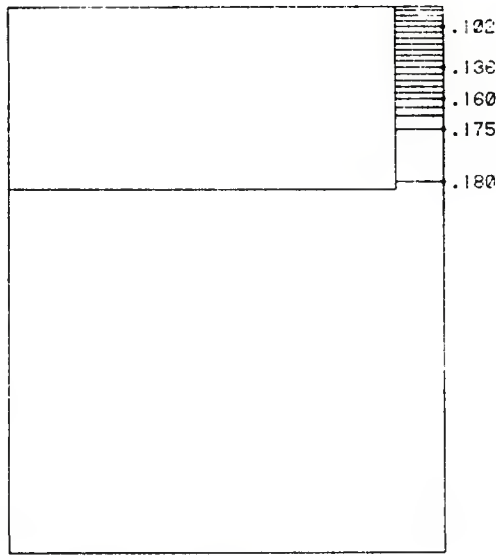


Figure B-38. See caption for Figure B-35. Final flow pattern is similar to other no gap cases in the chamber. In the gap, the larger viscosity has strengthened the wall boundary layer so much that upflow again appears along the shell.



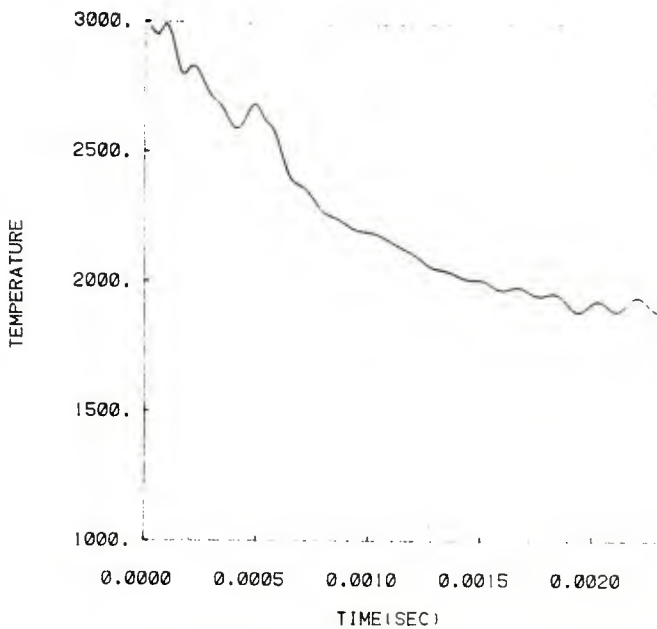
TIME HISTORY AT CORNER OF PROJECTILE

Figure B-39. Time history of pressure at corner of shell for 40 mm diameter barrel with a 1% gap when the viscosity has been raised to 10^{-3} cm²/sec. The behavior is similar to other gap cases.



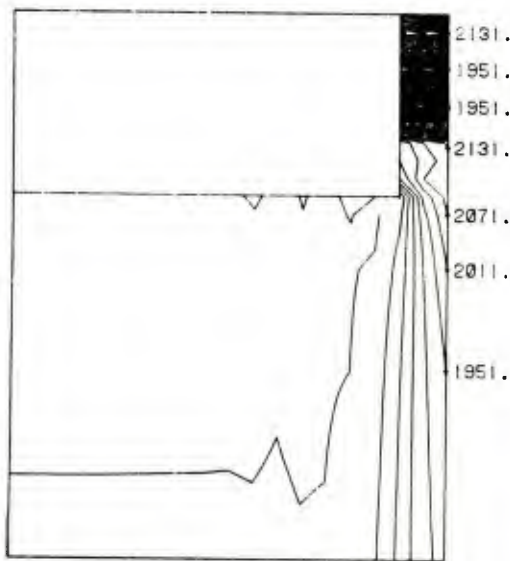
PRESSURE CONTOURS AT TIME = .22910E-02

Figure B-40. See caption for Figure B-35. Whole field visualization of pressure contours showing the lowest of all pressures in the gap. These low pressures develop in order to drive the gas into the gap.



TIME HISTORY AT CORNER OF PROJECTILE

Figure B-41. Time history of the gas temperature at the corner of the shell for a 40 mm diameter barrel with a 1% gap when the viscosity is raised to 10^{-3} cm²/sec. The results are similar to other gap cases but temperatures are generally higher due to enhanced viscous heating. Irregularities due to flow unsteadiness are now more evident.



TEMPEARTURE CONTOURS AT TIME = .22910E-02

Figure B-42. See caption for Figure B-35. Whole field temperature contours reveal that viscous heating has raised temperatures 400°C above the laminar case.

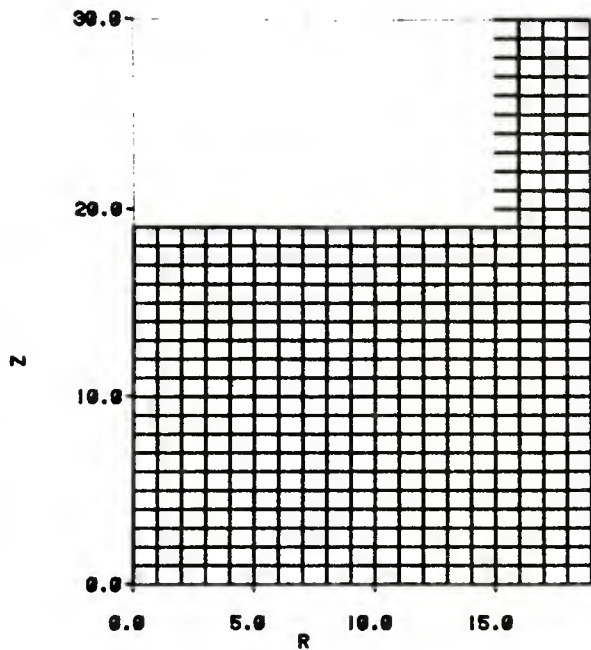


Figure B-43. Expanded computational grid for calculation at standard resolution (20×20 in chamber). Cells have been shown as square; correct aspect ratio is shown in Figure 15.

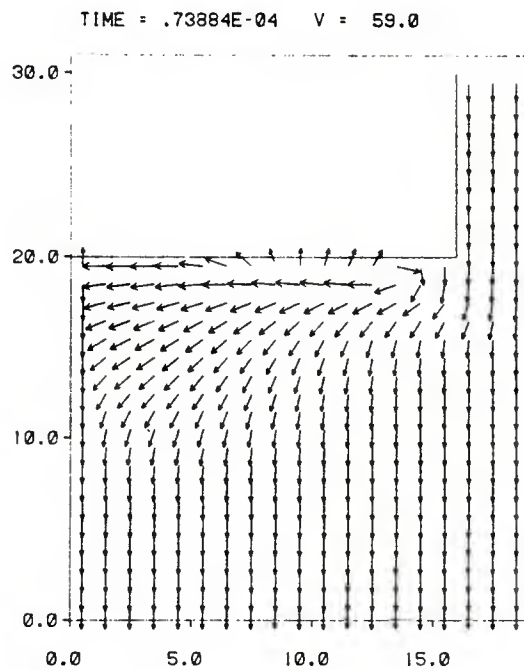


Figure B-44. Whole field visualization of flow pattern for a 40 mm diameter barrel with a 1% gap and a viscosity of 10^{-4} cm 2 /sec. These parameters are the standard case for the mesh refinement calculations. Initial flow separation at t = 0.074 ms.

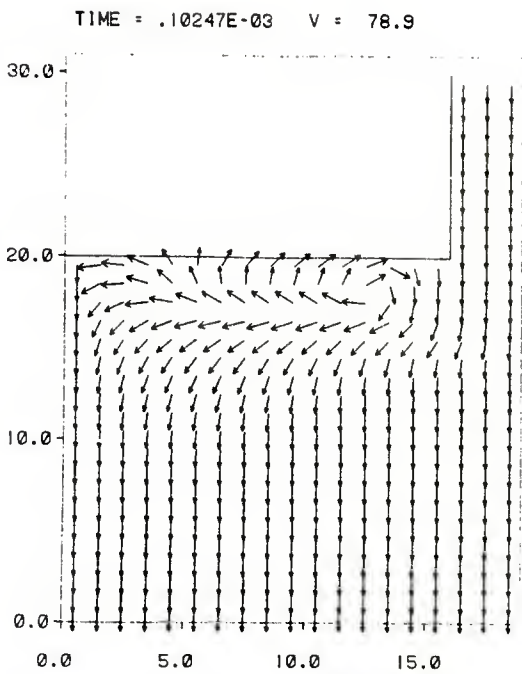


Figure B-45. See caption for Figure B-44. Development of recirculation zone, $t = 0.10$ ms.

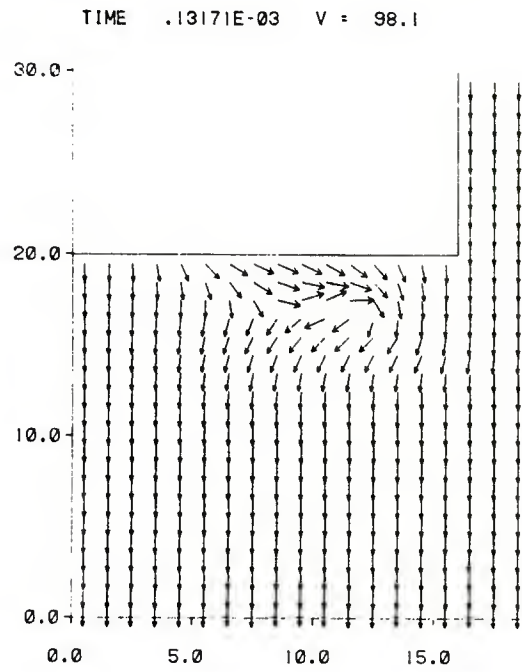


Figure B-46. See caption for Figure B-44. Migration of eddy; $t = 0.13$ ms.

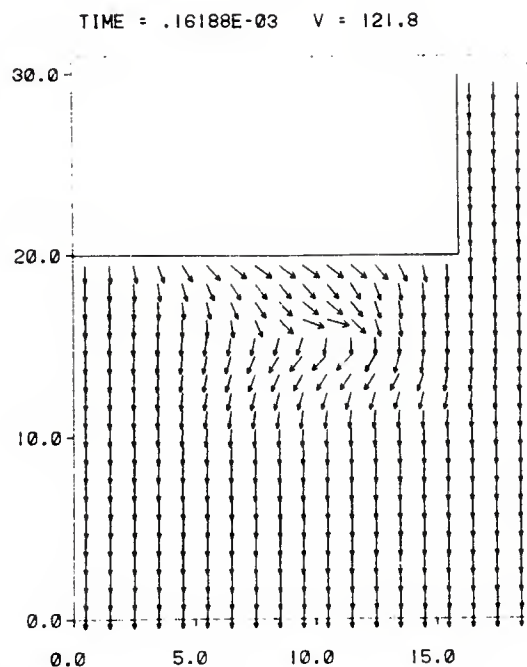


Figure B-47. See caption for Figure B-44. Diffusion of eddy; $t = 0.16 \text{ ms}$.

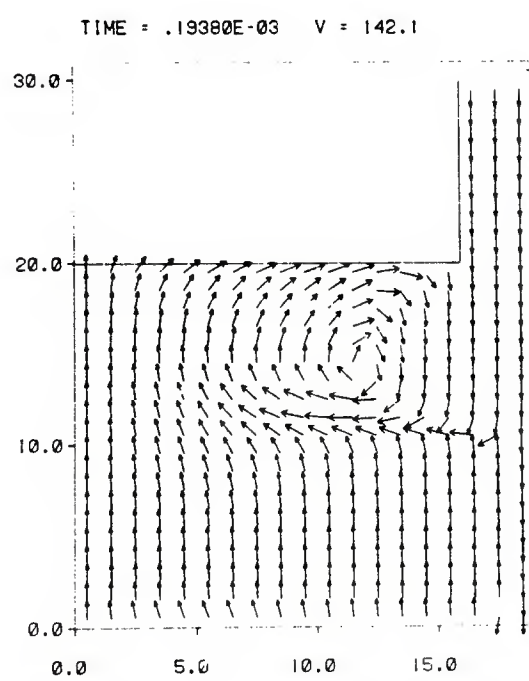


Figure B-48. See caption for Figure B-44. Flow reversal and reestablishment of recirculation by rarefaction wave; $t = 0.19 \text{ ms}$.

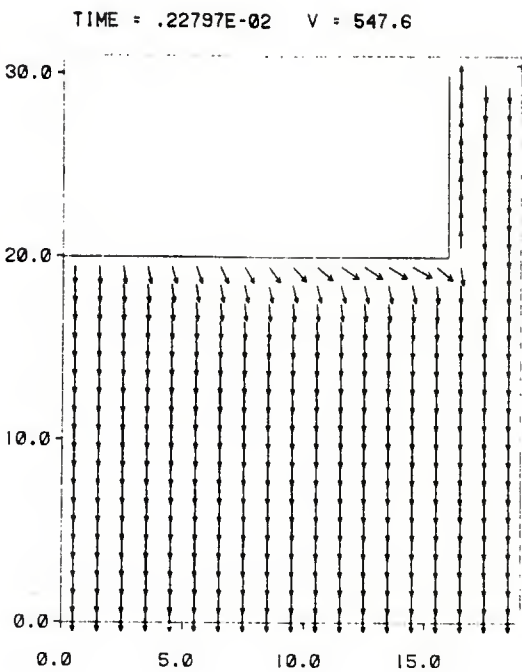


Figure B-49. See caption for Figure B-44. Final flow pattern; $t = 2.28 \text{ ms}$.

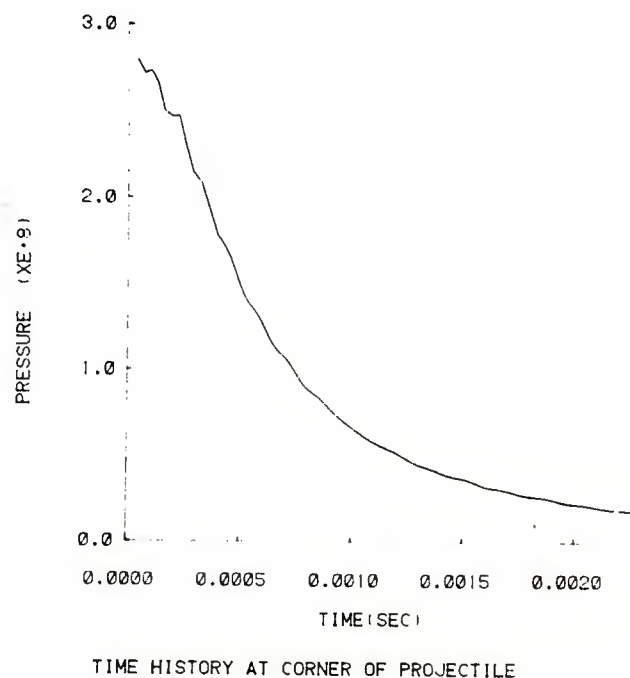
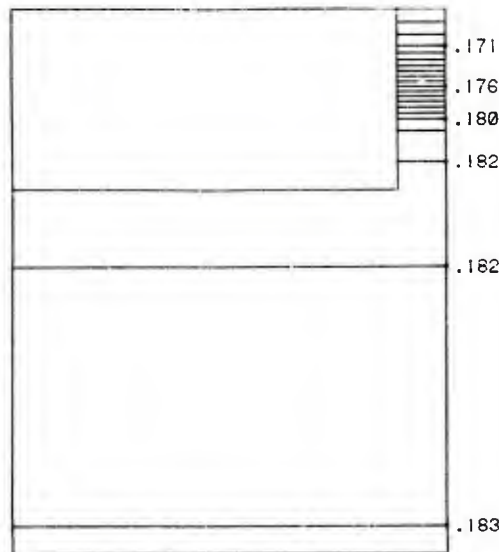


Figure B-50. Time history of pressure at cell corner for calculation at standard resolution.



PRESSURE CONTOURS AT TIME = .22797E-02

Figure B-51. See caption for Figure B-44. Pressure field contours for standard resolution run.

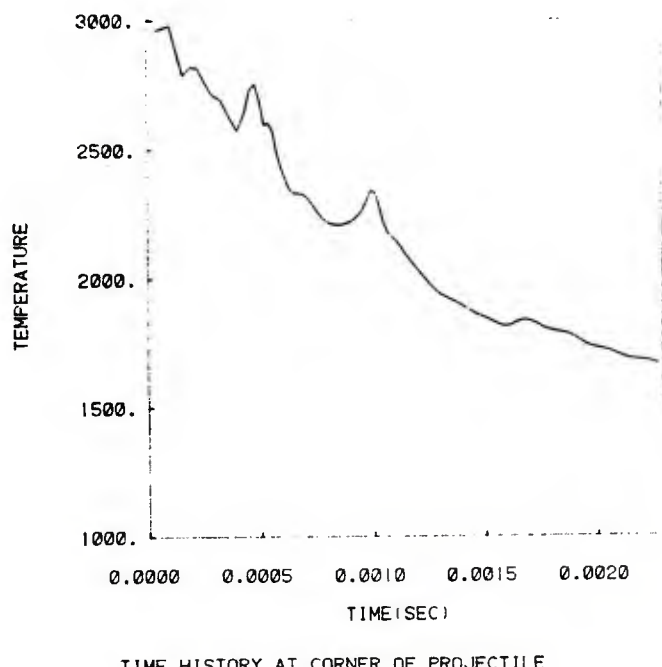
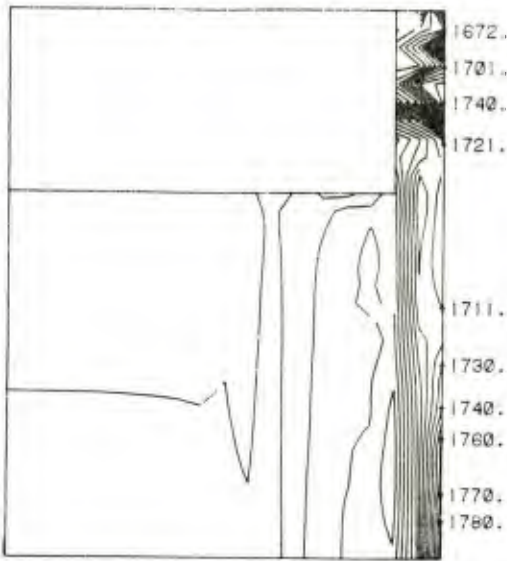


Figure B-52. Time history of temperature at corner of shell for calculation at standard resolution.



TEMPERATURE CONTOURS AT TIME = .22797E-02

Figure B-53. See caption for Figure B-44. Temperature field contours for calculation at standard resolution.

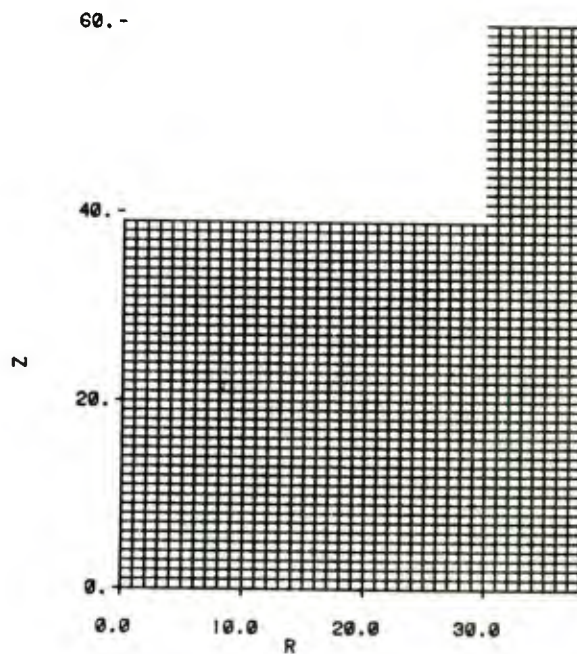


Figure B-54. Expanded computational grid for making the twice normal resolution runs (40×40). Correct aspect ratio of cells are shown in Figure 15.

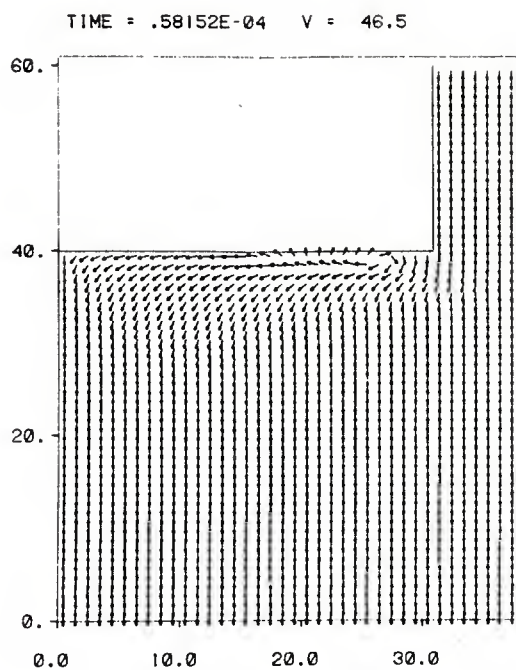


Figure B-55. Whole field visualization of flow pattern for (40 × 40) resolution calculation of 40 mm diameter barrel with 1% gap. Early time formation of rarefaction region; $t = 0.058$ ms.

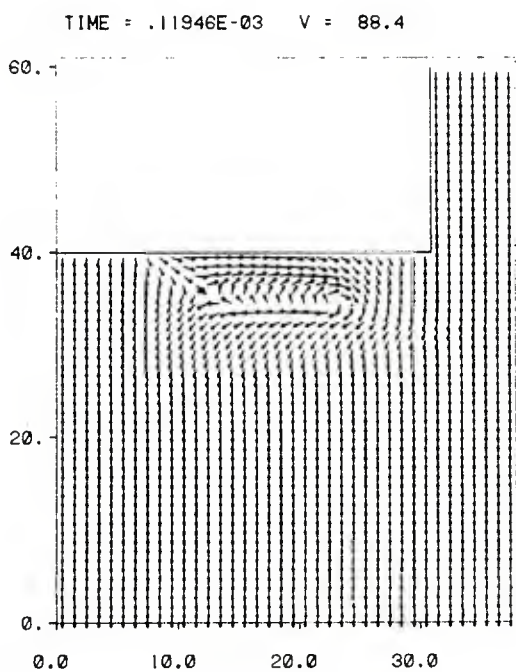


Figure B-56. See caption for Figure B-55. Growth of recirculation eddy; $t = 0.12$ ms.

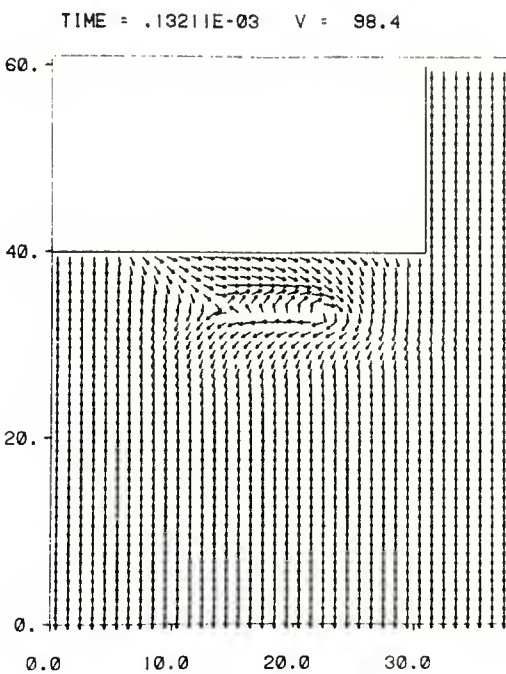


Figure B-57. See caption for Figure B-55. Growth of separation eddy;
t = 0.13 ms.

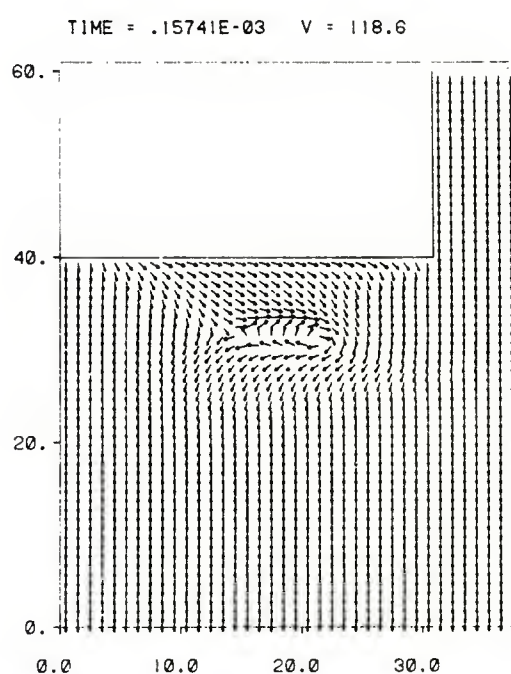


Figure B-58. See caption for Figure B-55. Diffusion of recirculation eddy;
t = 0.16 ms.

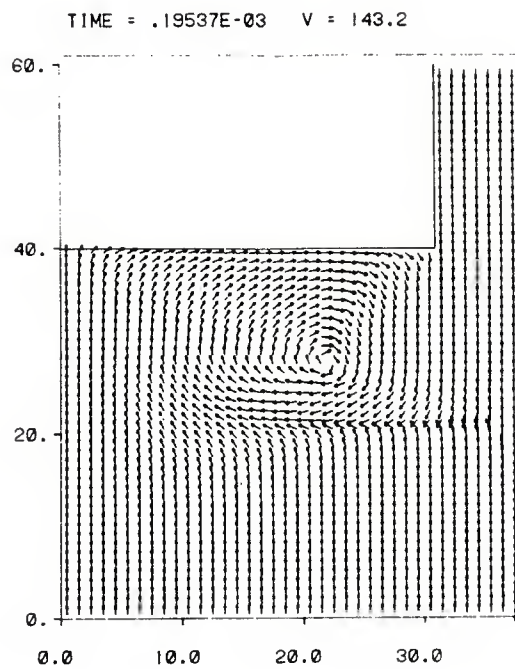


Figure B-59. See caption for Figure B-55. Reestablishment of recirculation eddy due to rarefaction wave; $t = 0.19$ ms.

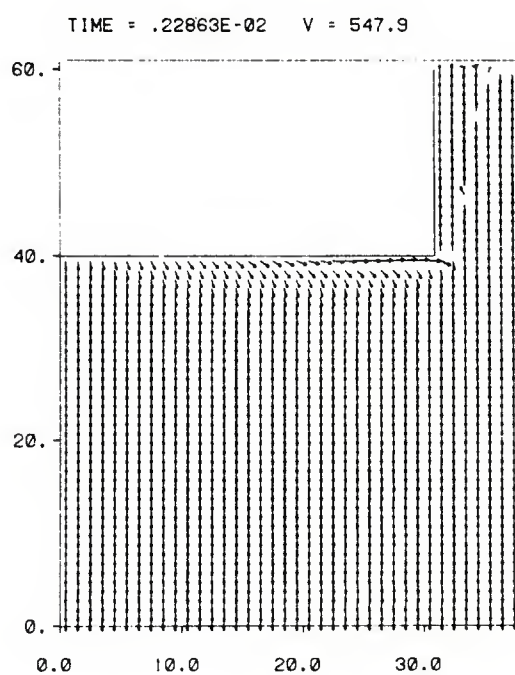
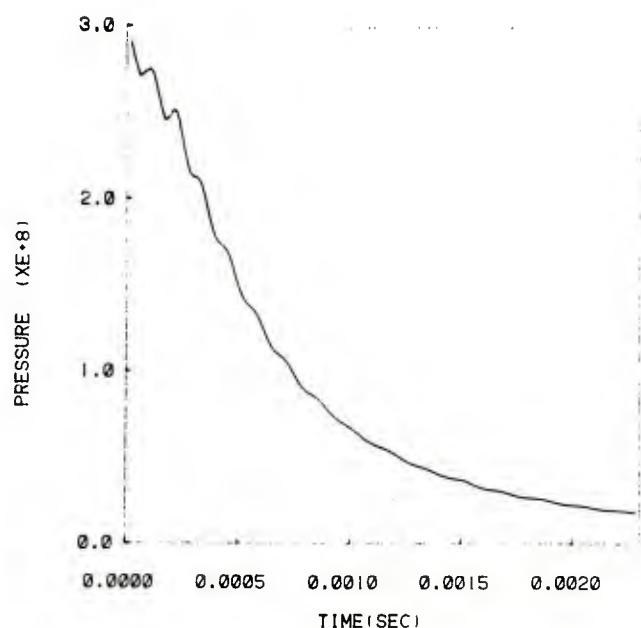
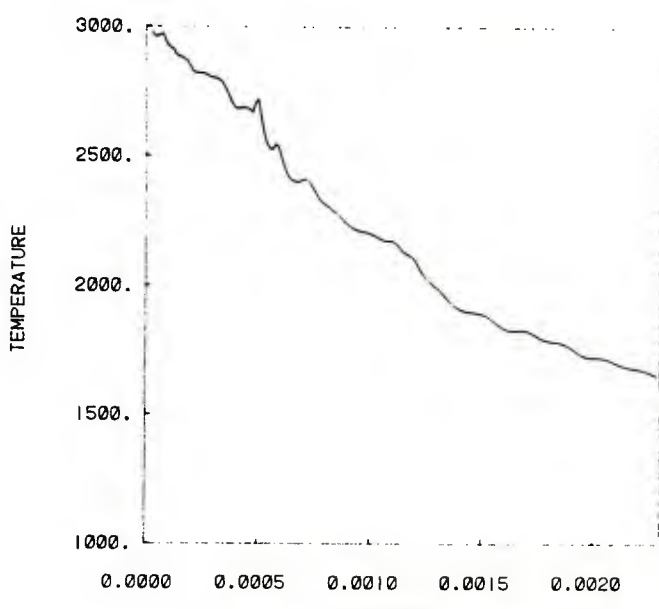


Figure B-60. See caption for Figure B-55. Final flow field; $t = 2.29$ ms.
Note that growing boundary layers on the shell and the wall lead to countercurrent flow and flow splitting at the corner.



TIME HISTORY AT CORNER OF PROJECTILE

Figure B-61. Time history of pressure at the corner of the shell showing the same behavior as in the lower resolution runs.



TIME HISTORY AT CORNER OF PROJECTILE

Figure B-62. Time history of temperature at the corner of the shell showing the same behavior as in the low resolution calculations.

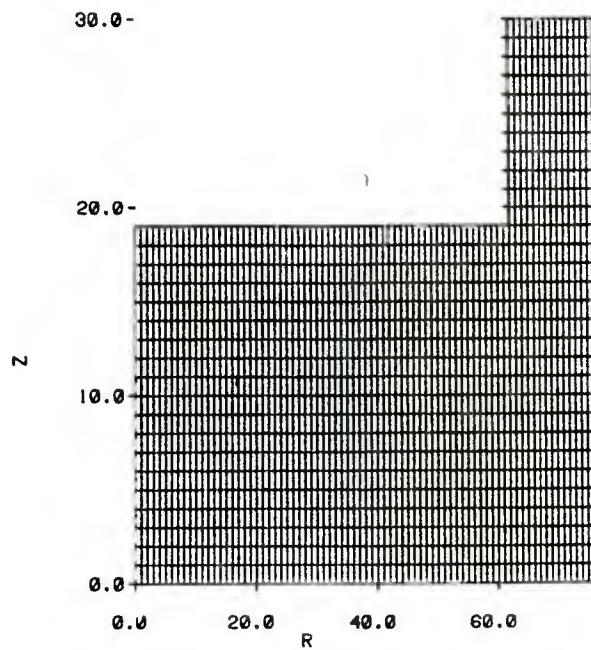


Figure B-63. Computation grid for highest radial resolution calculation (20 × 80). Grid has been distorted into rectangular configuration for the purposes of whole field visualization.

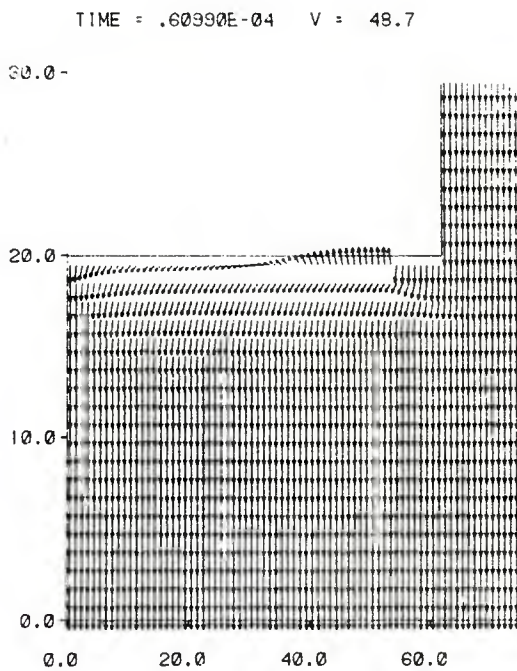


Figure B-64. Highest resolution calculation of 40 mm diameter barrel with 1% gap. Early time expansion region behind shell; t = 0.061 ms.

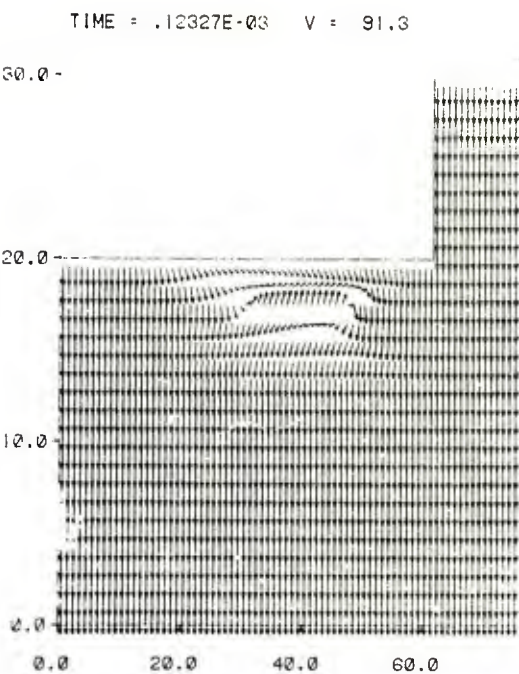


Figure B-65. See caption for Figure B-64. Dissipation of recirculation eddy; $t = 0.12 \text{ ms.}$

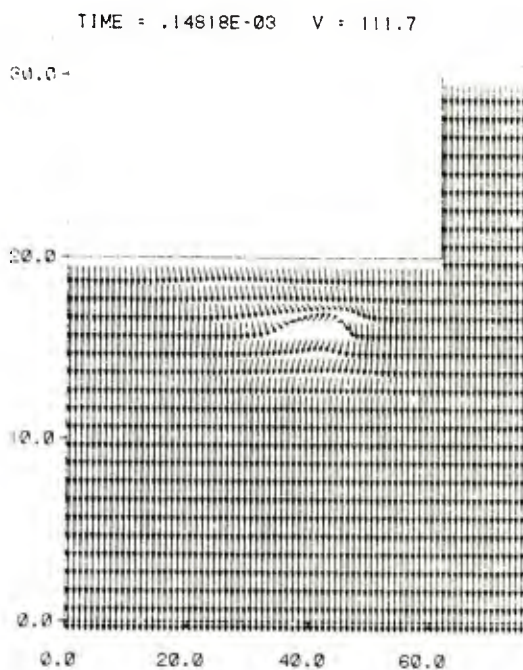


Figure B-66. See caption for Figure B-64. Dissipation and migration of recirculation eddy; $t = 0.15 \text{ ms.}$

TIME = .19801E-02 V = 144.9

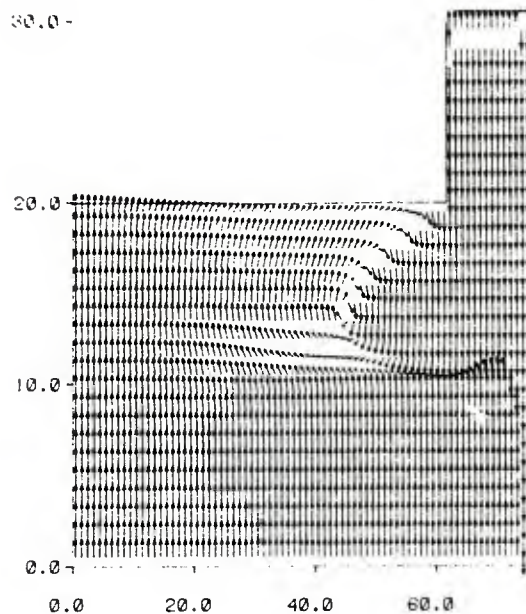


Figure B-67. See caption for Figure B-64. Reestablishment of the eddy by the rarefaction wave; $t = 0.198$ ms.

TIME = .22907E-02 V = 548.1

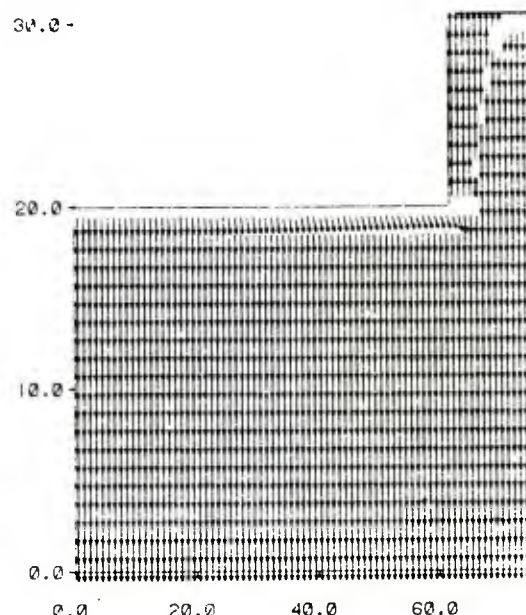


Figure B-68. See caption for Figure B-64. Late time flow field pattern; $t = 2.29$ ms. Strong countercurrent flow in gap similar to 40×40 resolution calculation.

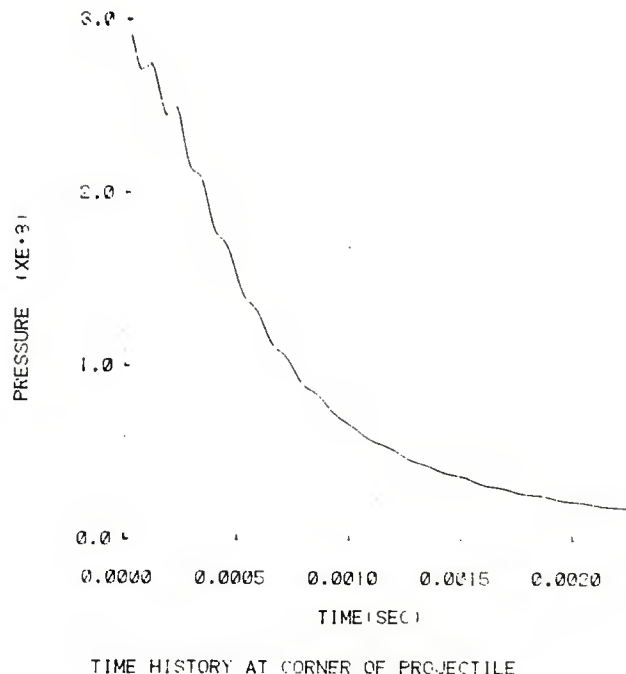


Figure B-69. Time history of pressure at the corner of the shell for 40 mm diameter barrel, 1% gap with high (20×80) resolution. Results identical to lower resolution runs.

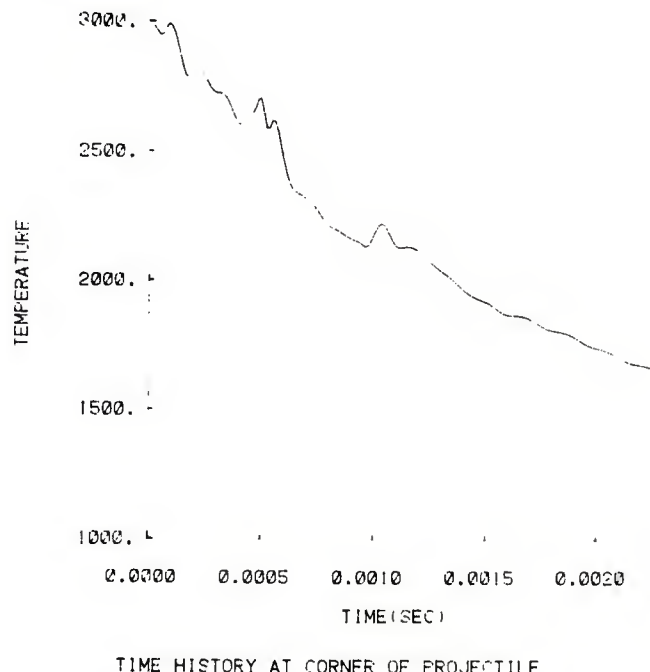
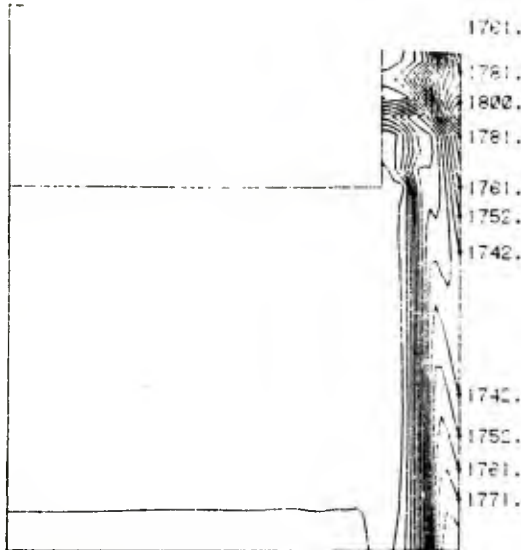


Figure B-70. Time history of gas temperature at the corner of the shell for case described in Figure B-69. Results substantially the same as in standard resolution calculation.



TEMPERATURE CONTOURS AT TIME = .22907E-02

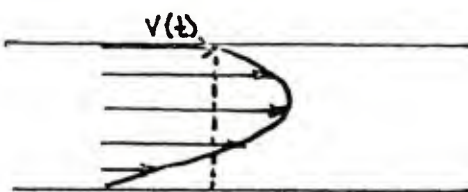
Figure B-71. See caption for Figure B-64. Temperature contours at late time.
Values agree with standard resolution case to within about 20°C except
right at the gap exit. See Figure B-53.

APPENDIX C
CONSIDERATIONS ON THE OUTFLOW BOUNDARY CONDITIONS

Excerpt from letter dated 27 February 1981
to Dr. Csaba Zoltani from Dr. Stuhmiller

It was a pleasure to meet with you and the BRL staff earlier this month to discuss both the flow calculations done under the present contract and the future directions of BRL in numerical simulations. My only regret is that the time was so short that we were just starting to get to the nuances of the physics and the numerics. I hope that over the next several months we can rectify that situation.

As you recall, we had a lengthy discussion on the flow in the annular gap. In our calculations, we assumed that the average gas velocity out of the gap was equal to the shell velocity. You expressed your concern that there should be a net positive flow rate relative to the shell. When we considered the zero velocity wall boundary condition, then we find a region where the velocity is considerably less than the shell so that the net flow is not as definite.



The curvature of the profile in laminar flow is governed by the pressure gradient and can take a maximum value up to the sonic speed. It was decided to arbitrarily assume a flow rate that was 10% higher than the shell speed.

Later that week, Henry Evans was contacted about using an integral formula for the flow rate derived from the steady state, one-dimensional form of the axial momentum equation. Taken literally this formula produces supersonic velocities (because the overall pressure drop is so large that the differential form of the equations is incorrect). More importantly, it is not proper to apply conditions which are approximate integrals of the solution - the partial differential equations must have local boundary conditions.

Reopening this issue led me to look into this compressible channel flow more closely. The problem can only be resolved with a two-dimensional calculation, with shock capture if it exists, of the channel flow and the widening ahead of the shell, but this goes beyond our present scope. Instead, I considered the allowed flow rates for laminar and turbulent channel flow if the velocity profile maximum was sonic.

The first question to be answered is whether the flow is laminar or turbulent. The nominal conditions considered are

$$\text{gap half-width, } h = 10^{-4} \text{ m}$$

$$\text{gap length, } L = 4 \times 10^{-2} \text{ m}$$

$$\text{density, } \rho = 200 \text{ kgm/m}^3$$

$$\text{shell velocity, } V < 400 \text{ m/sec}$$

$$\text{gas viscosity, } \mu = 8 \times 10^{-5} \text{ kgm/sec-m}$$

The Reynolds number based on the half width is

$$Re = \frac{\rho V h}{\mu} \approx 10^5$$

which suggests that the flow is turbulent, if turbulence has time to develop. From stability theory, disturbances grow as e^{kct} with time or $e^{kcx/V}$ with distance. For plane Poiseuille flow (according to C. C. Lin, Theory of Hydrodynamic Stability, Cambridge, p. 30) the maximum growth rate occurs at $Re \approx 6 \times 10^4$ for a wavelength $k \approx 0.75/h$ and has a magnitude $c/U \approx 7.65 \times 10^{-3}$. Therefore disturbances in the inlet of the gap will grow by an amount

$$e^{kcL/V} = e^{2.3}$$

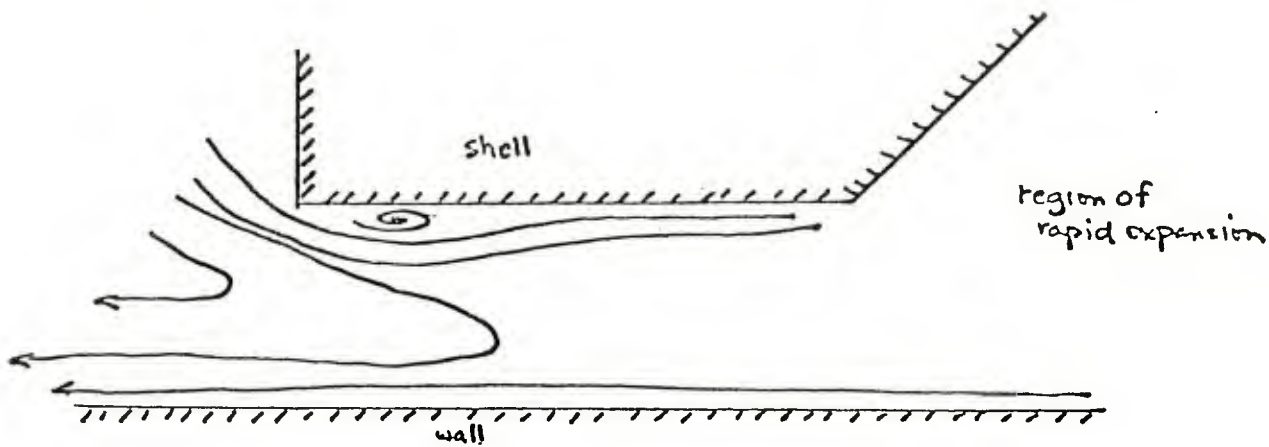
by the end of the channel. This growth is far less than that required by empirical transition theory, the so-called e^9 rule, so despite the high Reynolds number the flow is probably unsteady and laminar, not turbulent. These considerations are the same ones that cause me to doubt if true turbulence exists in the internal ballistic flows, hence if conventional turbulence models are appropriate.

The next question is whether laminar flow will have a chance to establish itself, that is, if inlet conditions will be smoothed out at the parabolic profile formed. The characteristic time behavior for the slowest viscous mode is $e^{-\mu t/\rho h^2}$, or as a spatial variation $e^{-\mu x/\rho Uh^2}$. Again, over the length of the gap the inlet profile will have relaxed by an amount equal to

$$e^{-\mu L/\rho Uh^2} = e^{-0.004}$$

Therefore, by viscous effects alone the inlet condition will be hardly changed along the gap.

The final, simple possibility is that the wall boundary layer that developed in the chamber before the gap triggers plane Couette flow, that is, a linear variation from the shell velocity to zero at the wall. This solution is discussed in Liepmann and Roshko, Elements of Gas Dynamics, Wiley, pp. 311-328. Flow separation at the corner is probably too great a phenomena to ignore. A schematic diagram of the corner and gap flow in the accelerating coordinate system is as follows



What about the question of flow rate? We've determined that the flow is probably neither fully developed laminar, turbulent, or Blasius, but what would we get if it were? From Schlichting, Boundary Layer Theory, McGraw-Hill, p. 505, we find the average flow velocity (in a pipe) is related to the maximum velocity (which we assume is the sonic speed, a) by the formula

$$u_{av}/u_{max} = \frac{2n^2}{(n+1)(2n+1)}$$

so that the following table can be generated

| <u>Re</u> | <u>n</u> | <u>u_{av}/u_{max}</u> |
|-----------------|----------|------------------------------------|
| 4×10^3 | 6.0 | 0.791 |
| 2×10^4 | 6.6 | 0.807 |
| 1×10^5 | 7.0 | 0.817 |

For fully developed laminar flow the profile is

$$u(y) = A + By + Cy^2$$

subject to the boundary conditions that

$$u(-h) = 0$$

$$u(+h) = V$$

$$u_{\max} = a$$

which after some simple, but lengthy algebra leads to

$$\frac{u_{\text{av}}}{u_{\max}} = \frac{1}{3} + \frac{1}{3} M \pm \frac{1}{3} \sqrt{1 - M}$$

where M is the shell Mach number, V/a . An abbreviated table of values generated by this formula is

| <u>M</u> | <u>u_{av}/u_{\max}</u> |
|----------|--|
| 0.0 | 0.667 |
| 0.2 | 0.698 |
| 0.4 | 0.725 |
| 0.6 | 0.744 |
| 0.8 | 0.749 |
| 1.0 | 0.667 |

Finally, plane Couette flow would have a profile

$$u(y) = \frac{1}{2} V (1 + y/h)$$

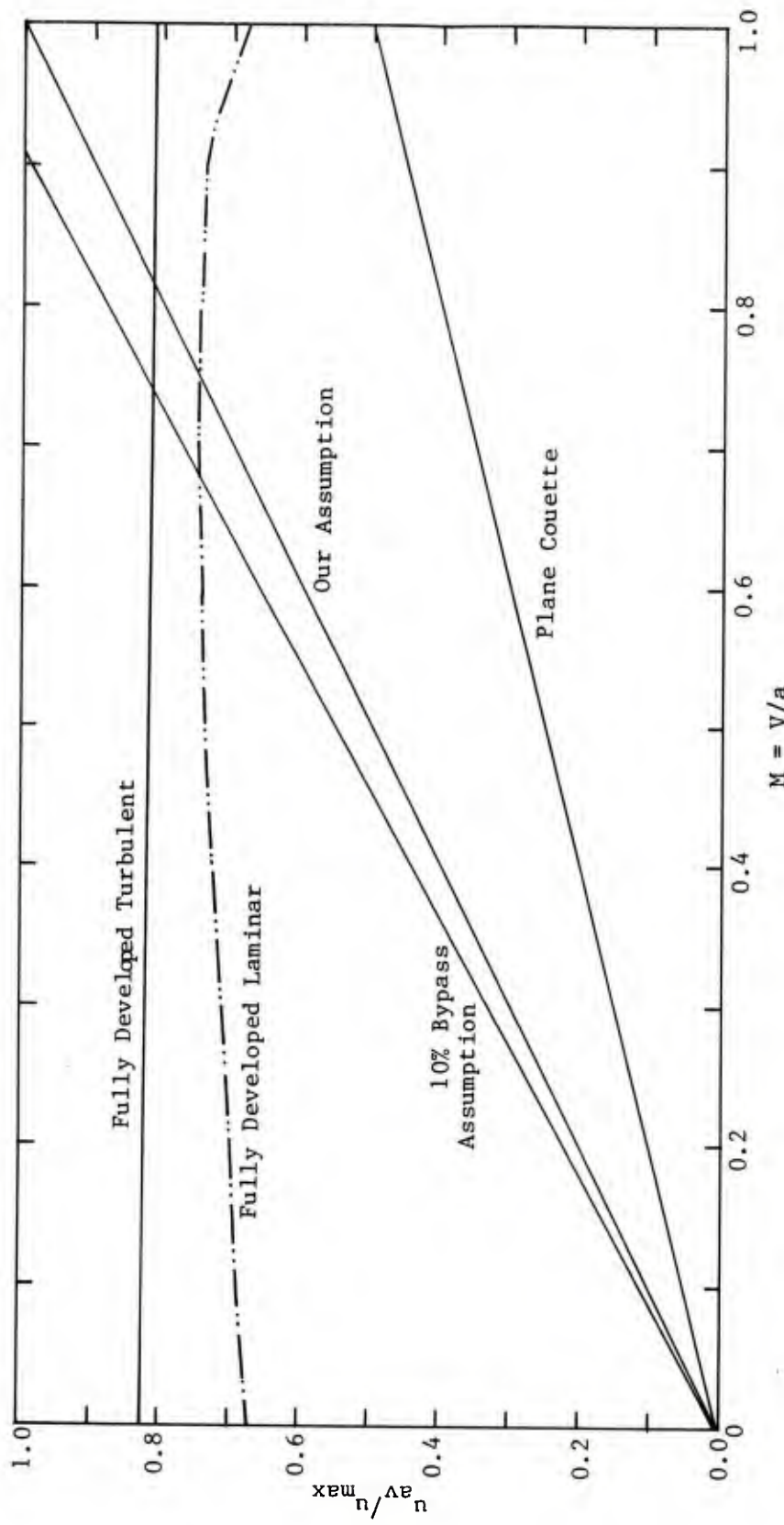
with the corresponding flow rate relation

$$\frac{u_{\text{av}}}{u_{\max}} = \frac{1}{2} M$$

In our calculations already presented we used the condition

$$\frac{u_{\text{av}}}{u_{\max}} = M$$

The various flow rates are displayed on the enclosed plot. The correct flow rate lies somewhere between the Couette flow that would exist in the absence of a pressure gradient and the fully developed flow which we know do not have time to form. The assumption used in the present calculation is in that broad band.



DISTRIBUTION LIST

| <u>No. of Copies</u> | <u>Organization</u> | <u>No. of Copies</u> | <u>Organization</u> |
|----------------------|---|----------------------|--|
| 12 | Commander Defense Technical Info Center ATTN: DDC-DDA Cameron Station Alexandria, VA 22314 | 2 | Commander US Army Armament Research and Development Command ATTN: DRDAR-LCU-E, S. Westley, D. Katz Dover, NJ 07801 |
| 2 | HQDA(DAMA-CSM-CS, LTC Townsend, COL Zimmerman) Washington, DC 20310 | 3 | Commander US Army Armament Research and Development Command ATTN: DRDAR-LCU-EP, S. Einstein, S. Bernstein DRDAR-LCU-S, R. Corn Dover, NJ 07801 |
| 1 | Commander US Army Materiel Development and Readiness Command ATTN: DRCDMD-ST 5001 Eisenhower Avenue Alexandria, VA 22333 | 2 | Commander US Army Armament Research and Development Command ATTN: DRDAR-TDS, V. Lindner DRDAR-TD, E. Friedman Dover, NJ 07801 |
| 3 | Commander US Army Armament Research and Development Command ATTN: DRDAR-CG, MG Light Dover, NJ 07801 | 2 | Commander US Army Armament Research and Development Command Benet Weapons Laboratory, LCWSL ATTN: A. Hussain DRDAR-LCB-TL Watervliet Arsenal, NY 12189 |
| 3 | Commander US Army Armament Research and Development Command ATTN: DRDAR-TSS (2 cys) DRDAR-LC, COL Kenyon Dover, NJ 07801 | 1 | Commander US Army Armament Materiel Readiness Command ATTN: DRSAR-LEP-L, Tech Lib Rock Island, IL 61299 |
| 3 | Commander US Army Armament Research and Development Command ATTN: DRDAR-LCA, H. Fair, D. Down, G. Bubb Dover, NJ 07801 | 1 | Commander US Army Aviation Research and Development Command ATTN: DRDAV-E 4300 Goodfellow Blvd. St. Louis, MO 63120 |
| 4 | Commander US Army Armament Research and Development Command ATTN: DRDAR-LCU, A. Moss, D. Costa, R. Reisman, E. Wurzel Dover, NJ 07801 | | |

DISTRIBUTION LIST

| <u>No. of Copies</u> | <u>Organization</u> | <u>No. of Copies</u> | <u>Organization</u> |
|----------------------|---|----------------------|---|
| 1 | Director US Army Air Mobility Research and Development Laboratory Ames Research Center Moffett Field, CA 94035 | 3 | Project Manager M110E2 Weapons System ATTN: DRCPM-M110E2-TM, S. Smith, R. Newlon, B. Walters Rock Island, IL 61299 |
| 1 | Commander US Army Communications Research and Development Command ATTN: DRDCO-PPA-SA Fort Monmouth, NJ 07703 | 2 | Commander US Army Research Office ATTN: J. Chandra E. Singleton P.O. Box 12211 Research Triangle Park, NC 27709 |
| 1 | Commander US Army Electronics Research and Development Command Technical Support Activity ATTN: DELSD-L Fort Monmouth, NJ 07801 | 1 | Director US Army TRADOC Systems Analysis Activity ATTN: ATAA-SL, Tech Lib White Sands Missile Range, NM 88002 |
| 1 | Commander US Army Missile Research and Development Command ATTN: DRSMI-R Redstone Arsenal, AL 35809 | 1 | Commander US Army Field Artillery School ATTN: APSF-CD-W, LT Monigal Fort Sill, OK 73503 |
| 1 | Commander US Army Missile Research and Development Command ATTN: DRSMI-YDL Redstone Arsenal, AL 35809 | 2 | Commander Naval Surface Weapons Center ATTN: J. East Tech Lib Dahlgren, VA 22338 |
| 1 | Commander US Army Tank Automotive Research and Development Command ATTN: DRDTA-UL Warren, MI 48090 | 1 | Commander Naval Weapons Center ATTN: Tech Lib China Lake, CA 93555 |
| 6 | Project Manager Cannon Artillery Weapons System ATTN: DRCPM-CAWS, COL Phillip DRCPM-CAWS-AM, F. Menke H. Hassman DRCPM-CAWS-GP, B. Garcia DRCPM-CAWS-WP, H. Noble DRCPM-SA, J. Brooks Dover, NJ 07801 | 3 | Commander Naval Ordnance Station ATTN: F.W. Robbins S.E. Mitchell Tech Lib Indian Head, MD 20640 |

DISTRIBUTION LIST

| <u>No. of Copies</u> | <u>Organization</u> | <u>No. of Copies</u> | <u>Organization</u> |
|----------------------|--|----------------------|---|
| 2 | Lawrence Livermore Laboratory University of California ATTN: S.C. Buckingham S-W Kang Livermore, CA 94450 | 1 | University of Delaware Department of Mathematical Science ATTN: M.Z. Nashed Newark, DE 19711 |
| 1 | Director Los Alamos Scientific Laboratory ATTN: D. Durak Los Alamos, NM 87545 | 1 | University of Illinois Dept. of Mechanical Engineering ATTN: H. Krier 144 MEB, 1206 W. Green Street Urbana, IL 61801 |
| 1 | Director Los Alamos Scientific Laboratory ATTN: Group T-7, B. Wendroff Mail Stop 233 Los Alamos, NM 87545 | 1 | University of Illinois-Urbana Mechanics and Industrial Engineering ATTN: S.L. Soo Urbana, IL 61801 |
| 1 | Calspan Corporation ATTN: E.B. Fisher P.O. Box 400 Buffalo, NY 14221 | 1 | University of Maryland Institute of Physical Science and Technology ATTN: S.I. Pai College Park, MD 20742 |
| 1 | Paul Gough Associates, Inc. ATTN: P.S. Gough P.O. Box 1614 Portsmouth, NH 03801 | 1 | Massachusetts Institute of Technology Department of Materials Science and Engineering ATTN: J. Szekely 77 Massachusetts Avenue Cambridge, MA 02139 |
| 1 | Science Applications, Inc. ATTN: E.B. Edelman 23146 Cumorah Crest Woodland Hills, CA 91364 | 1 | Princeton Combustion Rsch Labs, Inc. ATTN: M. Summerfield 1041 U.S. Highway One North Princeton, NJ 08540 |
| 3 | Scientific Research Associates, Inc. ATTN: H. McDonald R.C. Buggeln H.F. Gibeling P.O. Box 498 Glastonbury, CT 06033 | 1 | Pennsylvania State University Department of Mechanical Engineering ATTN: K.K. Kuo University Park, PA 16801 |
| 1 | University of Cincinnati ATTN: A. Hamed Cincinnati, OH 45221 | 1 | Princeton University Guggenheim Laboratories Department of Aerospace and Mechanics Science ATTN: L.H. Caveny P.O. Box 710 Princeton, NJ 08540 |
| 1 | University of Cincinnati Dept. of Aerospace Engineering ATTN: W. Tabakoff Cincinnati, OH 45221 | | |

DISTRIBUTION LIST

| <u>No. of Copies</u> | <u>Organization</u> |
|--------------------------|--|
| 1 | Rensselaer Polytechnic Institute Mathematical Sciences Department ATTN: D. Drew Troy, NY 12181 |
| 1 | University of Wisconsin-Madison Mathematics Research Center ATTN: J.R. Bowen 610 Walnut Street Madison, Wi 53706 |
| 1 | Worcester Polytechnic Institute Department of Mathematics ATTN: P.W. Davis Worcester, MA 01609 |

Aberdeen Proving Ground
Dir, USAMSAA
ATTN: DRXSY-D
DRXSY-MP, H. Cohen
Cdr, USATECOM
ATTN: DRSTE-TO-F
Dir, USAMTD
ATTN: STEAP-MT-A, W. Rieden,
C. Herud, H. Bechtol
Dir, USACSL, Bldg. E3516, APG-EA
ATTN: DRDAR-CLB-PA

USER EVALUATION OF REPORT

Please take a few minutes to answer the questions below; tear out this sheet, fold as indicated, staple or tape closed, and place in the mail. Your comments will provide us with information for improving future reports.

1. BRL Report Number _____

2. Does this report satisfy a need? (Comment on purpose, related project, or other area of interest for which report will be used.)

3. How, specifically, is the report being used? (Information source, design data or procedure, management procedure, source of ideas, etc.)

4. Has the information in this report led to any quantitative savings as far as man-hours/contract dollars saved, operating costs avoided, efficiencies achieved, etc.? If so, please elaborate.

5. General Comments (Indicate what you think should be changed to make this report and future reports of this type more responsive to your needs, more usable, improve readability, etc.)

6. If you would like to be contacted by the personnel who prepared this report to raise specific questions or discuss the topic, please fill in the following information.

Name: _____

Telephone Number: _____

Organization Address: _____

